

WIRELESS REFLECTANCE PULSE OXIMETER DESIGN AND
PHOTOPLETHYSMOGRAPHIC SIGNAL PROCESSING

by

KEJIA LI

B.S., Zhejiang University, 2008

A THESIS

submitted in partial fulfillment of the requirements for the degree

MASTER OF SCIENCE

Department of Electrical & Computer Engineering
College of Engineering

KANSAS STATE UNIVERSITY
Manhattan, Kansas

2010

Approved by:

Major Professor
Steve Warren

Copyright

KEJIA LI

2010

Abstract

Pulse oximetry, a noninvasive circulatory system monitoring technique, has been widely adopted in clinical and homecare applications for the determination of heart rate and blood oxygen saturation, where measurement locations are typically limited to fingertips and earlobes. Prior research indicates a variety of additional clinical parameters that can be derived from a photoplethysmogram (PPG), the fundamental time-domain signal yielded by a pulse oximeter sensor. The gap between this research potential and practical device applications can be decreased by improvements in device design (e.g., sensor performance and geometry, sampling fidelity and reliability, etc.) and PPG signal processing.

This thesis documents research focused on a novel pulse oximeter design and the accompanying PPG signal processing and interpretation. The filter-free reflectance design adopted in the module supplements new methods for signal sampling, control, and processing, with a goal to acquire high-fidelity raw data that can provide additional physiologic data for state-of-health analyses. Effective approaches are also employed to improve signal stability and quality, including shift-resistant baseline control, an anti-aliasing sampling frequency, light emitting diode intensity autoregulation, signal saturation inhibition, etc. MATLAB interfaces provide data visualization and processing for multiple applications. A feature detection algorithm (decision-making rule set) is presented as the latest application, which brings the element of intelligence into the pulse oximeter design by enabling onboard signal quality verification.

Two versions of the reflectance sensor were designed, built, calibrated, and utilized in data acquisition work. Raw data, which are composed of four channels of signals at a 240 Hz sampling rate and a 12-bit precision, successfully stream to a personal computer via a serial connection or wireless link. Due to the optimized large-area sensor and the intensity autoregulation mechanism, PPG signal acquisition from measurement sites other than fingertips and earlobes, e.g., the wrist, become viable and retain signal quality, e.g., signal-to-noise ratio. With appropriate thresholds, the feature detection algorithm can successfully indicate motion occurrence, signal saturation, and signal quality level. Overall, the experimental results from a variety of subjects and body locations in multiple applications demonstrate high quality PPGs, prototype reliability, and prospects for further research value.

Table of Contents

List of Figures.....	vi
List of Tables.....	ix
Acknowledgements.....	x
CHAPTER 1 - Introduction.....	1
Potential Clinical Parameters Available from PPG Data.....	1
Designing a Novel and Competent Pulse Oximeter	6
CHAPTER 2 - System and Methods	8
System Layout at the Circuitry Level	8
Shift Resistance	9
Control System	12
Removable Noise.....	14
Motion Artifact	15
Calibration Approach.....	18
Power Consumption.....	18
CHAPTER 3 - Hardware Development.....	20
Microprocessor and Wireless Link	20
Version 1 Circuitry Design.....	23
Version 2 Circuitry Design.....	27
Device Prototypes	28
CHAPTER 4 - Firmware Development	30
Jenie Application Programming Interface.....	30
Firmware Control Flow	32
Firmware Optimization	33
CHAPTER 5 - MATLAB Interface.....	35
Serial Communication.....	35
MATLAB Code	37
MATLAB Graphical User Interface 1	39
MATLAB Graphical User Interface 2	40

CHAPTER 6 - Multiple Applications	42
Blood Oxygen Saturation Calibration.....	42
Multi-Location Measurements and Discussion	44
Biomedical Instrumentation Laboratory	52
Other Applications	55
CHAPTER 7 - Feature Detection	57
Algorithm Flow	57
Feature Selection.....	60
Initial Results and Discussion	65
CHAPTER 8 - Conclusion	69
Future Work.....	70
References	71
Appendix A - Hardware Schematics	76
Pulse Oximeter Version 1	76
Pulse Oximeter Version 2	77
Appendix B - Hardware PCB.....	78
Pulse Oximeter Version 1	78
Pulse Oximeter Version 2	79
Appendix C - Hardware Parts Lists	80
Pulse Oximeter Version 1	80
Pulse Oximeter Version 2	82
Appendix D - JN5139 Module Pin Descriptions.....	83
Pin Configurations	83
Pin Assignments	84

List of Figures

Figure 1. Volume-pressure relationship in an arterial segment.....	2
Figure 2. Parameters obtained from digital volume pulse analysis [14].....	3
Figure 3. Respiration-induced venous volume pulse and arterial volume pulse. Their combined volume signal is demonstrated as V+A.	5
Figure 4. System layout at the circuitry level.....	8
Figure 5. The first-stage signal with a large DC portion enters the differential amplifier with gain G to obtain the second-stage photoplethysmographic signal.	10
Figure 6. Palm measurement site data with compensation demonstration.	12
Figure 7. Control flow for the pulse oximeter with feedback functionality (black blocks).....	13
Figure 8. An example of removable noise. (a) Photoplethysmographic waveform (compensated) corrupted by ambient noise. (b) Frequency spectrum of the 14 seconds of data sampled at 240 Hz.	15
Figure 9. (a) Photoplethysmographic waveform severely corrupted by three axes of hand motion artifact. (b) Frequency spectrum of 28 seconds of data sampled at 100 Hz.....	16
Figure 10. Three photoplethysmographic signals (uncompensated) under an analogous slight motion condition but with different parameter pairs (W , R), where W refers to the window size of the moving average filter, R refers to the rate of assigning V_{ref} to the DAC, and $f_s = 240$ Hz.	17
Figure 11. Block diagram of the JN5139 chip [39].	21
Figure 12. Block diagram of the JN5139 module [40].	22
Figure 13. Microprocessor module schematic.....	23
Figure 14. Red & near-infrared excitation LED module schematic.	25
Figure 15. Signal sampling module schematic.....	25
Figure 16. Power supply and management module schematic.....	26
Figure 17. Flash memory and display LED module schematic.....	27
Figure 18. Improved red & near-infrared excitation LED module (version 2) schematic.....	27
Figure 19. Top view of prototype version 1 and version 2.	28
Figure 20. Bottom view of prototype version 1.	29

Figure 21. Bottom view of prototype version 2.	29
Figure 22. Jenie application code structure [44].....	31
Figure 23. Ten-step firmware flow design for one data cycle of overall length T . CH1 and CH2 refer to the red and near-infrared channels, respectively. Note that the height of each block is not its actual implementation time.....	32
Figure 24. Serial communication data frame structure. R: red channel; IR: near-infrared channel. Numbers are in bytes, with 18 bytes total. The first 8 bytes are assigned to the unique MAC address, the next 8 bytes are assigned to the four channels of signal data, and the last two bytes are appended to ensure the frame integrity.....	36
Figure 25. Pulse Oximeter MATLAB GUI 1 that contains a signal processing module.....	40
Figure 26. MATLAB GUI 2 developed for a feature detection tool.	41
Figure 27. MATLAB GUI 1 adopted for blood oxygen saturation calculations. In this example, a series of calibration ratios is extracted from the current data segment.	43
Figure 28. Blood oxygen levels read from a BCI [®] 3180 pulse oximeter plotted against the R values calculated by the pulse oximeter prototype. The linear regression line (solid line) from the least-squares fit is expressed as $SpO_2 (\%) = 109.2 - 23.7R$ in comparison with the published calibration line (dashed line) $SpO_2 (\%) = 110 - 25R$	44
Figure 29. Fingertip measurement site results: 25 seconds of time-domain PPG data from the (a) red and (b) near-infrared channels.	46
Figure 30. Fingertip measurement site results: frequency-domain spectra of 100 seconds of PPG data from the red (a) and near-infrared (b) channels.....	47
Figure 31. Fingertip signal processing and digital volume pulse (DVP) analysis.	48
Figure 32. Magnitude and phase response of the 200-order low-pass FIR filter.	49
Figure 33. Wrist measurement site results. The pulsatile curves correspond to different placement locations.	50
Figure 34. Pulse oximeter measurement locations on the left wrist.	50
Figure 35. Earlobe measurement site results: (a) near-infrared channel and (b) red channel.....	51
Figure 36. Temple measurement data: (a) time-domain PPG with respiration and motion information and (b) frequency-domain spectrum.	52
Figure 37. Ten pulse oximeters to be used in a Fall 2009 biomedical instrumentation laboratory.	53

Figure 38. A team of students acquiring PPG data from the fingertip and performing ambient noise analysis with the new pulse oximeter and MATLAB interface.....	54
Figure 39. Blood oxygen saturation determination using the BCI [®] 3180 pulse oximeter (left) and photoplethysmogram measurement on the temple to assess respiration rate (right).	54
Figure 40. Tentative estimation of venous blood oxygen saturation level: (a) time-domain signal and (b) frequency spectrum.	55
Figure 41. Digital volume pulse analysis using a curve fitting method.....	56
Figure 42. Feature detection algorithm flow.	58
Figure 43. Triangular structures identified for the minimum representations.	58
Figure 44. Feature 1: baseline variation.....	61
Figure 45. Feature 2: upstairs count.....	62
Figure 46. Feature 3: downstairs count.....	63
Figure 47. Feature 4: level count.....	63
Figure 48. Ratio of downstairs count to upstairs count.....	64
Figure 49. An example of a downsampled waveform (b) obtained from an original photoplethysmographic signal (a).....	65
Figure 50. An example of 9 minimum representations from the first 27 seconds of data in the downsampled photoplethysmogram.....	66
Figure 51. Valid pulse presented in feature detection.....	67
Figure 52. Weak pulse presented in feature detection.	67
Figure 53. No pulse identified in feature detection.	68
Figure 54. Severe motion and signal saturation identified in feature detection.	68
Figure 55. Pulse oximeter version 1 schematic.	76
Figure 56. Pulse oximeter version 2 schematic.	77
Figure 57. Pulse oximeter version 1 PCB (top view).	78
Figure 58. Pulse oximeter version 1 PCB (bottom view).	78
Figure 59. Pulse oximeter version 2 PCB (top view).	79
Figure 60. Pulse oximeter version 2 PCB (bottom view).	79
Figure 61. JN5139 module pin configurations (top view) [40].....	83

List of Tables

Table 1. Potential clinical parameters that can be obtained from a PPG.....	2
Table 2. Characteristics of a high-fidelity reflectance pulse oximeter.	7
Table 3. Features of the JN5139 transceiver and microprocessor.....	21
Table 4. Minimum connection required for the microprocessor module (from [42]).	24
Table 5. Jenie API functionality (from [43]).....	30
Table 6. Properties of an object created by the MATLAB serial() function.....	37
Table 7. MATLAB interface 1 control panel functionality.	39
Table 8. Pulse oximeter version 1 parts list.	80
Table 9. Pulse oximeter version 2 parts list.	82
Table 10. JN5139 module pin assignments (from [40]).	84

Acknowledgements

The author wishes to thank Dr. Steve Warren and Dr. Bala Natarajan for their helpful advice and assistance throughout the program, the National Science Foundation for financially supporting the project, David Thompson and Jianchu Yao for their excellent work on predecessor module designs which served as good reference for the new design, and David Huddleston for his sophisticated reflow soldering technique on surface-mounted devices.

CHAPTER 1 - Introduction

A pulse oximeter is an optical medical device allowing the noninvasive monitoring of cardiopulmonary parameters. In clinical and homecare applications, this easy to use device, usually in the form of a fingertip clip, has been widely used to acquire and display heart rate (HR) and arterial blood oxygen saturation (SpO_2).

When the pulsatile waveform, a.k.a. photoplethysmogram (PPG), yielded by one excitation wavelength in the pulse oximeter sensor is further interpreted, many other physiological parameters can be derived. The PPG records changes in blood volume over a certain length of vascular tissue, and this volumetric signal is driven by the blood pressure waveform and also constrained by the compliance of the vascular walls. Hence, intuitively there exists a strong correlation between the photoplethysmographic waveform and the blood pressure waveform – a correlation that has been addressed in the literature [1-3].

A PPG can be considered a series of continuous snapshots of the circulatory system with respect to blood volume, and the character of these snapshots is determined by the measurement site of the pulse oximeter. Hemodynamics (the study of the circulation, including cardiac hemodynamics and arterial hemodynamics) guides the physiological and mathematical relationship between blood flow, blood velocity, blood pressure, blood volume, and other cardiac and arterial characteristics [4-6].

Potential Clinical Parameters Available from PPG Data

Although the regular physiological parameters, HR and SpO_2 , are reported on a conventional pulse oximeter, the PPGs provided by the pulse oximeter sensor offer other potential clinical parameters as listed in Table 1.

The blood pressure (BP) waveform and the sampled photoplethysmogram at the same location are related by a generalized transfer function, which is not influenced by the effects of hypertension or nitroglycerin [1, 2]. In hemodynamics, compliance quantifies the volume-pressure relationship that characterizes the local vasculature. Compliance, C , as defined in Equation 1.1 is the slope of the volume-pressure curve:

$$C = \Delta V / \Delta P \quad (1.1)$$

Table 1. Potential clinical parameters that can be obtained from a PPG.

Blood pressure (BP) waveform	Pulse wave reflection parameters
<ul style="list-style-type: none"> ○ Systolic BP ○ Diastolic BP ○ Mean BP ○ Stroke volume (SV) ○ Cardiac output (CO) 	<ul style="list-style-type: none"> ○ Peak-to-peak time (PPT) ○ Pulse wave velocity (PWV) ○ Arterial elasticity (E) ○ Stiffness index (SI) ○ Reflection index (RI)
Venous volume pulsations	Perfusion index (PI)
<ul style="list-style-type: none"> ○ Respiratory rate ○ Venous blood oxygen saturation ○ Metabolic rate 	Ambient light information Patient motion Patient identity

Figure 1 illustrates an example volume-pressure curve for an arterial segment. As BP increases, the vessel is more reluctant to dilate and demonstrates decreasing compliance and increasing elasticity. Because of the hysteresis effect, a loop relationship could be taken into consideration rather than static curves [7, 8]. I.e., when the pressure decreases from “B” status to “A” status, the relationship curve would be the new dashed orange route rather than the blue solid route that describes the original “A” to “B” transition.

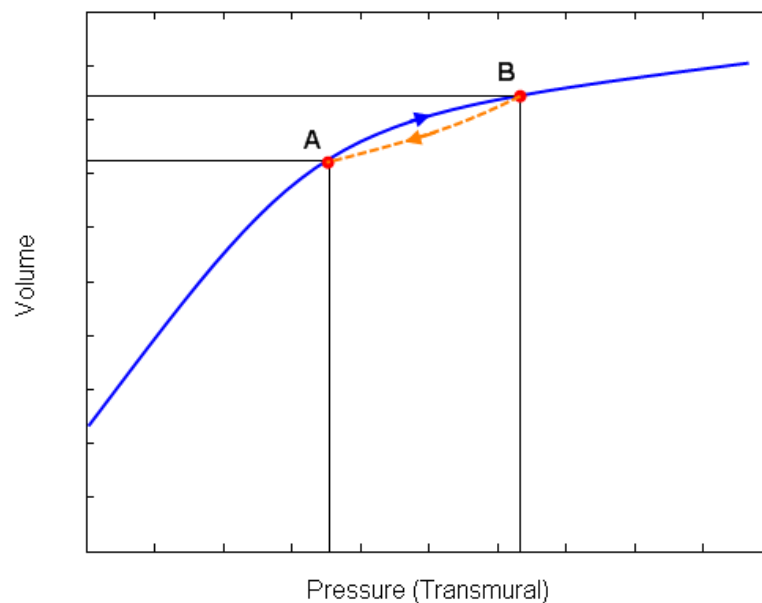


Figure 1. Volume-pressure relationship in an arterial segment.

Once a BP waveform is obtained from a volumetric waveform, systolic, diastolic, and mean BP are subsequently available. Stroke volume (SV) and cardiac output (CO) can also be estimated using a K value computed with BP information [9].

BP information can also be derived from pulse transit time (PTT) or pulse wave velocity (PWV) [10, 11], which is well correlated with peak-to-peak time (PPT) and the stiffness index (SI) [12, 13]. The PPT and SI are two parameters induced by pulse wave reflections primarily in the distal abdominal aorta [4], and these parameters are usually extracted through digital volume pulse (DVP) analysis. Figure 2 demonstrates a single DVP cycle, where the systolic component with height “b” results from the direct transmission of the systolic pressure wave from the aorta to the fingertip. The diastolic component with height “a” results from pulse wave reflections (e.g., from the lower extremities). The relative height of the diastolic component depends on the tone of the small peripheral arteries; greater elasticity will induce a larger secondary hump. The reflection index (RI) is the relative measure of the height of the diastolic component compared to the height of the systolic component, and the SI is defined as the subject height divided by the PPT.

$$RI = \frac{a}{b} \times 100\% \quad (1.2)$$

$$SI = \frac{\text{Subject_Height}}{PPT} \quad (1.3)$$

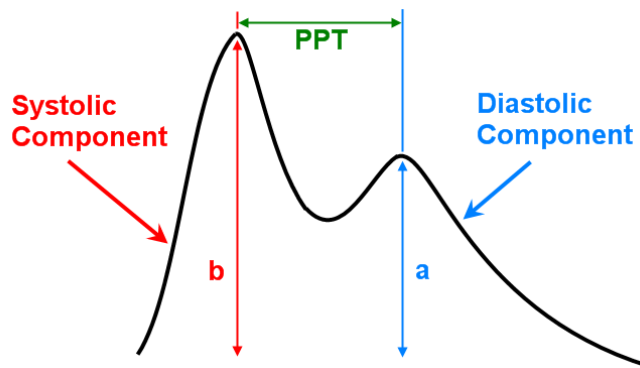


Figure 2. Parameters obtained from digital volume pulse analysis [14].

PWV can be expressed as a function of arterial elasticity (E) via the Moens-Kortewea equation [4]:

$$PWV = \sqrt{\frac{h \cdot E_{inc}}{2 \cdot r \cdot \rho}} \quad (1.4)$$

where h is the arterial wall thickness, E_{inc} is the incremental elastic modulus, r is the lumen radius, and ρ is the blood density.

Respiration-induced fluctuations are visible in a long-duration photoplethysmogram with pulsatile features that slowly shift upwards and downwards. The reliability of extracting respiratory rate using this type of waveform has been confirmed [15-17], and one straightforward approach is to seek the dominant frequency component in its low frequency spectrum. Intuitively, the fluctuation phenomenon is caused by the effects of ventilation on the cardiovascular system; however, there is still not a detailed physiologic explanation for the respiration-induced change in the volumetric signal. Possible reasons include direct transmission of arterial blood pressure changes, episodic sympathetic outflow and local autoregulation, and venous volume fluctuations [8, 18, 19].

Simultaneous recordings of respiration and blood flow signals from the subclavian and femoral veins show the consistency of their pulsatile rates and the Valsalva maneuver response [6]. With the factors that (a) veins and arteries are distributed hand in hand and (b) veins are closer to the skin and therefore to a reflectance pulse oximeter sensor, it is believed that venous volume pulse information will be embodied in the photoplethysmographic signal, as in Figure 3. Hence, by processing low-frequency oscillations due to fluctuations in venous volume, venous parameters could be obtained that map to traditional arterial parameters, e.g., venous blood oxygen saturation (SvO_2) as compared to arterial blood oxygen saturation (SpO_2). Furthermore, the metabolic rate at the measurement site could be estimated using the difference between the SpO_2 and SvO_2 values.

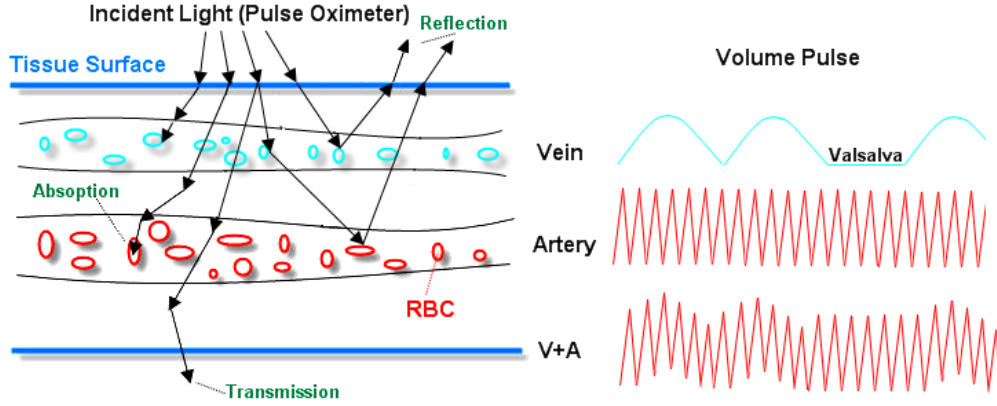


Figure 3. Respiration-induced venous volume pulse and arterial volume pulse. Their combined volume signal is demonstrated as V+A.

The perfusion index (PI), defined as the ratio of the pulsatile amplitude (AC) of a PPG to its baseline value (DC) is reported as an index sensitive to proximal sympathectomy [8]. With PI s calculated for the red and near-infrared channels, the calibration coefficient (R) for a pulse oximeter can be written as

$$R = \frac{PI_{red}}{PI_{ir}}, \quad (1.5)$$

where SpO_2 (%) = $AR + B$ (A and B are experimentally determined scalars).

Photoplethysmograms are also influenced by ambient light and the motion of a pulse oximeter relative to the measurement site. Ambient light is often deterministic and high frequency, e.g., 120 Hz flicker from full-wave-rectified fluorescent room lights, which could be useful to monitor room illumination and device appendage conditions (e.g., if the device is not placed by a patient, more ambient light tends to be picked up by the sensor). Motion artifact is typically stochastic and low frequency. Although much research has been focused on motion artifact reduction [20-28], motion information could prove helpful, e.g., to monitor a patient's activity level after a surgery.

The aforementioned parameters have not considered cycle-to-cycle variation in a pulsatile waveform and waveform morphological variations due to different measurement locations and vascular profiles. Hence, additional potential clinical parameters may be derived from photoplethysmographic signals yielded by a competent pulse oximeter.

Designing a Novel and Competent Pulse Oximeter

Interpreting the photoplethysmogram and extracting physiological parameters from the pulsatile waveform normally reside in the field of biomedicine or physiology, while designing pulse oximeter hardware and firmware usually relies on electrical engineering. Communication barriers and other hurdles between the two fields prevent physiologists and clinicians from obtaining high-fidelity measurement data and consequently research and diagnostic results. Most commercial pulse oximeters do not show the baseline variations in a pulsatile signal, and the waveforms displayed on their front panels have already been processed in an unspecified manner. Additionally, their sensors typically work in transmittance mode, and therefore measurement sites are limited to fingertips and earlobes.

A well-designed sensor module is essential for reliable parameter extraction from photoplethysmograms. It should provide high quality PPG data and support multiple measurement locations, i.e., in reflectance mode. The general characteristics for such a high-fidelity reflectance pulse oximeter are outlined in Table 2 with respect to these broader categories: the signal, LED/detector, functionality, and miscellaneous.

In this thesis, a pulse oximeter competent in high-fidelity data acquisition is presented that employs a novel control system and a wireless communication link. Four channels of signal data are generated simultaneously in real-time at a high sampling rate and amplitude bit depth. *Chapter 2* discusses technical issues for such a well-designed pulse oximeter, and the corresponding methods are also described. Two versions of the prototype hardware are devised from schematic creation to firmware development in *Chapters 3* and *4*. The performance and practical applications of the novel module are described in *Chapters 6* and *7*.

Table 2. Characteristics of a high-fidelity reflectance pulse oximeter.

Signal	
○ Distortion	Avoid with a filter-free design
○ Digitization level	Thousands of peak-to-peak levels
○ DC removal	Digital operational circuitry
○ Sampling frequency	High enough to avoid aliasing of signal and artifact data
○ Noise and artifact	Removable and resistant (high signal-to-noise ratio)
○ Data availability	Full access to all signal flows and uninterrupted sampling and acquisition
LED/Detector	
○ Geometry	Radial arrangement, central excitation sources, and large area detectors
○ Flat sensor profile	Improve signal quality and reduce motion sensitivity
○ Separation	3-5 mm to maximize the AC/DC ratio and optimize detection of photons that have traveled deeper into perfused tissue
Functionality	
○ Communication	Wireless (range: 10 m) and Universal Serial Bus (USB)
○ Local storage	Onboard memory module
○ Battery	Multi-day lifetime and rechargeable
○ Client software	Signal visualization and device control panel
Miscellaneous	
○ Location	Multiple body locations; gather signal independent of vascular and perfusion profile
○ Wearability/usability	Comfortable and easy to use
○ Cost	Low (~\$100)

CHAPTER 2 - System and Methods

This chapter begins with a brief introduction to the new pulse oximeter system's functional layout for a better understanding of the technical issues that follow. These technical issues and the corresponding design approaches are described in a yet-to-be published work [29], which will not be further cited in the following text and figures.

System Layout at the Circuitry Level

Figure 4 shows the block diagram for the high-fidelity reflectance wireless pulse oximeter circuitry. The microprocessor coordinates all operations, including photoplethysmographic signal excitation, control, processing, and transmission/storage.

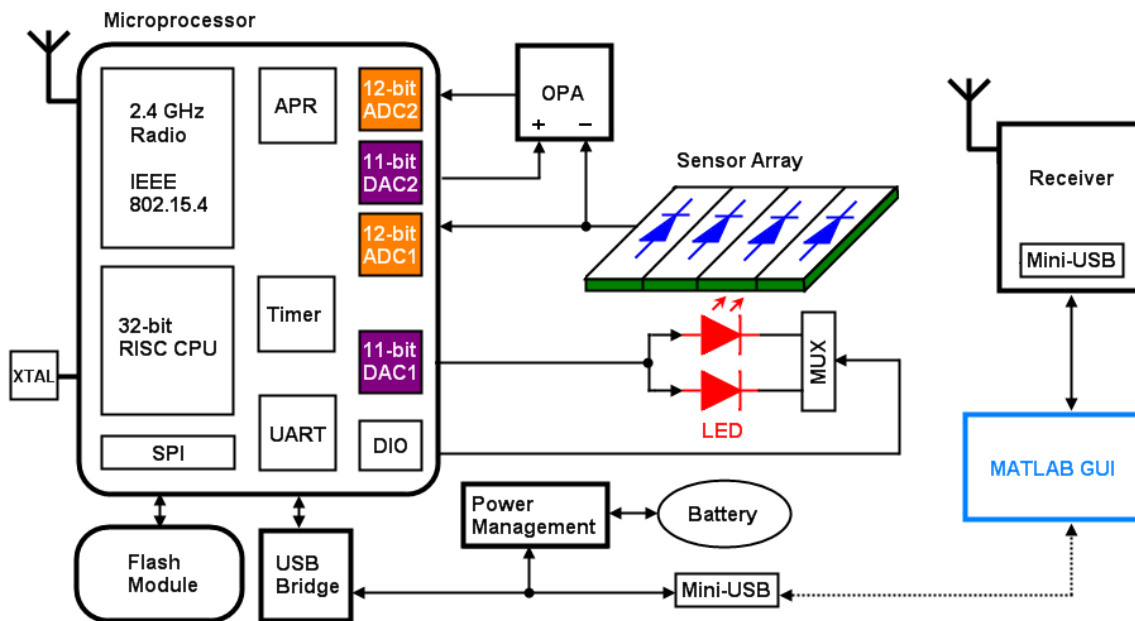


Figure 4. System layout at the circuitry level.

The basic signal excitation and collection circuitry are entirely controlled by the microprocessor, which has two 11-bit digital-to-analog converters (DACs), two 12-bit analog-to-digital converters (ADCs), and digital input/output ports (DIOs). With the cooperation of the DIOs and DAC1, the bi-color excitation LED generates alternating red and near-infrared light pulses to induce the two photoplethysmographic signals from blood perfused tissue. The

reflected signals are then collected by the sensor array, where the first-stage signals form and are sampled by ADC1. Given the positive input from DAC2 and the negative input from the first-stage signal, the differential operational amplifier circuitry (OPA) generate the second-stage signal that is sampled by ADC2. In summary, each first-stage signal contains both AC and DC components, whereas each second-stage signal contains only AC data (the DC baseline has been removed, and the remaining AC portion has been amplified to span a large portion of the ADC2 range).

No filter circuitry are introduced in the signal acquisition process. Full control of the process, which incorporates a high fidelity and flexible control system, will be introduced later. The battery (unstable power source) is isolated from the photoplethysmographic excitation and collection circuitry, since it is powered by the analog peripheral regulator (APR) inside the microprocessor.

Normally, the pulse oximeter (transmitter) uses a wireless link to communicate with a receiver, and the data are stored on a PC running a MATLAB graphical user interface (GUI). A mini-USB connection on the pulse oximeter can also be used to communicate with a PC directly while the battery is being recharged. If neither the wireless link nor the USB connection is available, the sampled data will be temporarily stored on the flash memory module (offline mode).

Shift Resistance

The first-stage photoplethysmographic signal consists of a large DC portion and a small AC portion, as in Figure 5. The goal is to extract the second-stage signal (AC) by eliminating the DC component. If the DC portion is not removed, then maintaining many digitization levels in the AC signal (usually hundreds to thousands) over that small voltage range requires an ADC of very high precision, which is not recommended for a low-voltage and low power consumption device. This extraction (DC removal) process is executed by the OPA unit. Its role is expressed in Equation 2.1, where S_1 and S_2 are the first-stage and second-stage signal respectively, G is the gain of the OPA, and V_{ref} is a reference voltage that functionally equates to the DC signal level. In order to show the photoplethysmographic waveform peak during systole as with a blood pressure curve, V_{ref} is hooked up to the positive pin of the OPA, effectively ‘flipping’ the AC signal vertically before it is digitized.

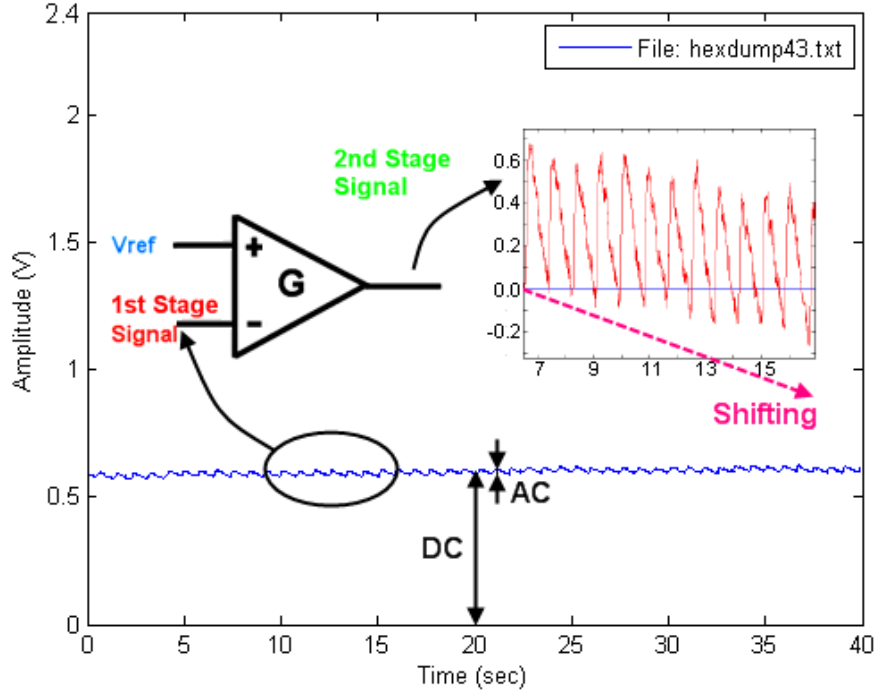


Figure 5. The first-stage signal with a large DC portion enters the differential amplifier with gain G to obtain the second-stage photoplethysmographic signal.

$$S_2 = G \times (V_{ref} - S_1) \quad (2.1)$$

Nevertheless, S_1 does not remain stable all of the time, as both the AC and DC level can be easily influenced by intrinsic blood flow inconsistency, extrinsic motion, respiration, background light, etc. All of these factors cause shifting of the second-stage signal. The input voltage range of the 12-bit ADC is set to 0-2.4 V, which is also designated as the sampling window, so one digitization level is defined to be $2.4 \text{ V} / 4096 \text{ levels} = 0.586 \text{ mV}$. Given the gain $G = 30$ and a constant V_{ref} , one digitization level increment in the DC signal results in a decrement of 30 digitization levels in the output according to Equation 2.1. As in Figure 3, the second-stage signal shifts 0.3 V (512 digital levels) in 10 seconds, which is unacceptable because the signal will eventually saturate at the lower bound of the sampling window, and clipped data cannot be sampled by the ADC, which leads to signal corruption.

Equation 2.1 implies three ways to address this issue: adjust either the first-stage signal, V_{ref} , or the gain. In this effort, a V_{ref} adjustment method is employed to resist the shifting. The

reason for this choice is that the value of V_{ref} is outputted by the DAC, which can be controlled by the firmware developer. Hence, a moving average filter is employed to estimate the DC component (V_{DC}) in real-time, and V_{ref} is defined as

$$V_{ref} = MA(t) + V_+ \quad (2.2)$$

where $MA(t)$, the DC estimator, equates to an N -point moving average result of the first-stage signal at time t . V_+ is added to $MA(t)$ to ensure that V_{ref} is always greater than the first-stage signal and to ensure that the second-stage signal is positive.

Although V_{ref} typically varies slowly (several seconds per digitization level in an environment with minimal motion and ambient noise), the discrete adjustment leads to a discontinuity in the second-stage photoplethysmographic signal. Hence, the V_{ref} data must also be transmitted or stored along with the photoplethysmographic data so as to restore the original photoplethysmographic signal. This process is designated as compensation in this thesis.

Figure 6 shows an experimental data set from the palm. The collected data are compensated to remove the discontinuities caused by V_{ref} jumps in the pulsatile waveform using the following method. Plug Equation 2.1 into Equation 2.2, then rearrange the result to isolate the first-stage signal S_1 :

$$S_1 = MA(t) + V_+ - \frac{S_2}{G} \quad (2.3)$$

The compensated second-stage signal, \hat{S}_2 , can be defined as

$$\hat{S}_2 = G \times (V_{DC} + V_+ - S_1) \quad (2.4)$$

Then, substituting Equation 2.3 into Equation 2.4 yields

$$\hat{S}_2 = S_2 - G \times (MA(t) - V_{DC}) \quad (2.5)$$

Typically, DC is an unknown constant, but it is okay to initially set $V_{DC} = MA(t_0)$ and define

$V_{jump} = MA(t) - MA(t_0)$ so that Equation 2.5 becomes

$$\hat{S}_2 = S_2 - G \times V_{jump} \quad (2.6)$$

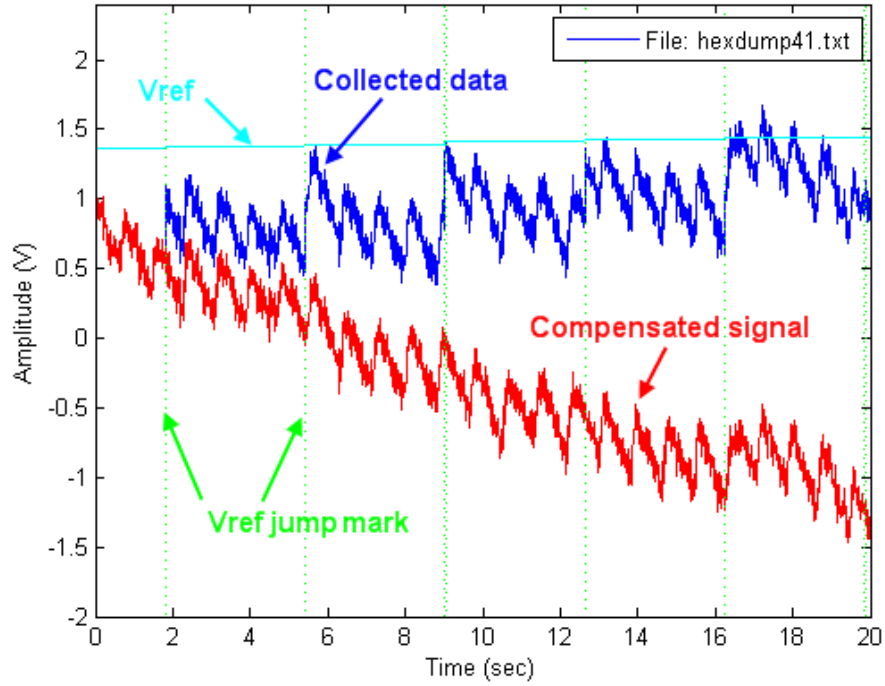


Figure 6. Palm measurement site data with compensation demonstration.

By utilizing this method, the photoplethysmographic signal can be completely restored as long as the second-stage signal is not saturated. The V_{ref} adjustment effectively resists the shifting of the first-stage signal. Additionally, V_{ref} is usually considered equal to V_{DC} to calculate the blood oxygen saturation level.

Control System

Figure 7 illustrates the control system for photoplethysmographic signal collection to demonstrate how the high-fidelity photoplethysmographic signal is formulated. In the control flow block diagram, incident light from the LED penetrates into the underlying blood perfused tissue. The reflected light collected by the photodiode array (PD) is converted to the first-stage photoplethysmographic signal, which forks into three branches. The first branch directly connects to the operational amplifier circuitry (OPA). The second branch connects to the V_{ref} generator unit that essentially is a V_{DC} estimator that implements a moving average filter. The

third branch contributes to a feedback loop. The OPA yields the second-stage photoplethysmographic signal.

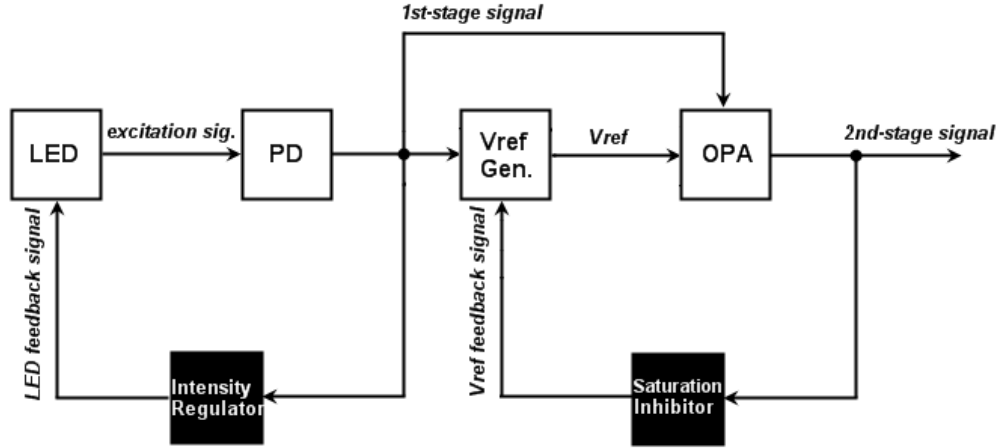


Figure 7. Control flow for the pulse oximeter with feedback functionality (black blocks).

Two black control blocks embody the two feedback loops in Figure 7. The LED intensity regulator (left) maintains the amount of reflected photons at the optimal level, independent of a subject’s vascular and perfusion profiles. The saturation inhibitor (right) ensures that the second-stage signal falls in the ADC’s sampling window and restrains its shifting behavior by adjusting the component V_+ of V_{ref} .

To keep the signal’s high-fidelity quality, the sensitivity of the LED intensity regulator should be set to low. Once a different value is yielded by the LED intensity regulator, the influence on the first-stage signal converted by the PD will be impossibly formulated because the blood perfused tissue between the LED and the PD is viewed as an unknown system. On the other hand, the sensitivity of the saturation inhibitor should be set to high to ensure a rapid response to the signal shifting. Since this adjustment only influences V_{ref} , the primitiveness of the photoplethysmographic signal is guaranteed, and the second-stage signal can be compensated using the same Equation 2.6.

The signal-to-noise ratio (SNR) compares the level of a desired signal to the level of ambient noise. In a controlled scenario, variations in ambient noise level can be neglected. If the desired signal increases as the LED intensity increases, the SNR will consequently improve.

However, this method results in a saturation risk due to a second-stage signal with too large of a magnitude within a fixed sampling window, in spite of the aforementioned shift-resistant method. Additionally, an LED with stronger intensity consumes more power. Hence, an optimized intensity level should be empirically predetermined as the reference for the intensity regulator.

Removable Noise

In an environment with grid-powered equipment, the ambient light is considered to be 60 Hz (i.e., from the USA electricity grid) and usually its harmonic noise, such as 120 Hz flicker in fluorescent lights due to a full-wave rectified 60 Hz signal. Normally, the information in a photoplethysmographic signal resides in the range of 0-30 Hz. According to the Nyquist-Shannon sampling theorem, the lower bound of the sampling frequency (f_s) is then 60 Hz, but to prevent frequency aliasing caused by ambient noise, sampling frequencies of 240 Hz or higher are required.

Figure 8 shows the frequency spectrum of a segment of photoplethysmographic data with ambient noise. The heart rate component is 1.329 Hz, and its harmonics dominate in the frequency band below 20 Hz. As frequency increases, some noise stands out at 60.02 Hz, 84.43 Hz, and 120.1 Hz. However, this noise is removable by signal post-processing as long as the sampling frequency is high enough to prevent frequency aliasing.

The realization of a high sampling frequency requires the microprocessor to have a high clock frequency, small timer cycle, rapid analog-to-digital and digital-to-analog conversions, and properly designed firmware. However, the bandwidth of the serial communication or wireless communication link may limit the maximum sampling frequency. Usually, a properly designed shield or cover can effectively reduce ambient noise, and a low pass filter can also clean the photoplethysmographic signal.

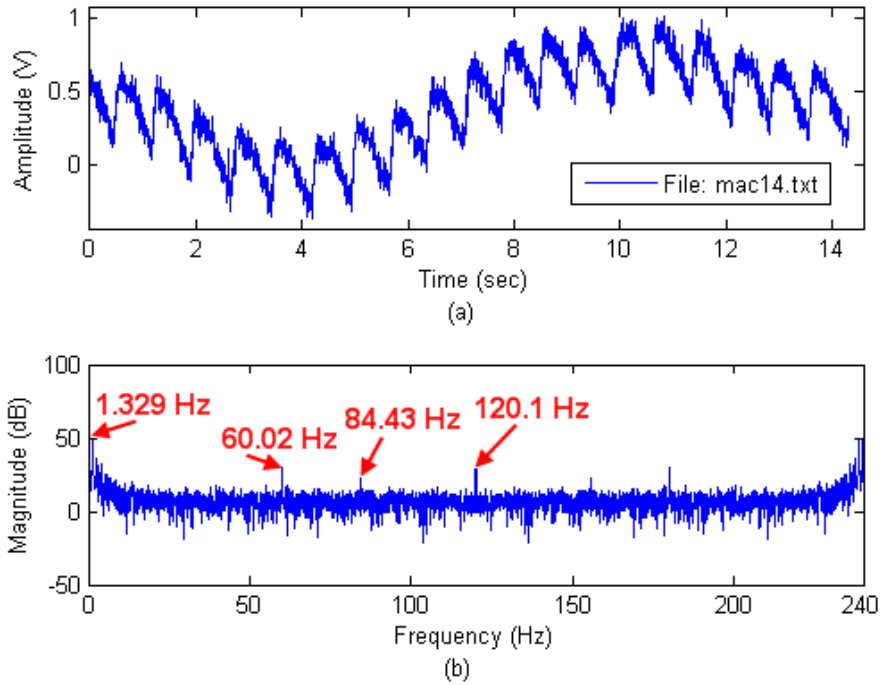


Figure 8. An example of removable noise. (a) Photoplethysmographic waveform (compensated) corrupted by ambient noise. (b) Frequency spectrum of the 14 seconds of data sampled at 240 Hz.

Motion Artifact

Motion artifact is always an issue for a pulse oximeter, and it is more of a problem for a pulse oximeter working in reflectance mode, as noted in [30]. Much existing literature is focused on signal processing for the reduction of motion artifact and the restoration of the photoplethysmographic signal. Most of those methods are based on the fact that there is enough information in the corrupted photoplethysmographic signal for recovery. If motion is severe, saturation will occur frequently and last for some time, leading to information loss.

Motion artifact can be considered special signal shifting. In this thesis, we seek a shift-resistant method (V_{ref} adjustment) and do not purport to address motion processing. Motion artifact is classified into two categories: slight and severe. Figure 9 demonstrates an example of the severe condition characterized by three axes of hand motion. The movement is within a 10 cm range and at around a 1 Hz rate. The photoplethysmographic signal is severely corrupted,

including being saturated on both sides of the sampling window, with many segments losing the AC information and being therefore unrecoverable.

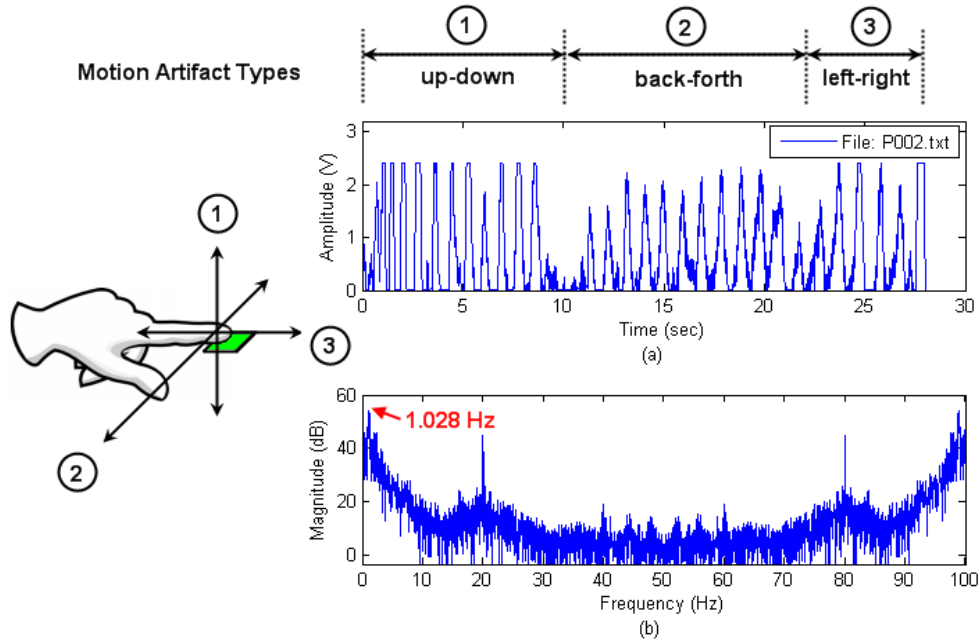


Figure 9. (a) Photoplethysmographic waveform severely corrupted by three axes of hand motion artifact. (b) Frequency spectrum of 28 seconds of data sampled at 100 Hz.

The slight condition refers, e.g., to slow body movement, where the photoplethysmographic signal still maintains its general shape but oscillates more violently relative to the still condition. To reduce this type of motion artifact, the shift-resistant method is promising and takes effect by setting the optimal rate and window size for the V_{ref} adjustment. The DAC assigns the V_{ref} value to the positive pin of the amplifier, and that voltage remains the same until the next cycle of assigning V_{ref} to the DAC. Obviously, the window size of the moving average filter (the DC estimation time delay) and the rate of assigning V_{ref} to the DAC (**not** the rate of V_{ref} variation) will influence the second-stage signal. An extreme example is that if the window size $W = 1$ and the assignment rate $R = f_s$, motion artifact will never happen since $MA(t) \equiv S_1$ and consequently $S_2 = G \times V_+$ according to Equations 2.1 and 2.2.

Figure 10 shows three experimental records acquired under an analogous condition (exaggerated deep respiration activity) with different rates and window sizes. Only subplot (a)

has a good presentation of the photoplethysmographic signal with slight shifting. A lower rate (b) or wider window size (c) causes the signal to shift severely, and some segments are almost saturated. Hence, the empirical parameter pair ($W = 256, R = f_s$) is adopted for V_{ref} adjustment.

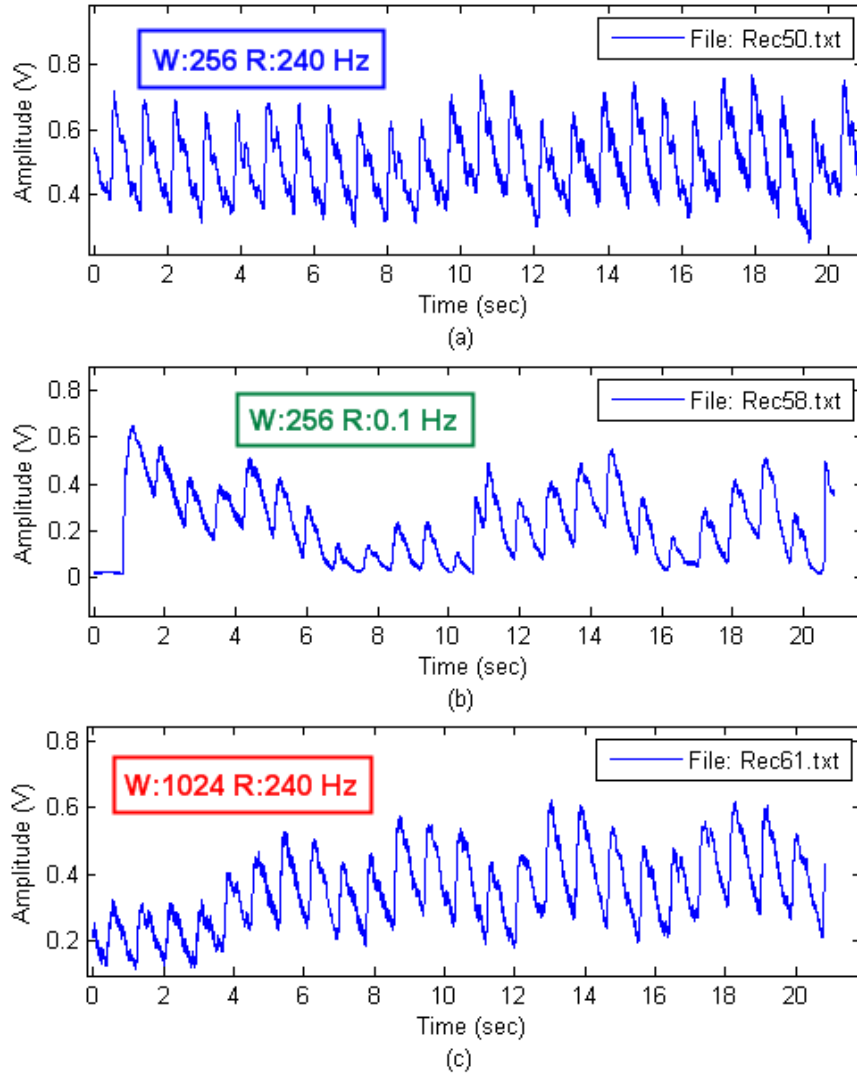


Figure 10. Three photoplethysmographic signals (uncompensated) under an analogous slight motion condition but with different parameter pairs (W, R), where W refers to the window size of the moving average filter, R refers to the rate of assigning V_{ref} to the DAC, and $f_s = 240$ Hz.

Calibration Approach

A calibration curve is needed to create a relationship between the calibration ratio, R , and the blood oxygen saturation level, SpO_2 , and a commercial pulse oximeter (Smiths Medical BCI[®] 3180) is employed to achieve the calibration work. Although (a) each pulse oximeter manufacturer uses a unique calibration curve with an SpO_2 accuracy specification usually equal to $\pm 1\%$ standard deviation relative to an actual measured SaO_2 [31], and (b) the curve is not necessarily a straight line even for a narrow domain, normally a linear empirically-determined equation is used for gross estimation, and it can be expressed as

$$SpO_2(\%) = a \times R + b \quad (2.7)$$

where (a, b) is a constant-coefficient pair, such as the published pairs (-25, 110) [32] and (-25.6, 118.8) [33].

An overdetermined system, Equation 2.8, is built by n measurements, where R_i and the corresponding SpO_{2i} values are read from the BCI[®] 3180 ($i = 1, 2, \dots, n$):

$$Mx = y \quad (2.8)$$

where $M = \begin{bmatrix} R_1 & R_2 & \mathbf{L} & R_n \\ 1 & 1 & \mathbf{L} & 1 \end{bmatrix}^T$, $x = [a \ b]^T$, and $y = [SpO_{21} \ SpO_{22} \ \mathbf{L} \ SpO_{2n}]^T$. Hence,

the least-squares approximate solution is

$$x = (M^T M)^{-1} M^T y \quad (2.9)$$

And the standard deviation is indicated by

$$s = \frac{\|y - Mx\|}{\sqrt{n}} \quad (2.10)$$

Power Consumption

For a pulse oximeter that needs to run wirelessly for a long time (such as a day) or save data on a flash module, a battery with adequate capacity is needed that challenges the size of the hardware package. Two primary ways were adopted to address this issue. The mini-USB connection is employed to power the pulse oximeter when needed, through which the battery is also being recharged. A lithium-ion battery is also employed, for it has the highest power density of all batteries on the commercial market on a per-unit-of-volume basis [34]. Another approach

is to optimize the firmware of the microprocessor to lower the average power consumption. Excitation LED illumination, wireless communication, and access to the flash module require the majority of the total power, which was confirmed in [35]. Appropriate control of the LED and the communication process is essential to save power, which will be discussed further in *Chapter 4-Firmware Development*. For the firmware development, sufficient system resources (CPU time and RAM) are reserved for a decision-making algorithm that roughly assesses the viability of the PPG signal. Since entering the sleep mode costs almost no power for the microprocessor, a decision-making algorithm will, in practice, be helpful to the system; this will be discussed further in *Chapter 7-Feature Detection*.

CHAPTER 3 - Hardware Development

This chapter describes the hardware development process for the wireless reflectance pulse oximeter module. After careful selection of a microprocessor and a wireless communication protocol, the first version was designed with circuitry and components referenced to a previous module [36]. The second version features improvements in automatic LED intensity regulation and photodiode voltage saturation inhibition.

The two versions exhibit similar circuitry and electronic parts listings, and their differences are depicted in detail. Hardware schematics, printed circuit board (PCB) layouts, and electronic parts lists are included in *Appendices A, B, and C*, respectively.

Microprocessor and Wireless Link

The first step in the design was selecting a suitable wireless-integrated microprocessor module. After comparing the specifications of six common wireless medical protocols [37], we selected IEEE 802.15.4 for this new pulse oximeter design because of its low power consumption, adequate data rate, and suitable transmission range. Off-the-shelf development toolkits are also widely available for this standard, and numerous mesh network topologies already exist that can utilize IEEE 802.15.4, including ZigBee and 6LoWPAN, which enables efficient IPv6 communication [38]. In the end, the Jennic JN5139 wireless microcontroller was employed. The JN5139 module and its development toolkit were provided directly by Jennic, which contributed to a convenient and fast design procedure.

The JN5139 is a low power, low cost wireless microcontroller suitable for IEEE 802.15.4 and ZigBee applications. The device integrates a 32-bit RISC processor with a fully compliant 2.4 GHz IEEE 802.15.4 transceiver, 192 kB of ROM, 96 kB of RAM, and a rich mixture of analog and digital peripherals, as depicted in Figure 11. The main features of the transceiver and microprocessor are listed in Table 3 [39].

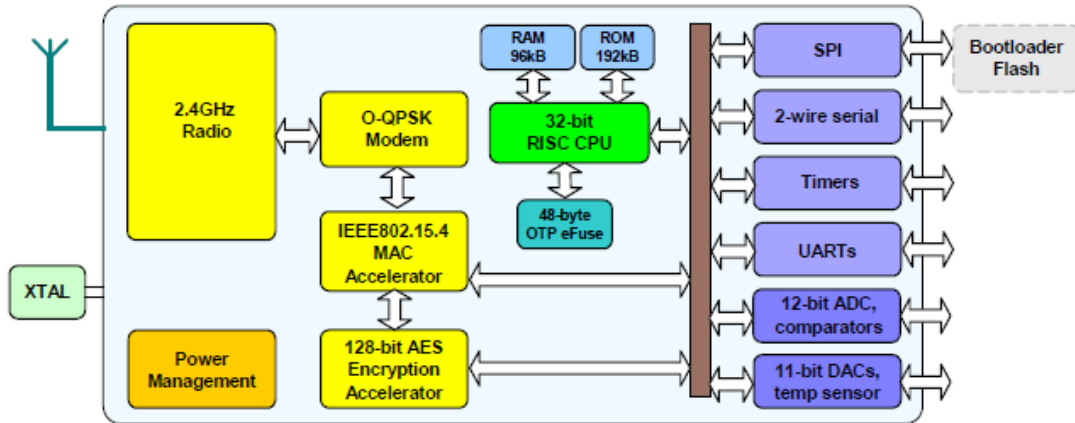


Figure 11. Block diagram of the JN5139 chip [39].

Table 3. Features of the JN5139 transceiver and microprocessor.

Transceiver	Microcontroller
<ul style="list-style-type: none"> ○ 2.4 GHz IEEE 802.15.4 compliant ○ 128-bit AES security processor ○ MAC accelerator with packet formatting, CRCs, address checks, auto-acks, and timers ○ Integrated power management and sleep oscillator for low power ○ On-chip power regulation for 2.2 V to 3.6 V battery operation ○ 60 nA deep sleep current ○ 1.2 μA sleep current with active sleep timer ○ 37 mA RX current ○ 38 mA TX current ○ -97 dBm receiver sensitivity ○ +3 dBm transmit power 	<ul style="list-style-type: none"> ○ 32-bit RISC processor that sustains 16 MIPS at low power ○ 192 kB ROM - stores system code including the IEEE 802.15.4 MAC ○ 96 kB RAM - stores system data and optionally bootloaded program code ○ 48-byte OTP eFuse supporting AES based code encryption ○ 4-input 12-bit ADC; 2 11-bit DACs; 2 comparators ○ 2 Application timers/counters; 3 system timers ○ 2 UARTs (one for debugging) ○ SPI port with 5 selects ○ 2-wire serial interface ○ Up to 21 DIO ports

The module that uses Jennic’s JN5139 chip is illustrated in Figure 12. It provides a comprehensive solution with a high-performance radio and includes all radio-frequency components. “All that is required to develop and manufacture wireless control or sensing products is to connect a power supply and peripherals such as switches, actuators, and sensors, considerably simplifying product development.” [40]. The pin configurations of the JN5139 module and their functions are presented in *Appendix D*.

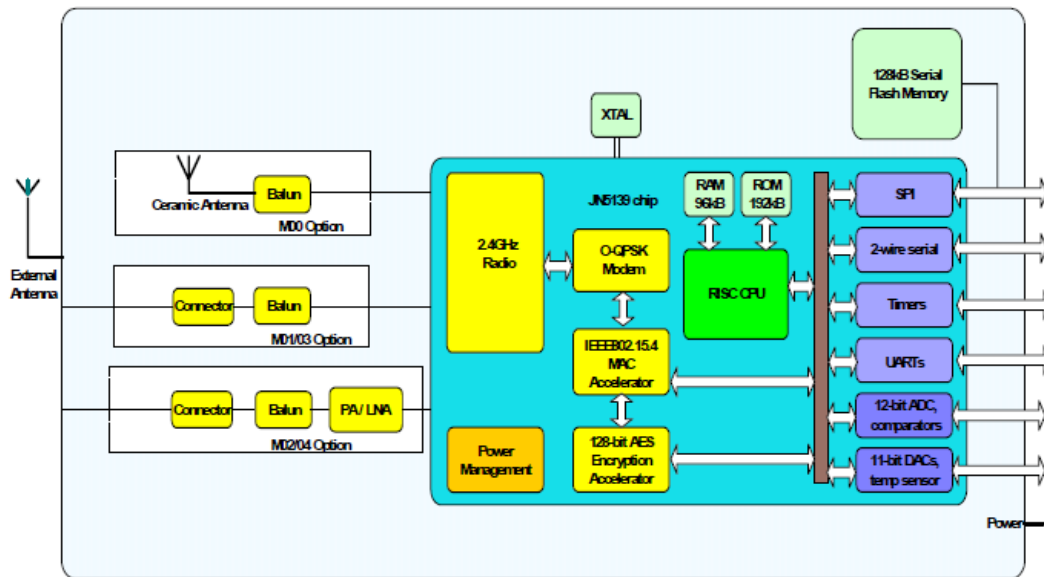


Figure 12. Block diagram of the JN5139 module [40].

The Jennic DR1080 board, supplied with the Jennic JN5139-EK020 Starter Kit, provides a platform to mount modules which contain Jennic wireless microcontroller products, providing a hardware development environment for wireless network applications. It offers the same pins as the JN5139 module, as in *Appendix D*, through its J4 expansion connector [41].

This toolkit is especially helpful during the first-stage of firmware development. Several jumper wires were hooked up between a J4 connector and the LED and photodiode circuitry on the previous module [36]. This test setup helped to ensure the successful functioning of the final manufactured prototypes.

Version 1 Circuitry Design

Schematic creation and PCB design were completed with CadSoft's Eagle Layout Editor Freeware version 5.2. The pulse oximeter hardware is divided into five modules according to their functionality on the board: microprocessor, excitation LED, signal sampling, power management, and other auxiliary circuitry.

The microprocessor module is the kernel of the prototype. The JN5139 wireless module, which is designed for robust and secure low power wireless applications, is illustrated in Figure 13. It connects to all of the other four parts with the tagged green wires, which correspond to the wires with the respective tag names in the other schematics. A minimum connection is also required for successful startup and to program the microprocessor, as summarized in Table 4 [42].

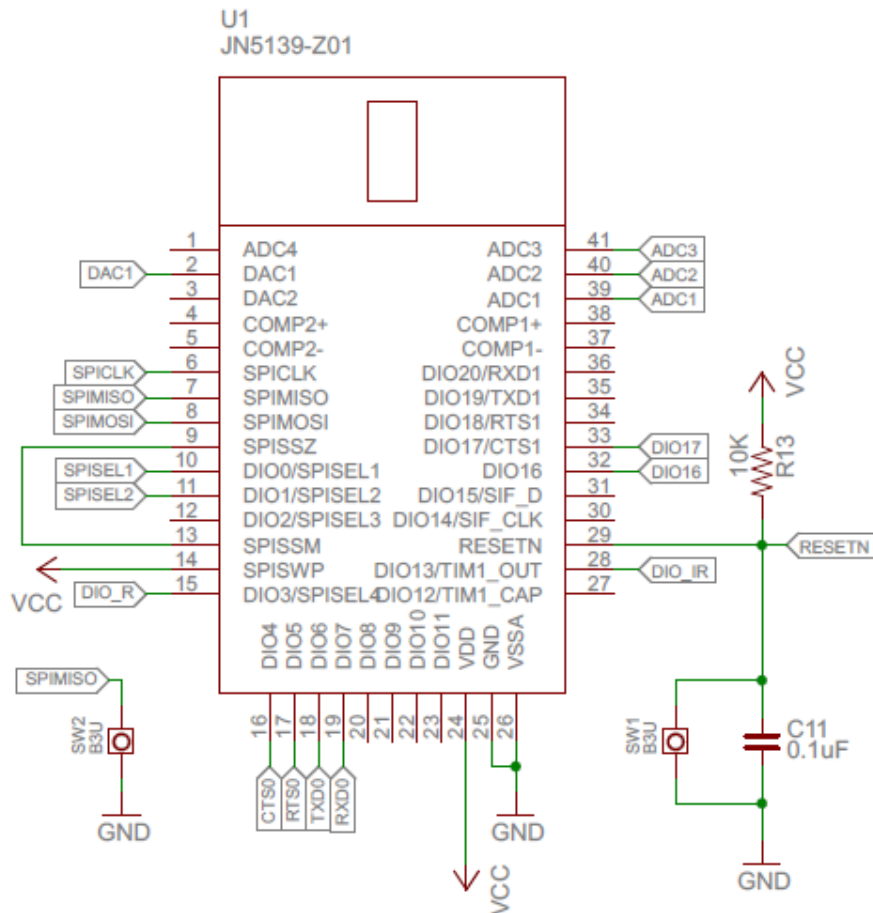


Figure 13. Microprocessor module schematic.

Table 4. Minimum connection required for the microprocessor module (from [42]).

- Connect power and ground on pins 24 (VDD), 25 (GND) & 26 (VSSA).
 - Ensure that pins 9 (SSZ) and 13 (SSM) are tied together. This allows the SPI Select signal from the JN5121 device to communicate with the FLASH.
 - Disable the write protect on the FLASH by tying pin 14 (SWP) HIGH.
 - To ensure correct power up, the reset circuit must be applied to pin 29 (RESETN). If required a switch can be applied between RESETN and GROUND.
 - At power up or reset the Boot Loader first looks at pin 7 (MISO) to determine whether to go into programming mode. To enter programming mode, pin 7 (MISO) must be held LOW at power up or reset and then released.
 - Serial communications are made on pins 18 & 19 (TXD, RXD). These signal levels must be level shifted to 3.3V.
 - Some terminal programs, e.g., HyperTerminal, pull the serial PGM/RTS line down by default, thus setting the device into programming mode at power on/reset. After programming, when powering on the module, ensure you have quit or disconnected HyperTerminal or disconnect the serial lead.
-

The excitation LED module of prototype version 1 utilizes API's PDI-E837 660 nm/880 nm dual excitation source with a typical forward current of 20 mA. Because the typical forward voltages for the two channels are 1.8 V and 1.3 V, respectively, a trim potentiometer is serially connected to each channel to compensate for the voltage difference. The shortcoming of a manual LED intensity adjustment is that it requires a trimming operation prior to each measurement if the vascular profile at the measurement location changes too much (e.g., when a new user places the sensor), a situation that is conquered in version 2.

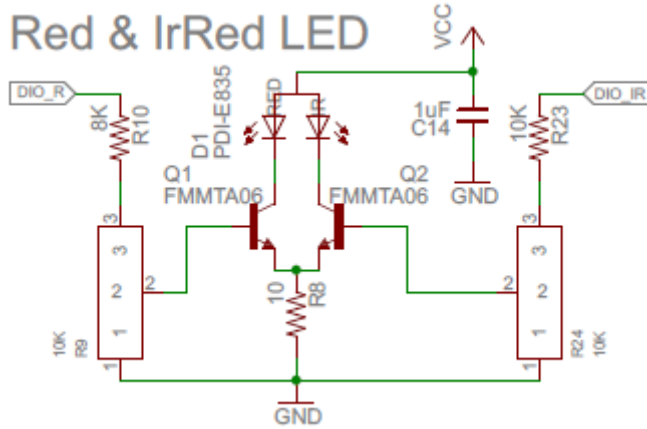


Figure 14. Red & near-infrared excitation LED module schematic.

The signal sampling module consists of operational amplifier circuitry connected to the sensor array. Four API PDV-C173SM high-speed photodiodes are hooked up in parallel with a good responsivity ($> 0.3 \text{ A/W}$) to wavelengths greater than 650 nm. The OPA chip contains two amplifier units. The signal yielded by the sensor array is buffered at the first unit and amplified at the second unit. The outputs of the two units are sampled by ADC1 and ADC2, respectively. DAC1 provides the reference voltage (estimated from ADC1) that is used to remove the baseline of the first-stage signal.

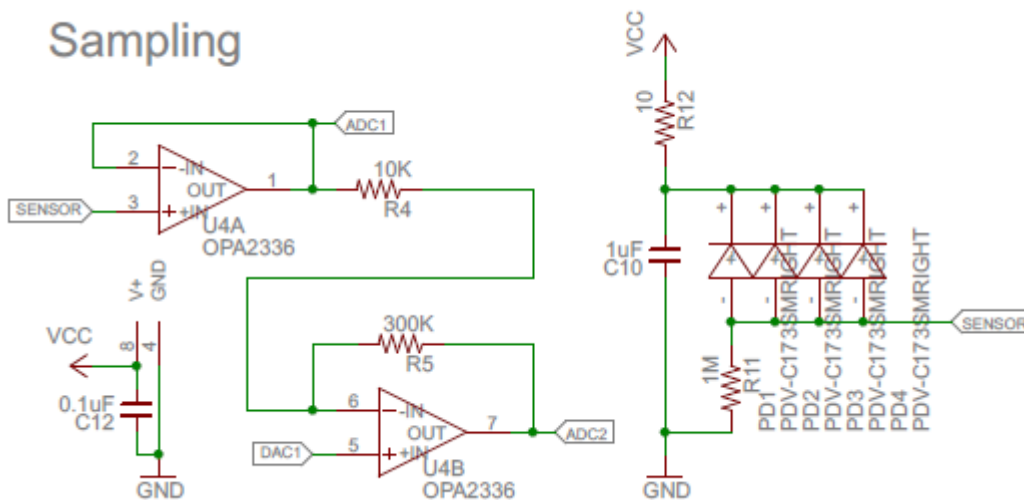


Figure 15. Signal sampling module schematic.

The power management module includes two chips: (1) a Silicon Labs CP2102 USB-to-UART bridge that powers the pulse oximeter when the USB connection is detected and bridges data communication to the host and (2) a STMicroelectronics L6924D battery charger system with an integrated power switch for lithium-ion batteries which charges the battery when the USB connection is detected. A LIR2477 3.6 V Li-Ion rechargeable button cell with a capacity of 180-200 mAh serves as the power source when the USB connection is absent. SW3 selects the power source for the whole device whether the USB (VDD) or battery (VBAT) source is in use.

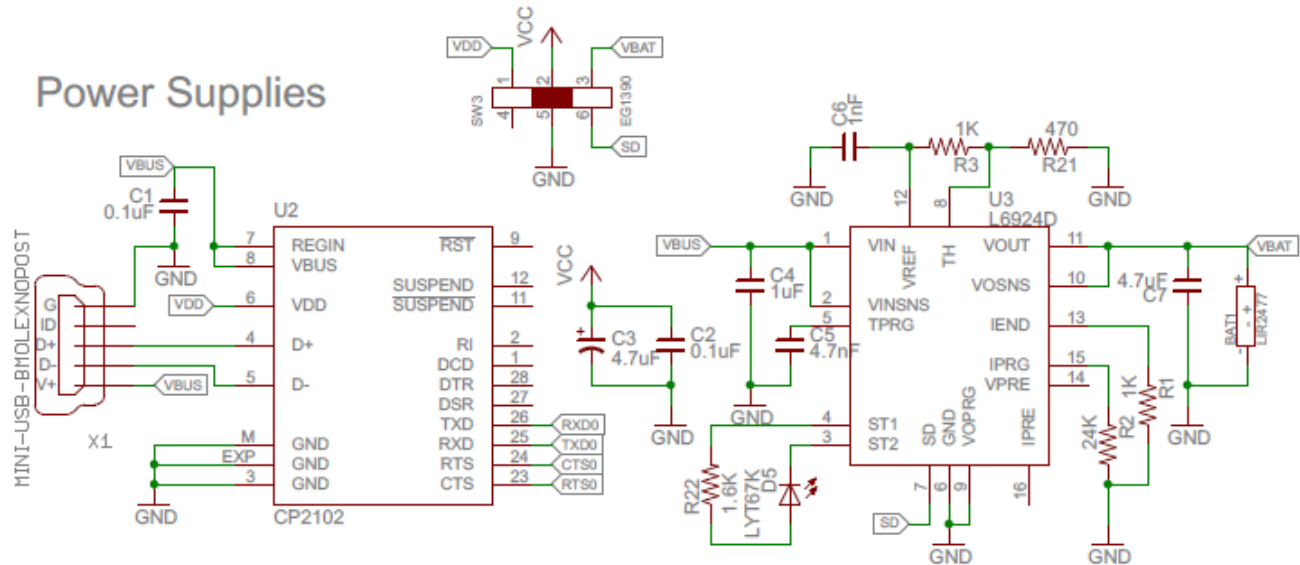


Figure 16. Power supply and management module schematic.

Other electronic components housed on the board include memory chips, indicators, and buttons. Two Numonyx M25PX64 64-Mbit flash memory chips with SPI bus interfaces provide storage space when the pulse oximeter works in offline mode; each consumes 20 mA of current while being accessed. The light wavelength selected for the display LED should be far from (a) the wavelengths of the red and near-infrared excitation LEDs utilized for signal excitation and (b) the sensitivity peak of the detector photodiodes so as to minimize interference.

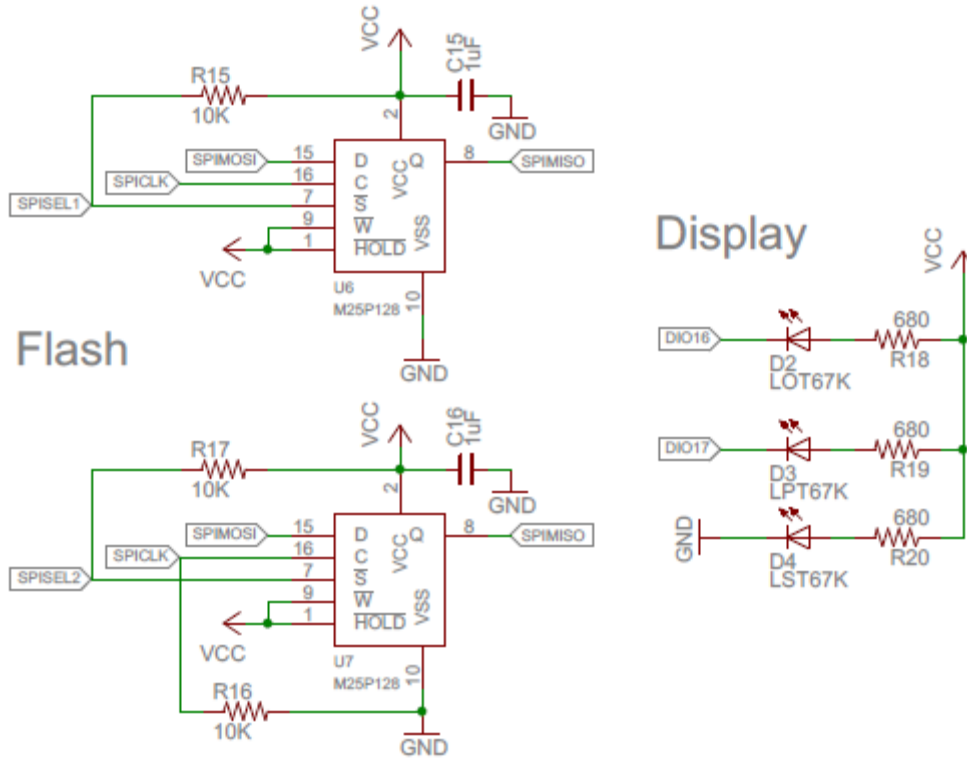


Figure 17. Flash memory and display LED module schematic.

Version 2 Circuitry Design

Version 2 shares the majority of the circuitry with version 1. The most significant difference is that it brings in a new LED intensity control module and a modified signal sampling module, as demonstrated in Figure 18.

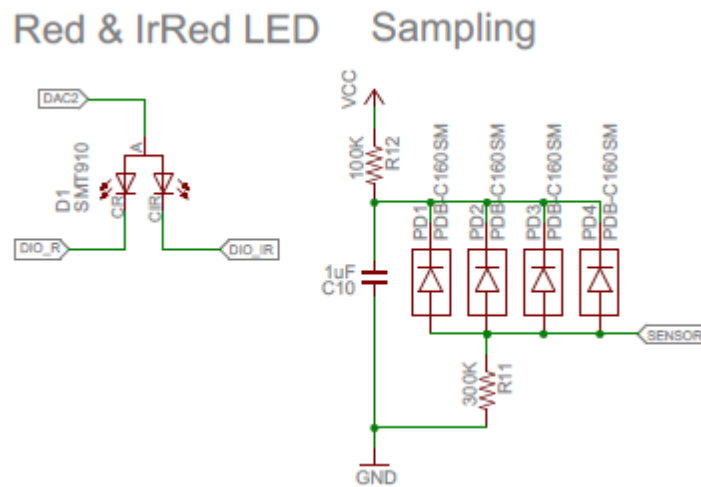


Figure 18. Improved red & near-infrared excitation LED module (version 2) schematic.

The excitation LED module of prototype version 2 is capable of automatic LED intensity control and uses a low-cost Marubeni SMT660/910 bi-color LED with the same typical forward current (20 mA) and forward voltages (1.9 V and 1.3 V for the 660 nm and 910 nm sources, respectively) as the API PDI-E837 dual excitation source used in version 1. The DAC output (0-2.4 V) of version 2 replaces the power supply connection of the excitation LED module, and the trim potentiometers are removed. Red or near-infrared channel selection is still implemented by two DIOs.

In the signal sampling module, the modified R11 and R12 ratio inhibits the signal amplitude sampled at the ‘SENSOR’ tagged wire. The maximum sampled voltage is limited to

$$SENSOR_{MAX} = VCC \cdot \frac{R11}{R11 + R12} \quad (3.1)$$

Device Prototypes

Figure 19 contains an upper view of both pulse oximeter prototypes (they share the same package and components). The PCB size is 41 mm by 36 mm excluding the antenna board. The top view shows the four main modules: microprocessor, sampling module, power management module, and display LED module. The primary differences can be better seen in the bottom view, as shown in Figure 20 and Figure 21. Version 2 features a more radial LED-detector arrangement and simplified but more controllable signal excitation circuitry.

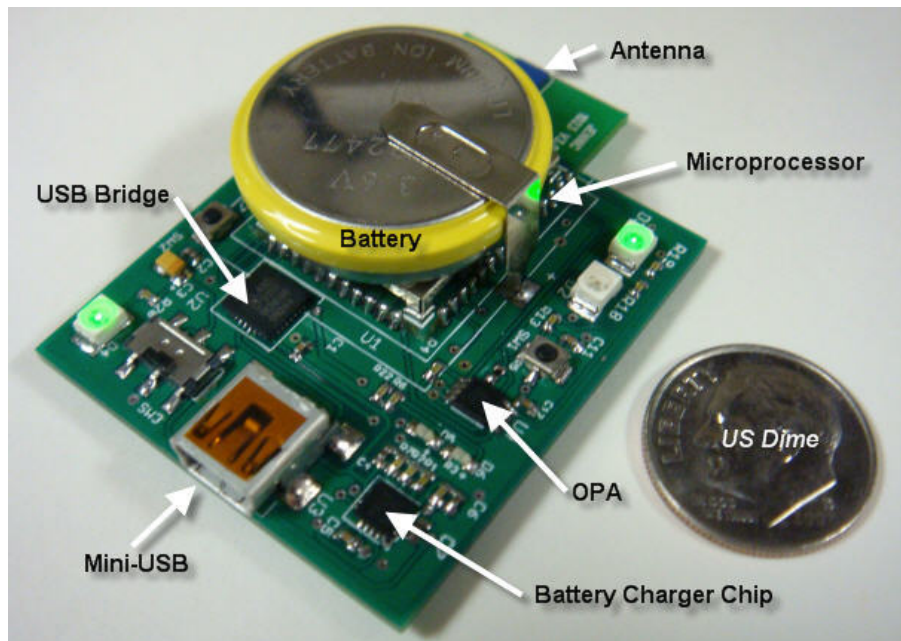


Figure 19. Top view of prototype version 1 and version 2.

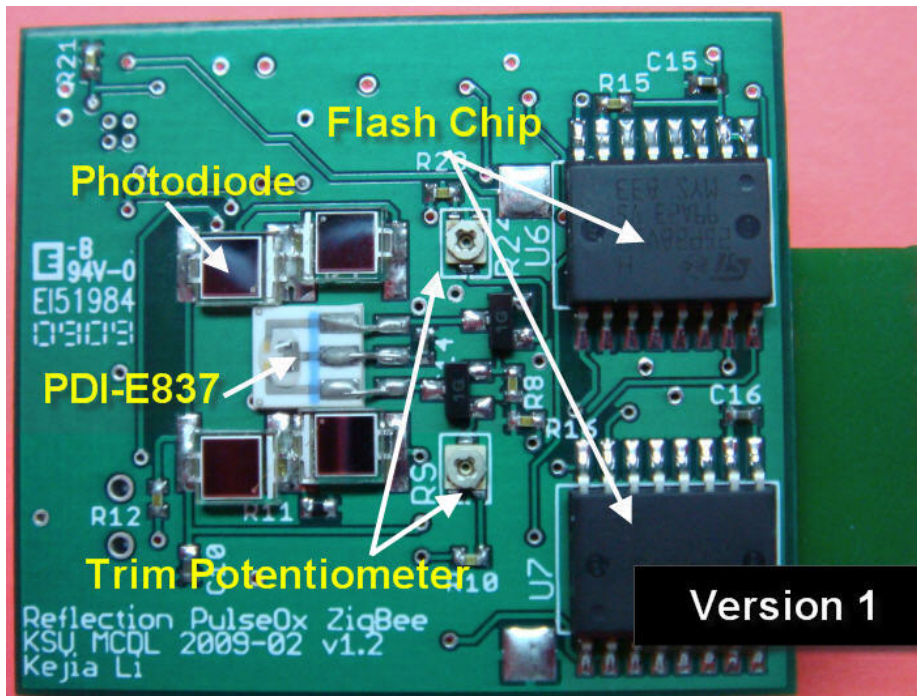


Figure 20. Bottom view of prototype version 1.

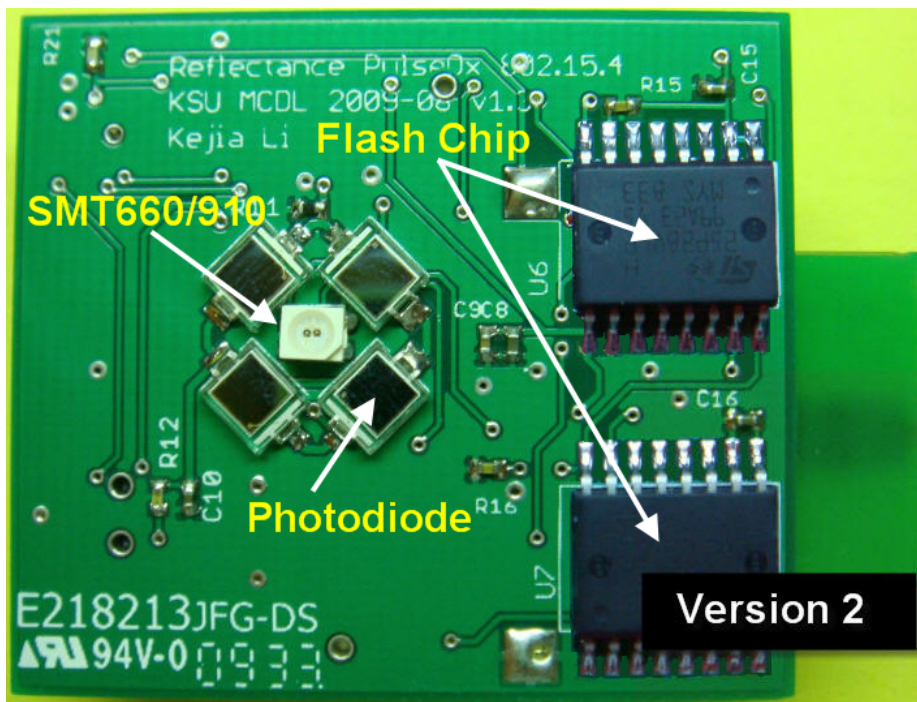


Figure 21. Bottom view of prototype version 2.

CHAPTER 4 - Firmware Development

The Jennic JN5139-EK020 Starter Kit not only contains Jennic wireless microcontroller products, but it also provides a firmware development environment for wireless network applications. Code programming was completed in this environment - Jennic CodeBlocks, which offers an abundant user guide, reference manual, and example code (available online).

Jenie Application Programming Interface

Jenic's proprietary Jenie software provides an easy to use interface to develop wireless network applications for Jennic JN5139 wireless microcontrollers. The Jenie Application Programming Interface (API) offers C functions to control the wireless network and the on-chip hardware peripherals, as outlined in Table 5 [43].

Table 5. Jenie API functionality (from [43]).

Management Tasks

- Configure and initialize network
- Start a device as a Coordinator, Router or End Device
- Determine whether a Router or Coordinator is accepting join requests
- Advertise local node services and seek remote node services
- Establish bindings between local and remote node services
- Handle stack management events

Data Transfer Tasks

- Send data to a remote node or broadcast data to all Router nodes
- Send data to a bound service on a remote node
- Handle stack data events

System Tasks

- Configure and start sleep mode
 - Configure, start and stop the radio transmitter
 - Obtain the version number of a component on the node
 - Handle hardware events
-

The powerful Jenie API tool was employed in the firmware development, and the general structure of the application code is illustrated in Figure 22.

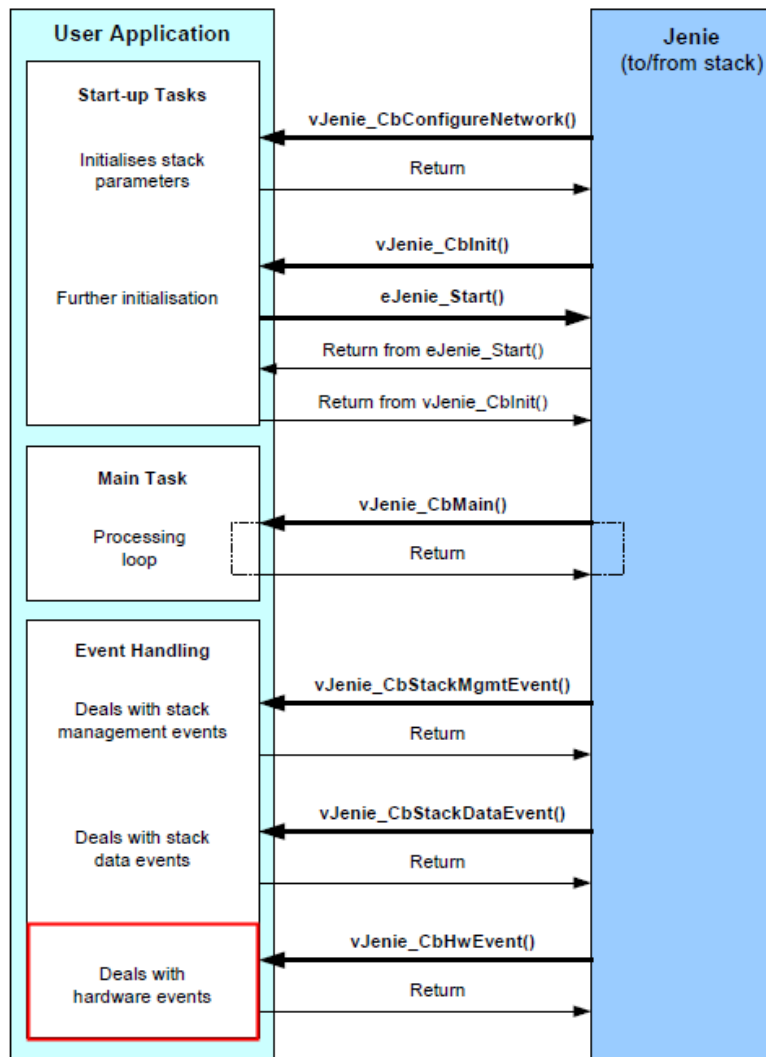


Figure 22. Jenie application code structure [44].

The stack-to-application functions and the application-to-stack functions presented in Figure 22 are all provided by the Jenie API, so these functions can be conveniently incorporated in the firmware code. The core part of the user application, “deals with hardware events” (marked with the red box in Figure 22), is also assisted by the Jenie Peripherals Interface (JPI), which includes analog resources (ADCs, DACs, comparators), digital I/O ports (DIOs), UARTs, timers, Serial Peripheral Interface (SPI) tools, etc.

Firmware Control Flow

The primary pulse oximeter hardware behavior is under the full control of the firmware code that corresponds to the red box section marked in Figure 22. The entire firmware control flow can be divided into ten steps, as illustrated in Figure 23, where each step is allotted a maximum time of $0.1T$ so that in aggregate the entire duration of the data cycle is $(0.1T)(10) = T$. At the current sample rate of 240 Hz per channel $T = 1/240$ sec = 4.16 ms. Each step is initiated by one timer-interrupt event. The step 10 “Reserved Slot” will be described in *Chapter 7-Feature Detection*. The pseudo-code for the control flow rolls over step by step and is described below.

```

While (Timer Interrupt)
{
    Check (Step)
    {
        Step = 1: Implement Code 1; Step = 2;
        Step = 2: Implement Code 2; Step = 3;
        Step = 3: Implement Code 3; Step = 4;

        .....

        Step =10: Implement Code 10; Step = 1;
    }
}

```

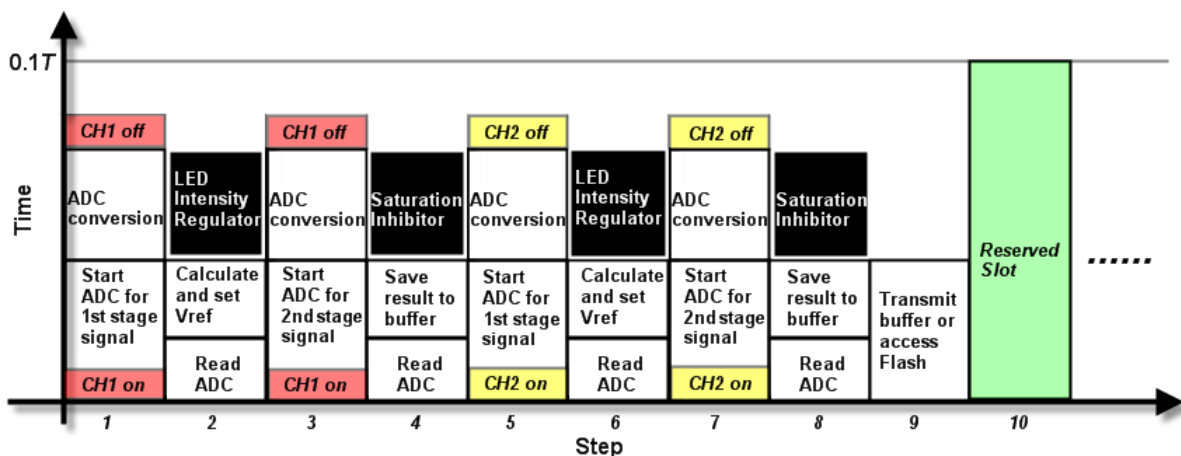


Figure 23. Ten-step firmware flow design for one data cycle of overall length T . CH1 and CH2 refer to the red and near-infrared channels, respectively. Note that the height of each block is not its actual implementation time.

Firmware Optimization

Although power consumption is constrained by the characteristics of the electronic components and signal sampling rate is restricted by the performance of the microprocessor, well-designed firmware code can efficiently switch electronic components on and off to lower the total power consumption and can allocate system resources, especially CPU time, in such a way as to maximize sampling frequency.

The wireless link requires the most power for the microprocessor module, with TX (transmitter) current at 38 mA and RX (receiver) current at 37 mA. The CPU consumes 7.75 mA at full speed, and the current required by the peripherals (ADC, DAC, UART, Timer, etc.) is less than 1 mA. JN5139 sleep current (with an active sleep timer) is only 2.6 μ A. Hence, a discrete wireless communication policy and an auto-sleep policy should be taken into consideration.

According to the power consumption data determined for all of the onboard parts (e.g., 20 mA for the excitation LED, 38 mA for the wireless transmitter, and 20 mA for the flash memory) excitation LED illumination and wireless communication (or flash memory access) constitute the majority of the total power cost. If the excitation LED and wireless functions are a continuous cost, the battery can support about 3 hours of operation. However, the firmware depicted in Figure 23 can be optimized to control and modulate their behavior appropriately so as to minimize the average current consumption.

To that end, excitation LED channels are turned off when the signal acquisition process is inactive. The only scenario that requires a channel to be turned on is when the ADC is prepared to work; however, the process of turning on a channel excitation LED is a step response, so the procedure to start the ADC must hold until the channel is stable. The duration over which the excitation LED channels are turned on can be minimized subject to this constraint. In this case, the average current consumption of the excitation LED is ensured to be less than 8 mA. Similarly, since only one of the ten steps (step 9) utilizes wireless communication, the average current consumption of the wireless link is ensured to be less than 3.8 mA. An overall current consumption less than 12 mA is therefore achieved compared to the original 58 mA, yielding more than 10 hours of operation on a single battery charge even when the unit is “continuously” acquiring and transmitting data.

The sampling interval T , which is the time duration to yield one data point pair for the two channels of photoplethysmographic data, is inversely proportional to sampling frequency:

$T = \frac{1}{f_s}$. The period of the timer on the microprocessor is set to $0.1T$, which results in ten interrupts (steps) being generated for each data cycle, and the implementation time of each step (or “height” of each step in Figure 23) should be ensured to be less than $0.1T$. If an increase in sampling frequency is required to prevent aliasing, e.g., caused by ambient noise, the following method can be adopted. First, given the same timer period, $0.1T$, reduce the number of steps to n (< 10) to achieve

$$f_s' = f_s \cdot \frac{10}{n} \quad (4.1)$$

Next, using n steps, lower the upper bound $0.1T$ to correspond to the “highest” block for the set of steps (see Figure 23). The blocks can also be rearranged to lower the highest block. A realistic application would be to double sampling frequency when only one channel is utilized. A four-step version of the firmware with the same T has been developed successfully using a similar approach, where $f_s' = 2.5f_s$ according to Equations 4.1.

CHAPTER 5 - MATLAB Interface

All red and near-infrared signal data yielded by this pulse oximeter will either be stored on the unit or transmitted in real-time to a PC via a wireless ZigBee or wired USB link mapped to a serial port. Any stored onboard data will also be eventually transmitted to a PC for backup, display, signal processing, etc. Wireless communication still requires a receiver on the PC side, which talks to the PC through a serial port. Hence, serial communication is the key to pulse oximeter data transfer.

MATLAB was adopted as the client tool on the PC to receive, process, display, and save the data provided by the device. MATLAB Graphical User Interfaces (GUIs) can be developed for different applications, including firmware debugging, signal demonstrations, laboratory class tools, and research-oriented tools. Code creation and graphic design are therefore two aspects of MATLAB interface development; this chapter will elaborate on both aspects.

Serial Communication

The CP2102 USB-to-UART bridge chip soldered on the unit performs the signal transformation from the UART to the USB specification. Therefore, RS-232 (Recommended Standard 232 [45]) is the standard actually employed for data communication. RS-232 is defined as a “standard for serial binary single-ended data and control signals connecting between a DTE (Data Terminal Equipment) and a DCE (Data Circuit-terminating Equipment), which is commonly used in computer serial ports.” [45].

Once a data frame is created by a pulse oximeter unit, it will be eventually transmitted to the PC client via a serial port. Figure 24 illustrates the content included in each data frame. One single frame consists of 18 bytes. The first 8 bytes are assigned to the unique 64-bit MAC address of a specific pulse oximeter, which becomes especially important to classify data sources when multiple devices communicate with the same PC client. Additionally, the MAC address is also identified by the PC client to signify the beginning of the four channels of signal data.

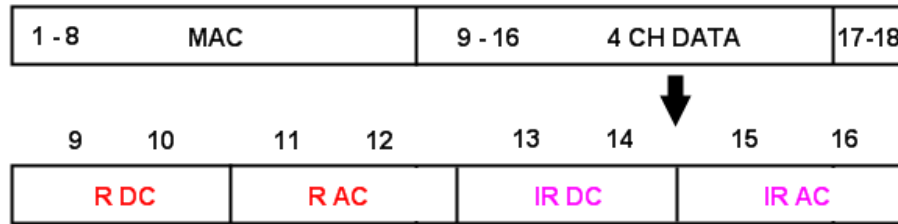


Figure 24. Serial communication data frame structure. R: red channel; IR: near-infrared channel. Numbers are in bytes, with 18 bytes total. The first 8 bytes are assigned to the unique MAC address, the next 8 bytes are assigned to the four channels of signal data, and the last two bytes are appended to ensure the frame integrity.

The next 8 bytes are assigned to the four channels of signal data: the DC value of the red channel, the AC value of the red channel, the DC value of the near-infrared channel, and the AC value of the near-infrared channel, in that order. Each signal sample is two bytes, with the most significant byte coming first.

The last two bytes have nothing to do with the signal information but play an important role in the integrity of the frames. In a high-speed serial communication link with a baud rate of 115200 bps, it is observed that the last one or two bytes are often lost regardless of the frame length. Hence, byte 17 and byte 18 have to be appended to each frame. Since the length of each frame is not fixed (i.e., it might be 16, 17, or 18 bytes), the frame determination process therefore relies on the unique MAC address at the very beginning rather than the frame length. Additionally, the frame structure varies for differing applications, e.g., decision information may also be attached.

MATLAB provides a useful function `serial()` to deal with serial communication. This function constructs a serial port object, which has many configurable and readable properties (see Table 6). Some important properties include “Port” and “Baud Rate,” which are the fundamental parameters to initialize serial communication. “InputBufferSize” specifies the buffer size for incoming data temporary storage, and the actual space occupied is recorded by “BytesAvailable.”

Table 6. Properties of an object created by the MATLAB serial() function.

○ BaudRate	○ ByteOrder
○ BreakInterruptFcn	○ BytesAvailable
○ DataBits	○ BytesAvailableFcn
○ DataTerminalReady	○ ErrorFcn
○ FlowControl	○ InputBufferSize
○ Parity	○ Name
○ PinStatusFcn	○ OutputBufferSize
○ Port	○ OutputEmptyFcn
○ ReadAsyncMode	○ RecordDetail
○ RequestToSend	○ RecordMode
○ StopBits	○ RecordName
○ Terminator	○ Tag
○ Timeout

MATLAB Code

MATLAB code runs behind the graphical interface. This code consists of functions that respond to the interface events, e.g., start interface, click a button, and input text. The core code that runs with the highest priority is the serial communication processing routine. Once data frames are detected in the serial input buffer, the four channels of signal data should be immediately extracted into the MATLAB workspace to ensure real-time data acquisition. The data in the workspace can then be further processed, e.g., visualized or filtered. The pseudo-code for serial communication processing is described below.

```

While (Read BytesAvailable)
{
  If (BytesAvailable > A specified number)
  {
    X = Serial buffer;
    Empty Serial buffer;
    For (i = 1 to BytesAvailable)
    {
      If (X(i) == MAC(1))
      {
        If (X(i+1) == MAC(2))
        {
          If (X(i+2) == MAC(3))
          {
            Extract MAC address;
            Extract signal data;
          }
        }
      }
    }
  }
}

```

The “A specified number” value is determined by how much delay is tolerable for an interface update. For example, if “180” is specified as the threshold, around 10 frames of delay will be induced because each frame consists of 16-18 bytes. If the sampling frequency of the pulse oximeter is 100 Hz, there is only a 0.1 second lag. A threshold number that is too small (e.g., 18) is not recommended, as it keeps the interface locked into the serial communication loop and slows down the response to other interface functions.

Although a MAC address is a unique identification number, the first three bytes are the same for all JN5139 modules, so MAC(1:3) is checked as a start of a data frame. Their values (0, 21, and 141) also help to ensure that the serial communication interface will not be fooled by the four channels of signal data, the most significant byte of which is always less than 8. The full unique MAC address and four channels of signal data can then be extracted after the frame header is confirmed.

MATLAB Graphical User Interface 1

GUIDE, the Graphical User Interface Development Environment, is the tool provided by MATLAB to create GUIs. Using the GUIDE Layout Editor, a GUI can be populated by clicking and dragging GUI components, such as axes, panels, buttons, text fields, sliders, and so on, into the layout area. Menus and context menus can also be created for the GUI. The activities and event responses that correspond to these components are completed in MATLAB code.

The first MATLAB GUI was initially developed for firmware debugging and signal visualization, but by adding a signal processing module into the original interface (see Figure 25), it became a good tool for a Fall 2009 biomedical instrumentation laboratory [14]. The signal processing module includes (1) pulsatile signal compensation (to recover the adjusted data points, i.e., discrete jumps in Figure 6, in the raw photoplethysmographic signals induced by the shift-resistant method), (2) a frequency spectrum display, (3) real-time noise filtering, (4) real-time SpO_2 tracking, and (5) customized function integration.

Besides performing signal processing, this GUI also makes it convenient to set the communication parameters, to visualize the photoplethysmographic signals in real-time, to log raw data to files, etc. The left side of this GUI is the control panel, and the right side is the data visualization area. The GUI's primary operations and functionality are selectively listed in Table 7.

Table 7. MATLAB interface 1 control panel functionality.

Name	Function
○ Sample Rate	Specify f_s (up to 480 Hz)
○ Wireless Ch	Specify the wireless communication channel when multiple units are present
○ Signal Processing	Compensation, Fast Fourier Transform, filtering, SpO_2 , and user-defined function
○ Filter Option	Set filter type and cut-off frequency
○ SpO_2 (%) =	Specify calibration curve coefficients
○ Data Dump	Dump the data received to a file

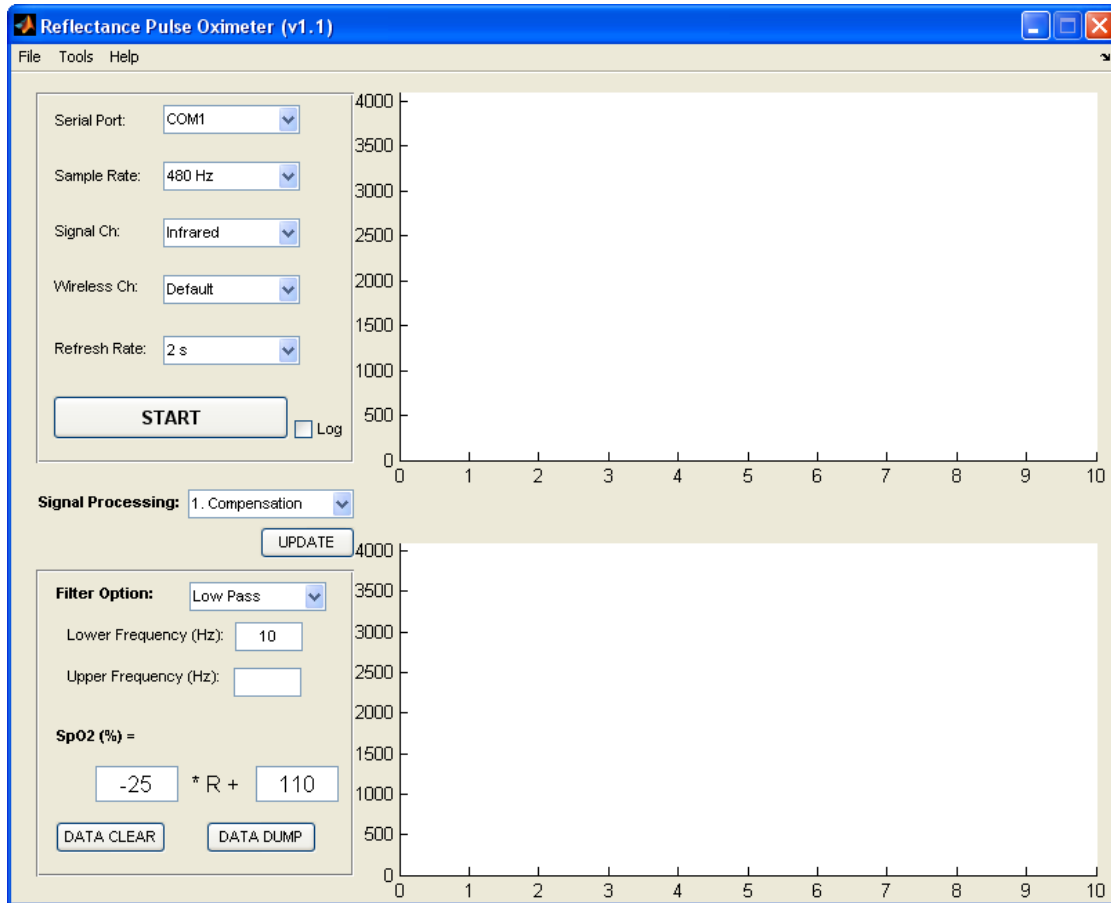


Figure 25. Pulse Oximeter MATLAB GUI 1 that contains a signal processing module.

MATLAB Graphical User Interface 2

Figure 26 illustrates the second MATLAB GUI developed as a feature detection tool. No algorithms or signal processing are implemented on this interface. It only displays signals, signal features, decision results (these relate to data viability – see *Chapter 7*), and HR and SpO_2 values transmitted by a pulse oximeter device. The main motivation to develop this GUI was to manually verify the decision results and seek appropriate thresholds for each decision. More details as to the decisions reached by a feature detection scheme are presented in *Chapter 7*.

Interface 2 also integrates the control panel for communication parameter setting and raw data storage. The two small plots (Figure 26, lower left) show four features alternating at a three-second interval. The big plot on the upper right depicts the original photoplethysmographic signal, and the big plot on the lower right depicts the minimum representation for the signal: the

least number of points to represent the primary features in the original pulsatile waveform. There is also a purple information bar in the middle of the interface to show the decision results, e.g., “Severe Motion Detected,” “Valid Pulse,” and “Signal Saturated.”

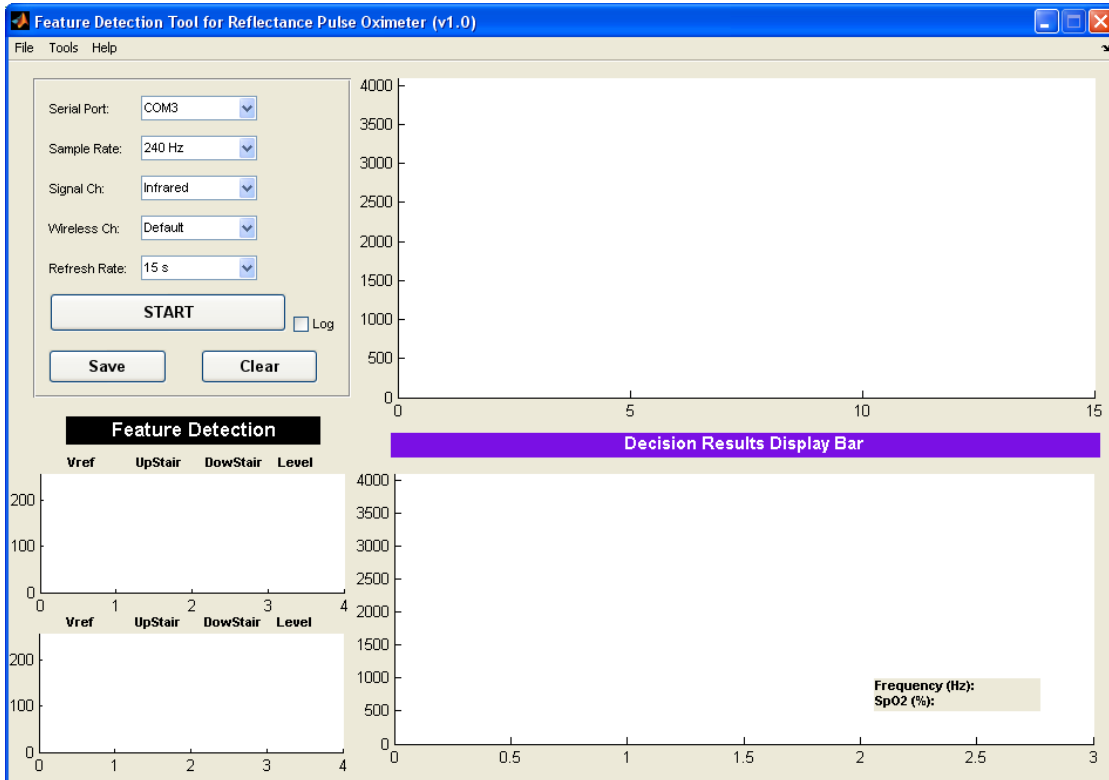


Figure 26. MATLAB GUI 2 developed for a feature detection tool.

CHAPTER 6 - Multiple Applications

This chapter focuses on the applications of the new device and the data acquired, processed, and displayed via the developed MATLAB interface. Since a pulse oximeter is conventionally designed for HR and SpO_2 monitoring, blood oxygen saturation calibration naturally becomes the first task to accomplish. The pulse oximeter works in reflectance mode, so multi-location measurement results are demonstrated, discussed and compared. It also serves as an excellent learning and laboratory tool for both undergraduate and graduate students that may gain benefit from the signals and the circuitry. Finally, given the unique data provided by this novel high-fidelity pulse oximeter, more applications and research potential are presented.

Blood Oxygen Saturation Calibration

A total of 22 photoplethysmographic data sets were collected from 22 subjects (ages 20-64) for blood oxygen saturation calibration: determination of the best fit linear regression line for 'known' SpO_2 values as a function of the correlation coefficient, R , calculated from the PPG data. In this application, MATLAB interface 1 was adopted to perform data acquisition and blood oxygen saturation calculation tasks.

Figure 27 illustrates an example data sequence obtained by this GUI, where the unique 64-bit client ID (MAC address) is noted on the title bar. The upper axes (x: time, y: digitization level) show the real-time raw photoplethysmographic signal and the baseline of the near-infrared channel, the duration of which is set by the control panel ("Refresh Rate"). On the control panel, the "Serial Port" is COM 2, the "Sampling Rate" is 100 Hz, and the "Signal Channel" is near-infrared. The lower axes show the real-time calibration ratio, R , for the blood oxygen saturation level, SpO_2 , using the Fourier transform method [46]. R updates every 0.5 seconds using the past 4 seconds of photoplethysmographic data. The final SpO_2 value is achieved by employing a median or mean filter on the 40 points of R data and plugging the resulting value into a specified linear calibration curve.

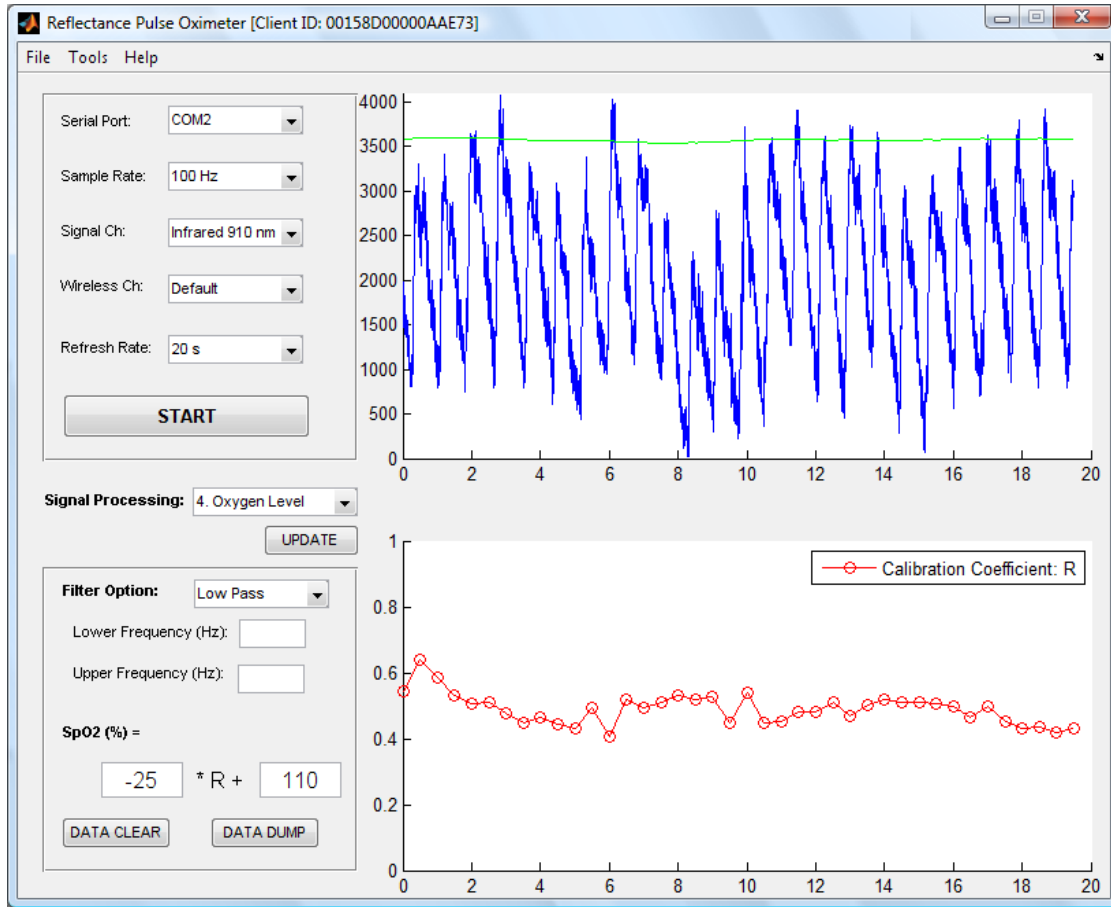


Figure 27. MATLAB GUI 1 adopted for blood oxygen saturation calculations. In this example, a series of calibration ratios is extracted from the current data segment.

Blood oxygen saturation levels read from a BCI[®] 3180 pulse oximeter and plotted in Figure 28 against the calibration ratios calculated by the pulse oximeter. The linear calibration curve derived from this data set is

$$SpO_2(\%) = -23.7R + 109.2 \quad (6.1)$$

with a correlation coefficient $r^2 = 0.795$ and a standard deviation $s = 0.48$. More accurate and reliable calibration results can be achieved by acquiring more measurements over a larger SpO_2 range and by employing higher-accuracy devices like blood gas analyzers and CO-oximeters [47].

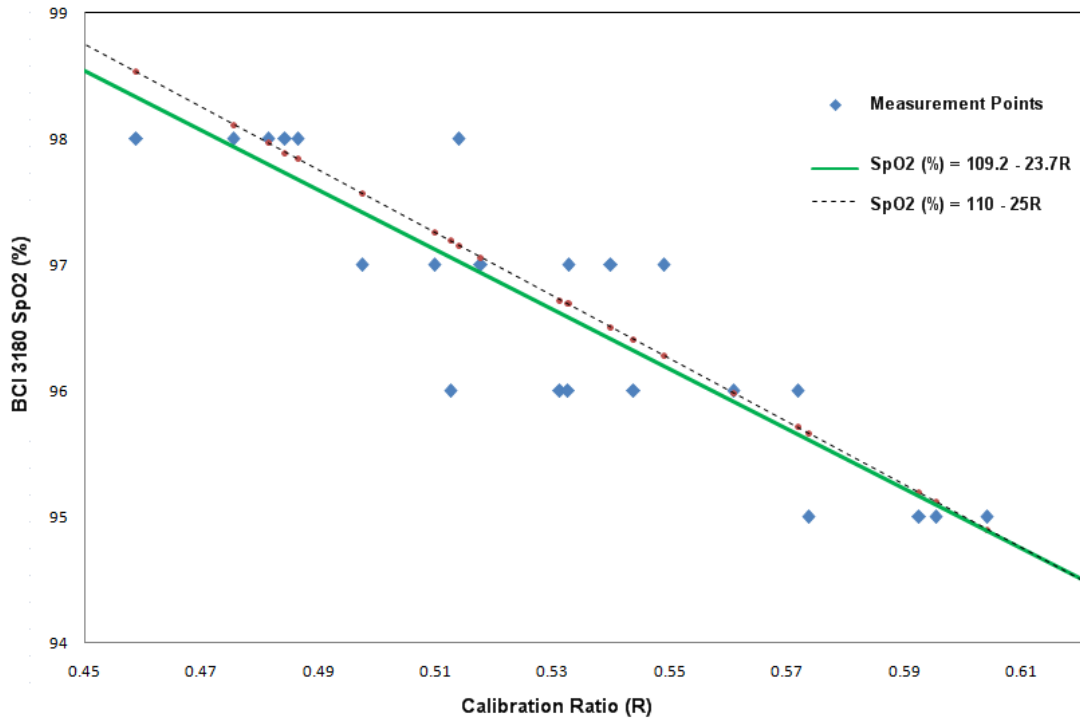


Figure 28. Blood oxygen levels read from a BCI⁰ 3180 pulse oximeter plotted against the R values calculated by the pulse oximeter prototype. The linear regression line (solid line) from the least-squares fit is expressed as $SpO_2 (\%) = 109.2 - 23.7R$ in comparison with the published calibration line (dashed line) $SpO_2 (\%) = 110 - 25R$.

Multi-Location Measurements and Discussion

The pulse oximeter prototypes have been tested for several months, yielding hundreds of high-quality photoplethysmographic records from different people. Many of these data sets were gathered during the Spring 2010 KSU Engineering Open House (under IRB approval #5448) and the Fall 2009 Bioinstrumentation Laboratory, where the pulse oximeter exhibited its reliability and convenience for photoplethysmographic signal acquisition. In one case, a young woman presented a large peak-to-valley signal with a small portion saturated (acquired by prototype version 1), which could have been addressed by trimming down the LED intensity (this was solved in prototype version 2 with adaptive LED intensity control). In another case, an old man presented a very small AC signal. The reason is assumed to be poor perfusion in his fingertip. In

such a case, one can take the advantage of the reflectance pulse oximeter design by measuring their SpO_2 levels at their temple or other accessible location.

Experimental results demonstrated on the following pages were acquired in an indoor environment utilizing prototype version 2 with a sampling frequency of 240 Hz. The results can be placed into two categories according to measurement site: (1) conventional location (fingertip) and (2) other location (wrist, earlobe, temple, etc.).

First, Figure 29 illustrates 25 seconds of experimental fingertip data extracted from a 100-second segment of consecutive measurements. Both channels of photoplethysmographic data, red and near-infrared, are uncompensated for a display area with limited height. The AC values of the near-infrared channel (Figure 29 (a)) offer 1.2 V peak-to-valley (i.e., 2048 digitization levels), and the AC values of the red channel (Figure 29 (b)) offer fewer digitization levels: about half compared to the near-infrared channel.

Even without applying any analog or digital filters, the signal quality is still quite good for both channels. As shown in Figure 30, up to seven harmonics reside in the spectrum of the near-infrared data, whereas six harmonics reside in the spectrum of the red-channel data. Additionally, the photoplethysmographic information and the noise components (e.g., 60 Hz and 120 Hz electrical grid noise) are clearly separated in the frequency domain. To further refine the signal, a properly designed digital low-pass filter can be applied.

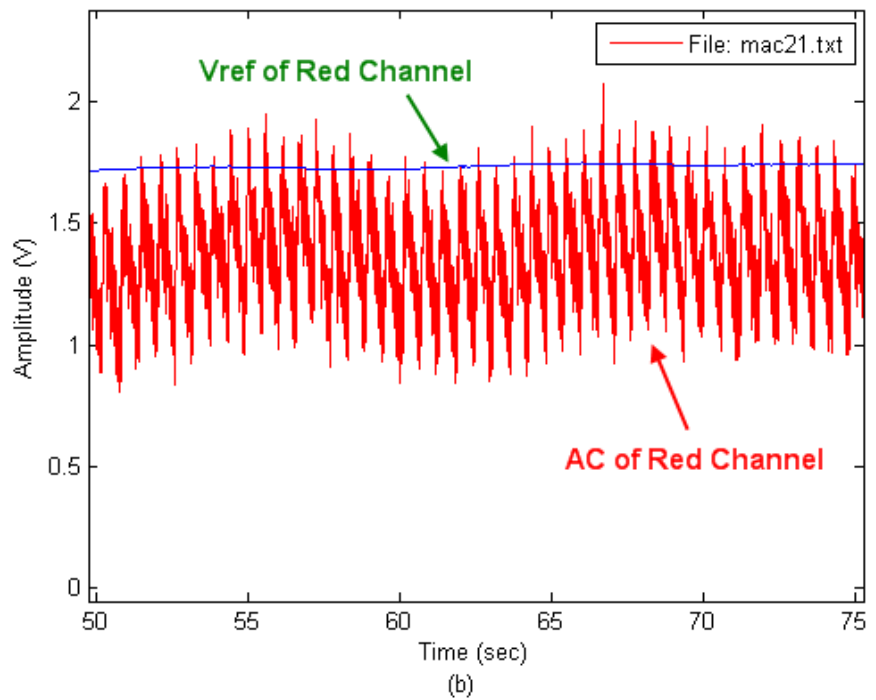
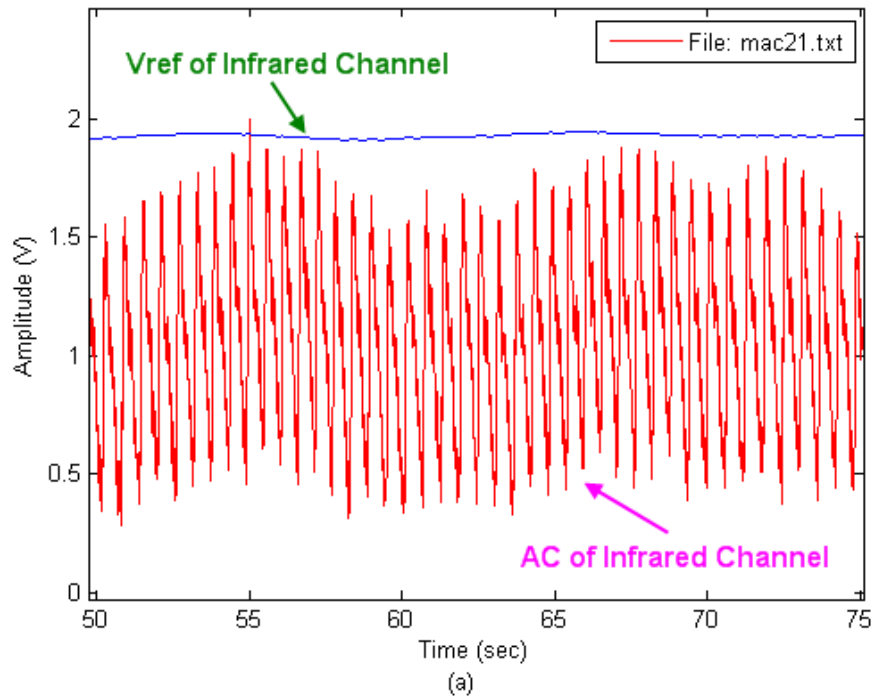


Figure 29. Fingertip measurement site results: 25 seconds of time-domain PPG data from the (a) red and (b) near-infrared channels.

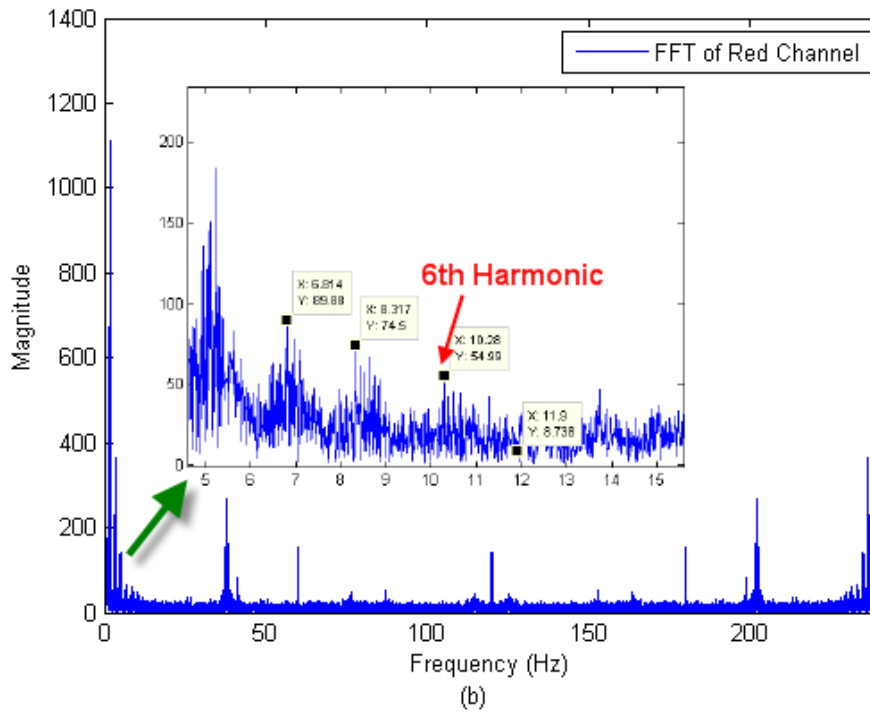
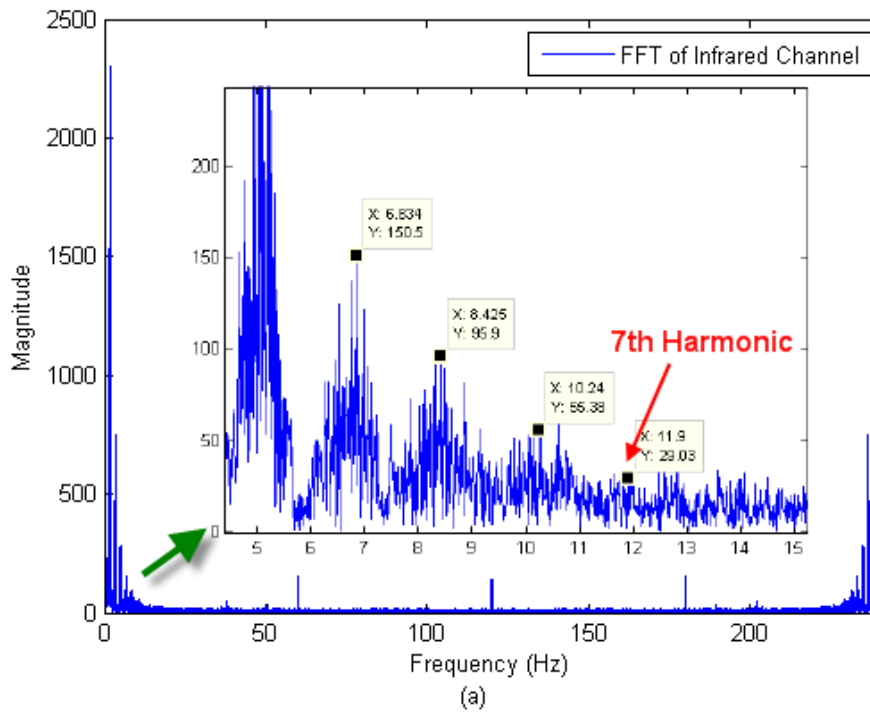


Figure 30. Fingertip measurement site results: frequency-domain spectra of 100 seconds of PPG data from the red (a) and near-infrared (b) channels.

Figure 31 demonstrates a zoomed-in section of the same experimental data set, where the raw signal is accompanied by its real-time filtered form within a MATLAB GUI. The filter is a 200-order low pass filter with a cut-off frequency equal to 10 Hz and is realized by the MATLAB function $firls()$, which is a linear-phase FIR filter design using least-squares error minimization. This filter has a delay of $t_d = 0.414$ seconds specified by

$$t_d = (n-1)/2f_s \quad (6.2)$$

where $n = 200$ and $f_s = 240$ Hz. The filter exhibits no phase distortion and has very slight magnitude ripple in the pass band, as shown in Figure 32. This ripple can be further reduced by increasing n .

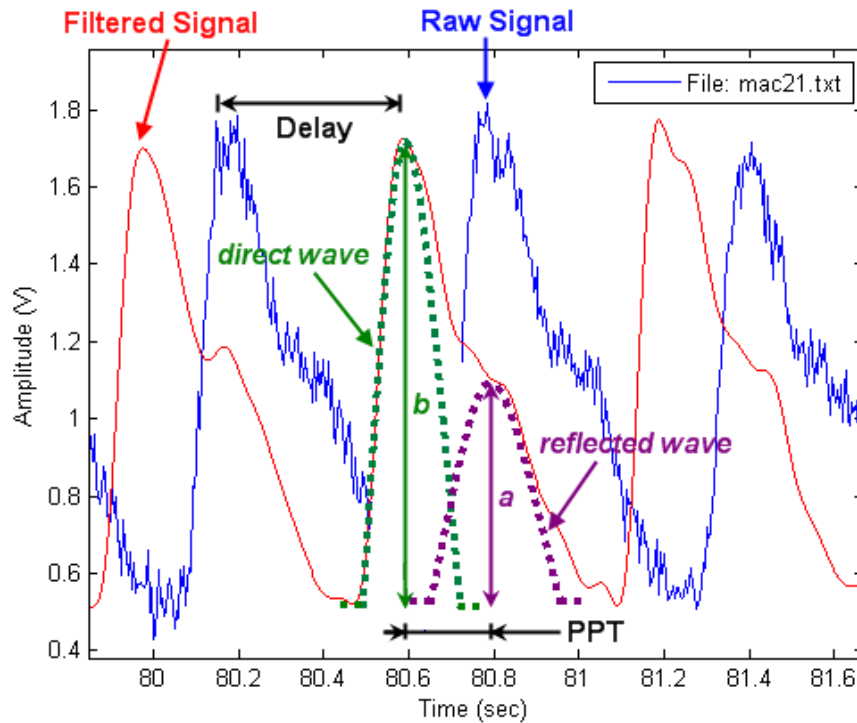


Figure 31. Fingertip signal processing and digital volume pulse (DVP) analysis.

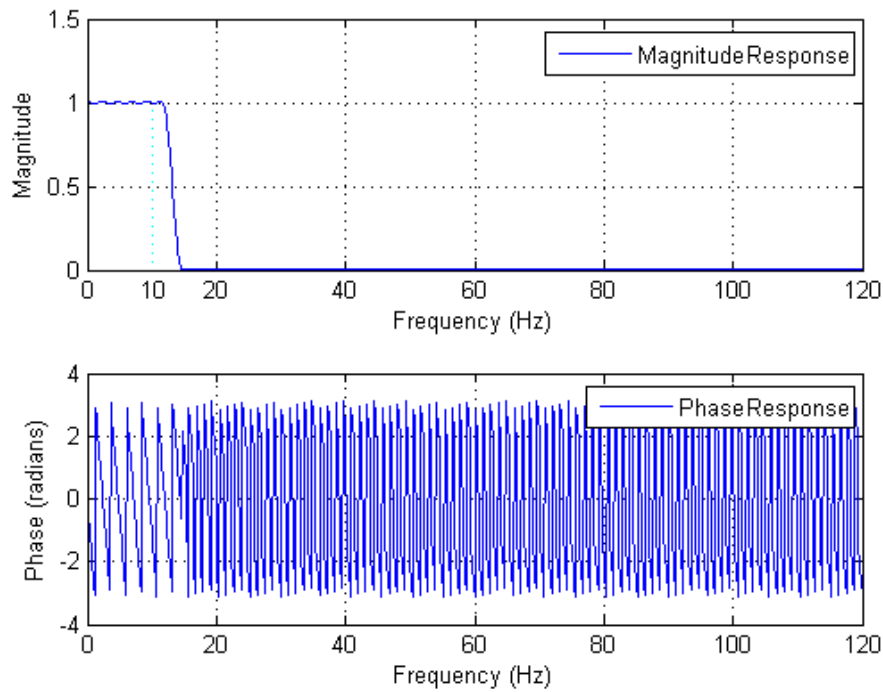


Figure 32. Magnitude and phase response of the 200-order low-pass FIR filter.

Given the high-fidelity digital volume pulse (DVP), some important cardiovascular parameters can be accurately extracted [12, 13, 48]. For example, the peak-to-peak time (PPT), as marked in Figure 31, can be used to calculate pulse wave velocity, which correlates to arterial stiffness, and “a” and “b” are used to calculate the reflectance index RI (see Equation 1.2), which correlates to endothelial function.

Figure 33 shows experimental data sets from the wrist at three placement locations (Figure 34). The signal quality, e.g., SNR, in location 2 is obviously lower relative to locations 1 and 3, but all three are high-fidelity photoplethysmographic signals. At present, it is difficult to obtain high quality photoplethysmographic data at the wrist; that often requires the application of pressure to bring the optical sensor closer to the major arteries [46]. An operation to achieve the same effect, bending the hand about 45 degrees, was usually employed if the presenting photoplethysmographic signal had a low SNR. Additionally, since every person has different arterial locations and depths at the wrist, proper measurement sites are essential to acquire high quality data sets, which was also verified in [49].

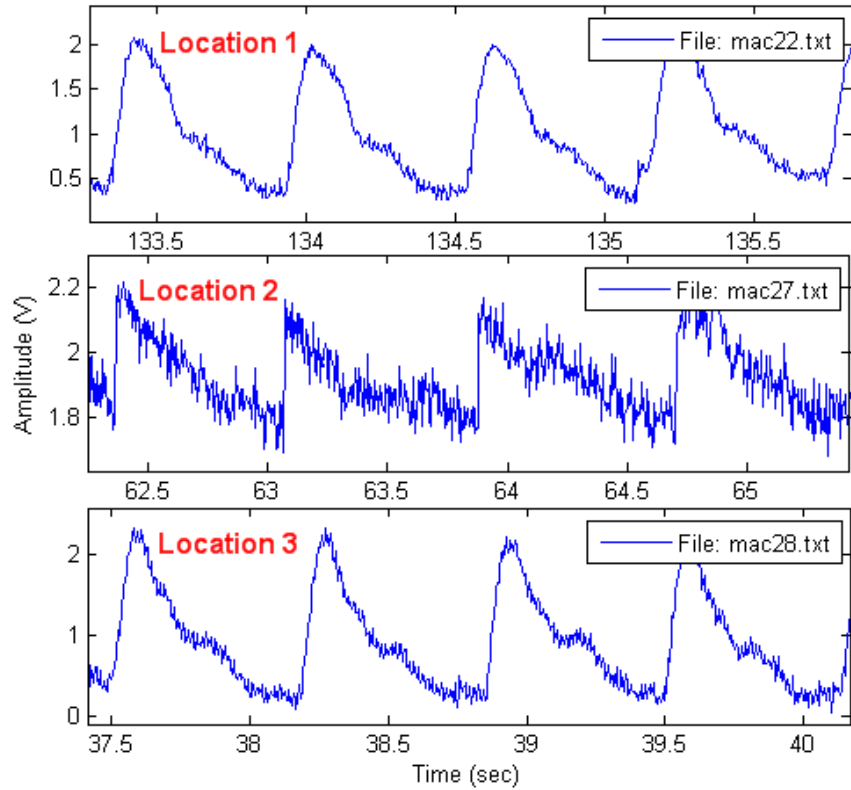


Figure 33. Wrist measurement site results. The pulsatile curves correspond to different placement locations.

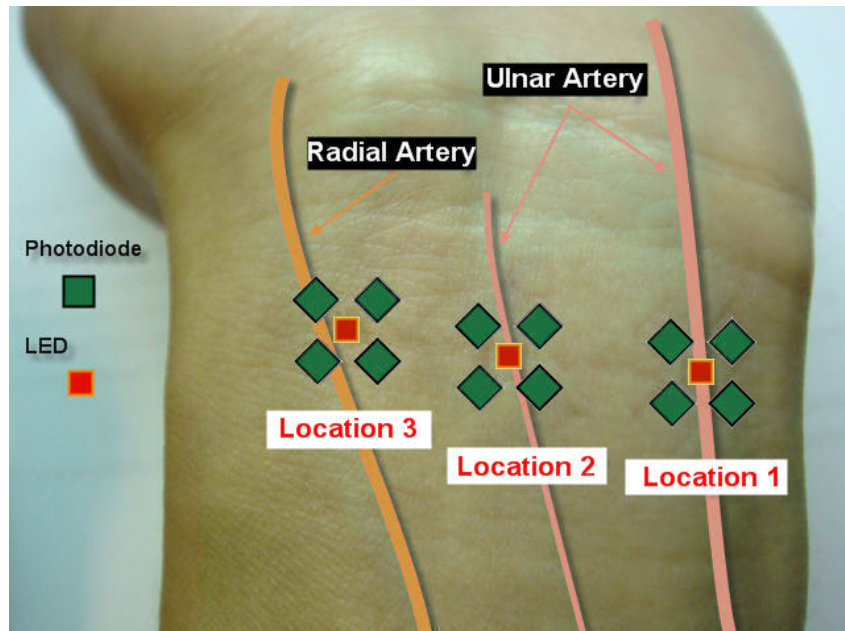


Figure 34. Pulse oximeter measurement locations on the left wrist.

Figure 35 shows two channels of earlobe experimental data. The near-infrared channel has an $SNR = 5.7$ and a peak-to-valley voltage of 1.0 V; the red channel has a much lower $SNR = 1.8$ and a peak-to-valley voltage of 0.6 V. Although two channels of data are required to calculate the oxygen saturation level and a large portion of the noise is removable, the near-infrared channel data are always preferred for pulse wave analysis and display purposes.

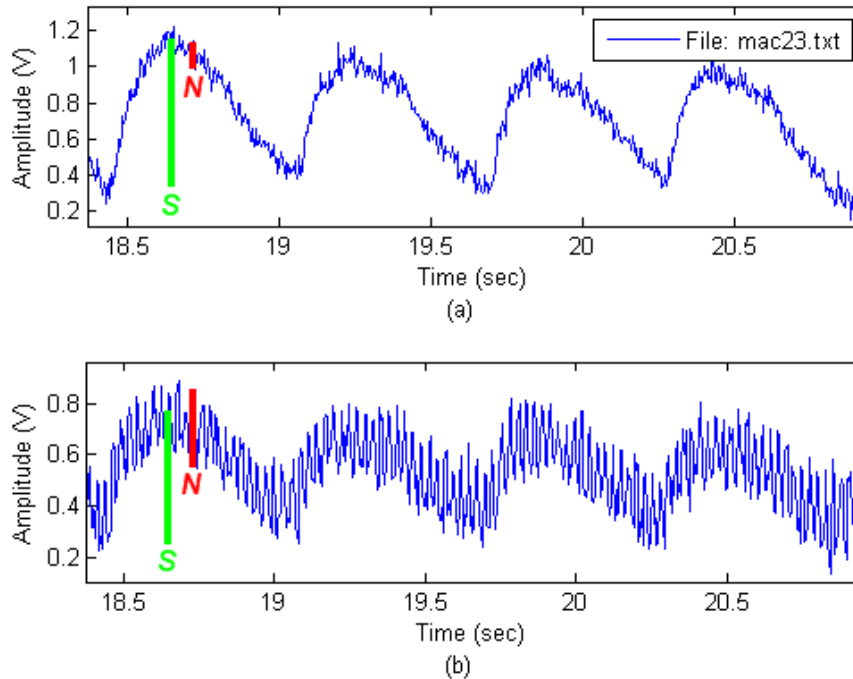


Figure 35. Earlobe measurement site results: (a) near-infrared channel and (b) red channel.

Figure 36 illustrates 120 seconds of temple experimental data that include respiration activity and a swallow motion in the middle. There are 33 respiration cycles present during the 120-second recording time (i.e., respiration rate is 0.275 Hz). An FFT is applied to seek the likelihood of extracting respiratory information from the photoplethysmographic data. In the frequency spectrum (Figure 36 (b)), 1.679 Hz is believed to be the heart rate and the 0.266 Hz frequency component is likely the respiratory frequency. This is only an initial result but is a good example of a situation where the high-fidelity pulse oximeter is capable of retaining the motion information.

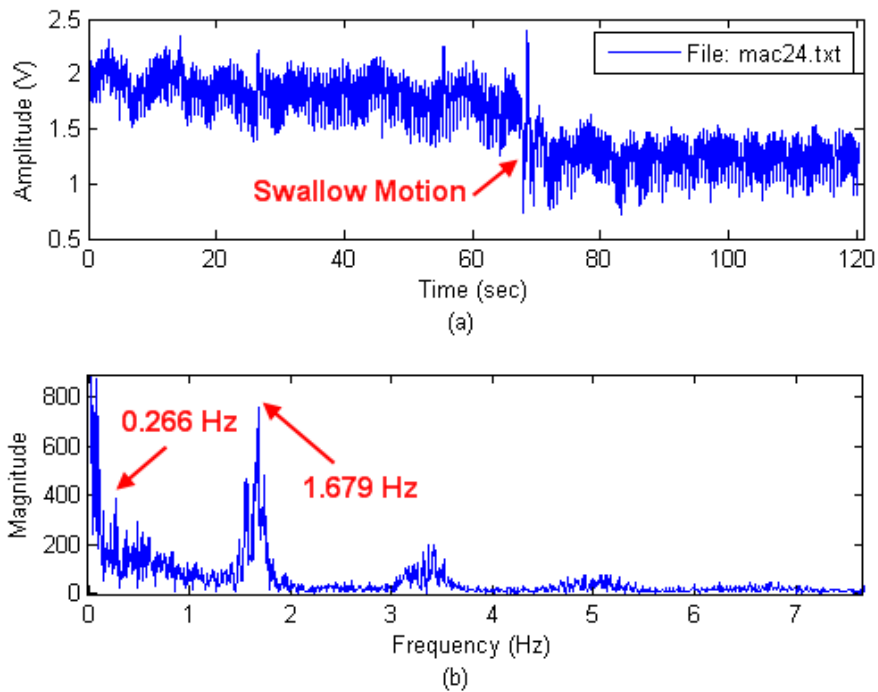


Figure 36. Temple measurement data: (a) time-domain PPG with respiration and motion information and (b) frequency-domain spectrum.

Biomedical Instrumentation Laboratory

The new pulse oximeter design and its accompanying MATLAB interface were initially applied within the context of the Fall 2009 Biomedical Instrumentation course jointly taught by faculty in the KSU Department of Electrical & Computer Engineering (College of Engineering) and the KSU Department of Anatomy & Physiology (College of Veterinary Medicine). An ASEE (American Society for Engineering Education) paper on this subject has been accepted, and part of the work is presented here [14].

Ten undergraduate and graduate students were enrolled in this course. Ten sets of devices were manufactured, programmed, and tested, as in Figure 37. The instructors let the students work in pairs (five groups of two students). A commercial pulse oximeter (Smiths Medical BCI[®] 3180) was also employed as a comparison standard for the blood oxygen saturation values calculated by the custom system.

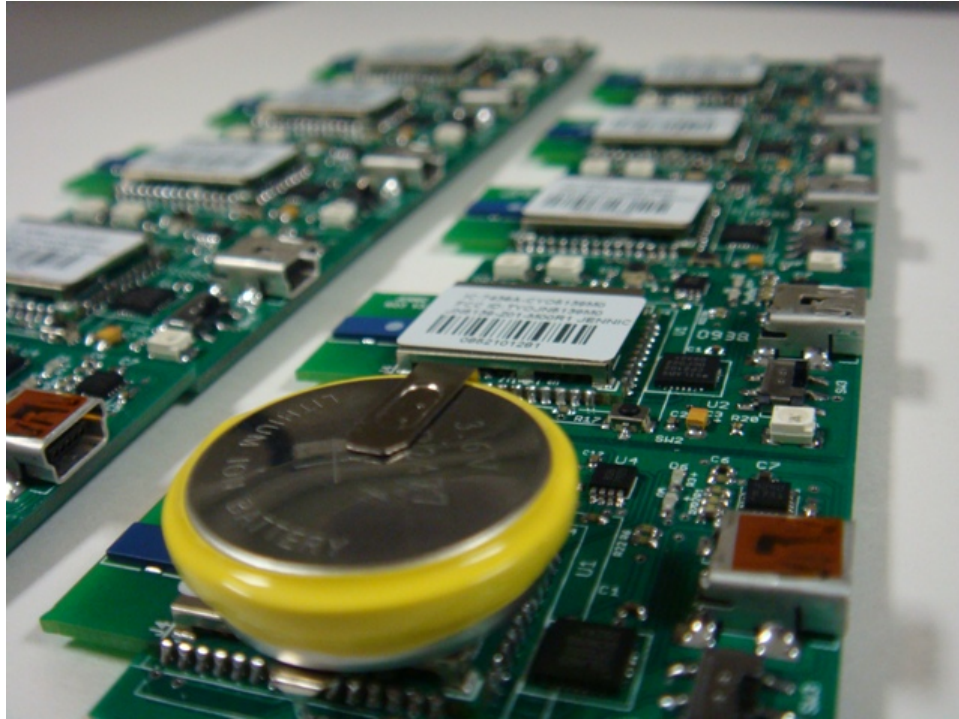


Figure 37. Ten pulse oximeters to be used in a Fall 2009 biomedical instrumentation laboratory.

The new pulse oximeter design exceeded expectations in this initial laboratory experience. Due to the adaptive-LED-intensity mechanism that seeks to optimize signal quality independent of a subject's relative perfusion, all ten students acquired high-quality photoplethysmographic data and derived meaningful analysis results, which has not always been the case with previous pulse oximeter designs [36, 50]. Figure 38 shows a team of students acquiring fingertip data with a goal to identify the ambient noise component. By applying an FFT operation to the current data segment, they found a 120 Hz spike in the frequency domain, where the spike is caused by 120 Hz flicker from the full-wave-rectified fluorescent room lights. Figure 39 illustrates the use of the BCI[®] 3180 pulse oximeter (left) and temple-based measurements for the determination of respiration rate (right).



Figure 38. A team of students acquiring PPG data from the fingertip and performing ambient noise analysis with the new pulse oximeter and MATLAB interface.

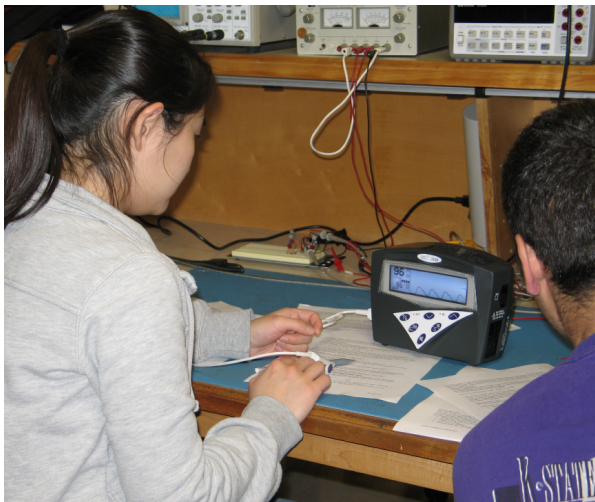


Figure 39. Blood oxygen saturation determination using the BCI[®] 3180 pulse oximeter (left) and photoplethysmogram measurement on the temple to assess respiration rate (right).

Other Applications

The potential application areas that can be addressed with the novel high-fidelity reflectance wireless pulse oximeter are more numerous than those mentioned in this chapter. Each clinical parameter listed in Table 1 can be further investigated using this device. Due to its unique and improved characteristics as outlined in Table 2 and its corresponding convenient and efficient MATLAB interfaces, the new pulse oximeter can potentially offer more reliable measurement results and therefore more promising outcomes.

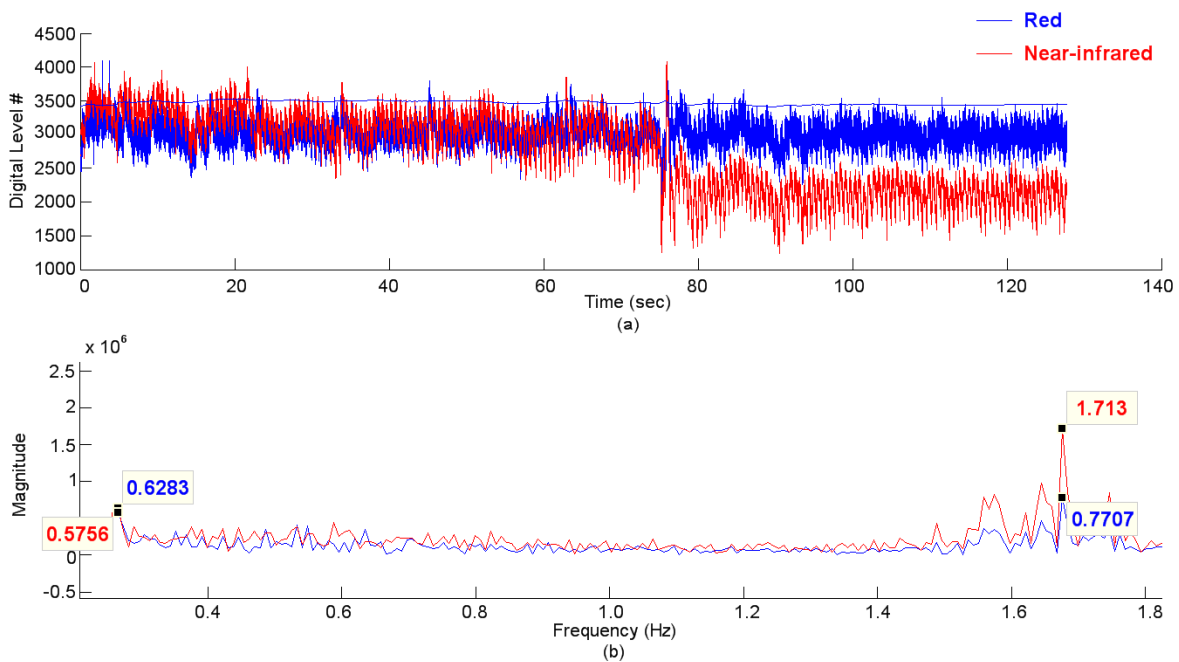


Figure 40. Tentative estimation of venous blood oxygen saturation level: (a) time-domain signal and (b) frequency spectrum.

Figure 40 gives an example of a tentative venous blood oxygen saturation (SvO_2) estimation method, where the relative peak-to-peak levels of the respiration components are used to determine SvO_2 . Using the same calibration curve, as in Equation 6.1, the method indicates $SpO_2 = 97.2\%$ and $SvO_2 = 93.0\%$. This implies a 4.2% blood oxygen saturation difference between the arterial and the venous blood at the same location. This value does not compare well to other published results [51, 52]; however, it does show that the blood oxygen saturation level

reduces due to metabolic activity and therefore warrants followup. The assumption of using the SpO_2 calibration curve for SvO_2 and the assumption that the lower dominant frequency components directly correspond to venous pulsations need to be carefully reconsidered.

As another example, Figure 41 illustrates a new method to analyze the digital volume pulse (DVP). The raw waveform (black) is compared to a calculated waveform (red), where the red waveform is created by combining the estimated direct wave (blue) and the estimated reflection wave (green). A least-squares approach guides this placement relative to the original raw data. The difference between this interpretation of DVP and the conventional interpretation, as in Figure 2 or Figure 31, is obvious. However, its clinical effectiveness still needs to be verified, and the curve produced by the fitting process must be improved to better match the original data.

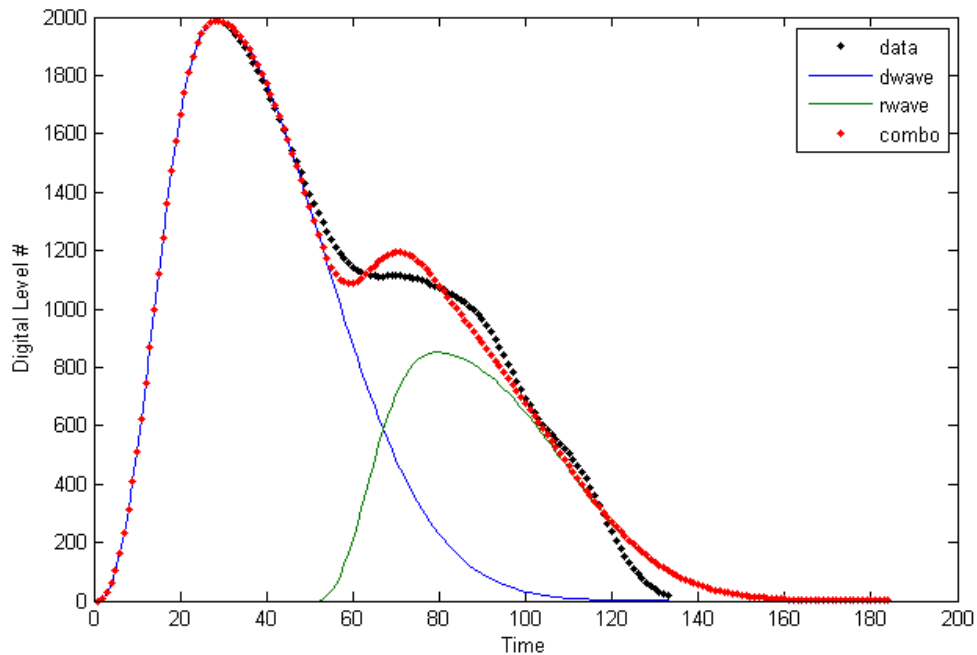


Figure 41. Digital volume pulse analysis using a curve fitting method.

A novel application is also introduced in *Chapter 7*. It brings the element of intelligence into the pulse oximeter design by enabling onboard signal quality verification.

CHAPTER 7 - Feature Detection

The feature detection or decision-making algorithm to assess the viability of a PPG has been mentioned in the previous text. In this chapter, it will be described in more detail. The overall purpose of this algorithm is to help distinguish between usable PPG data, data corrupted with motion artifact, and non-viable data so as to optimize system resources and increase the integrity of stored data.

Algorithm Flow

The main flow of the feature detection algorithm is depicted in Figure 42. Four channels of data, i.e., DC (Red), DC (IR), AC (Red), and AC (IR), are routinely transmitted to a MATLAB interface. The feature detection algorithm implemented on the pulse oximeter starts by intercepting a 3-second segment of these data. Raw data are typically sampled at a high frequency, e.g., 240 Hz, which is overkill for the feature extraction precision and slows down the algorithm implementation speed. Hence, the first step taken into consideration is downsampling the original signal, and the decimation is set to 8, resulting in a 30 Hz sampling frequency for the downsampled signal.

The feature extraction algorithm is activated when the downsampled data are available. Four features are extracted and finally determined at the end of the 3-second segment. The decision is made according to a formerly specified hypothesis testing, decision-making rule [53], and the decision is sent to the MATLAB interface. The decision concerns the following aspects: (1) the degree of motion detected, (2) the quality of the pulsatile signal, and (3) the signal saturation status.

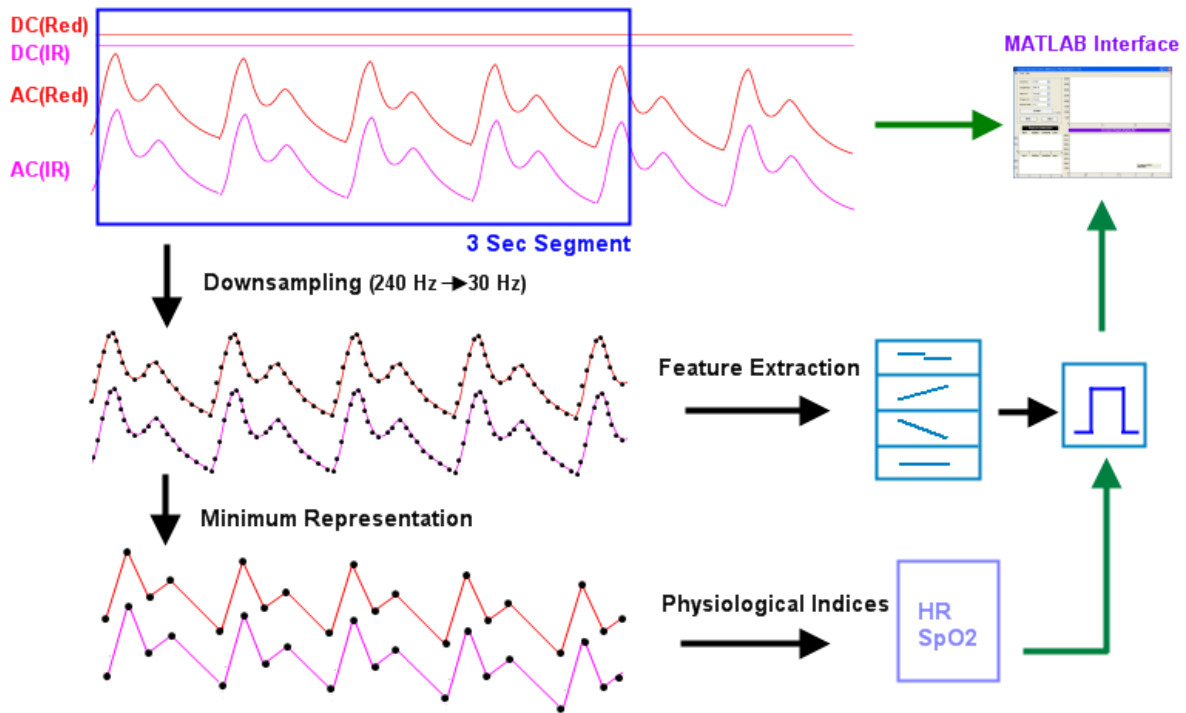


Figure 42. Feature detection algorithm flow.

The minimum representation is created based on triangular structure identification in the downsampled data set. There are normally only two possible structures if the signal is not saturated, as shown in Figure 43. In the blue triangle, the middle point is identified as a local minimum as it is less than the two points on either side of it. Analogously, in the red triangle, the middle point is identified as a local maximum. That is, the blue triangle is considered to be the valley of a certain length of the curve, and the red triangle appears at the peak of a certain length of the curve.

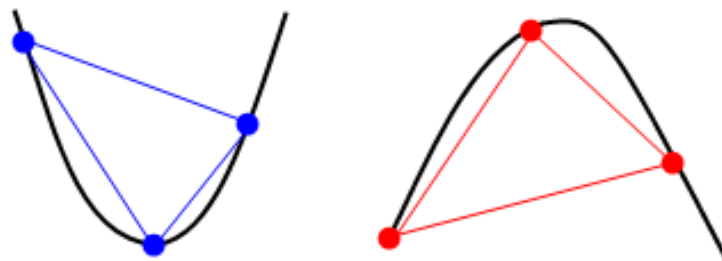


Figure 43. Triangular structures identified for the minimum representations.

If the decision based on features is positive, i.e., a valid pulse signal, then the physiological parameters HR and SpO_2 extracted from the minimum representation are also transmitted to the PC interface. The minimum representation further simplifies the waveform, which is essential to the algorithm implemented on a microprocessor with very limited resources.

The signal processing steps in the algorithm are distributed through each 3-second time segment, which is called “streaming signal processing.” This technique makes the best use of the system resources that remain after the normal pulse oximeter functions are performed, and it is described below using pseudo-code.

```

While (New raw data point yielded)
{
    Decimation count ++;
    Segment count ++;
    Update features with the new data point;
    If (Decimation count == 8)
    {
        Create new downsampled data X;
        Update features with X;
        Add X to Tri[3];
        If (Triangle detected in Tri[3])
        {
            Add X to MR[] array;
        }
        Decimation count = 0;
    }
    If (Segment count == 720)
    {
        Initialize all corresponding variables;
        Set Flag for main();
    }
}

```

This segment of code is included in the timer interrupt routine, and the “Flag” for the *main()* function is set at the end of each 3-second data segment. The algorithm for signal processing on the minimum representation is implemented in *main()*, which leads to an additional 3-second time delay for the calculated HR and SpO_2 values that are transmitted. The pseudo-code for this part of algorithm is described below.

```

While (Flag)
{
    For (i = 1 to length of MR[])
    {
        If ((MR(i)+Tolerance) < MR(i+1))
        {
            Amplitude = MR(i+1) - MR(i);
            Cycle count ++;
        }
    }
    Clear Flag;
}
Perform the same code for the other channel;
Calculate HR and SPO2;

```

Feature Selection

Features that are extracted from the original two channels of photoplethysmographic signal and baseline should be efficient and effective. The more efficient, the less the CPU time (i.e., feature selection should preserve the normal functions of a pulse oximeter), and the more effective, the more reliable the decision. Highly effective features can often require more complicated calculations, e.g., higher order statistics and bi-spectrum analysis as in [54]. The tradeoff between efficiency and effectiveness causes trouble in the feature selection procedure. Four features were eventually selected for these PPG data after many trials: (1) baseline variation, (2) upstairs count, (3) downstairs count, and (4) level count.

To statistically validate these features, a total of 20 photoplethysmogram measurements were collected from 20 subjects. Each measurement lasted more than 30 seconds to ensure ten 3-second segments. Features were extracted from each segment, and the mean and standard deviation of each feature were calculated for each person. The 20 mean and standard-deviation pairs were finally depicted in a bar chart.

Toward the extraction of Feature 1, one can note that the baseline is adjusted for signal saturation prevention and that motion is the dominant cause of signal saturation or severe fluctuation. Hence, frequent changes of baseline value suggest that motion is present or that the signal amplitude itself is too large, i.e., already saturated. The latter condition is usually temporary and soon disappears via the LED intensity autoregulation mechanism.

Feature 1 is the only feature directly obtained from the 720 points in a raw data segment. When the value in the baseline channel varies, Feature 1 increases by one. The maximum of

Feature 1 is 719, but a threshold is set to 255 so as to limit the value to one byte of storage space. Figure 44 illustrates the Feature 1 statistics in 20 patients. All bars are below 120, and the mean is 47.

A similar bar chart for motion-corrupted photoplethysmograms is hard to create. The primary problems are the lack of a clear method to quantify the motion degree and a sensible means to identify the minimum degree of motion that is acceptable. However, this problem can be viewed from a different perspective. If an appropriate initial threshold is created to distinguish severe motion, it can be manually trimmed to a degree of satisfaction. 100 is chosen as the Feature 1 threshold, which works fine in initial tests.

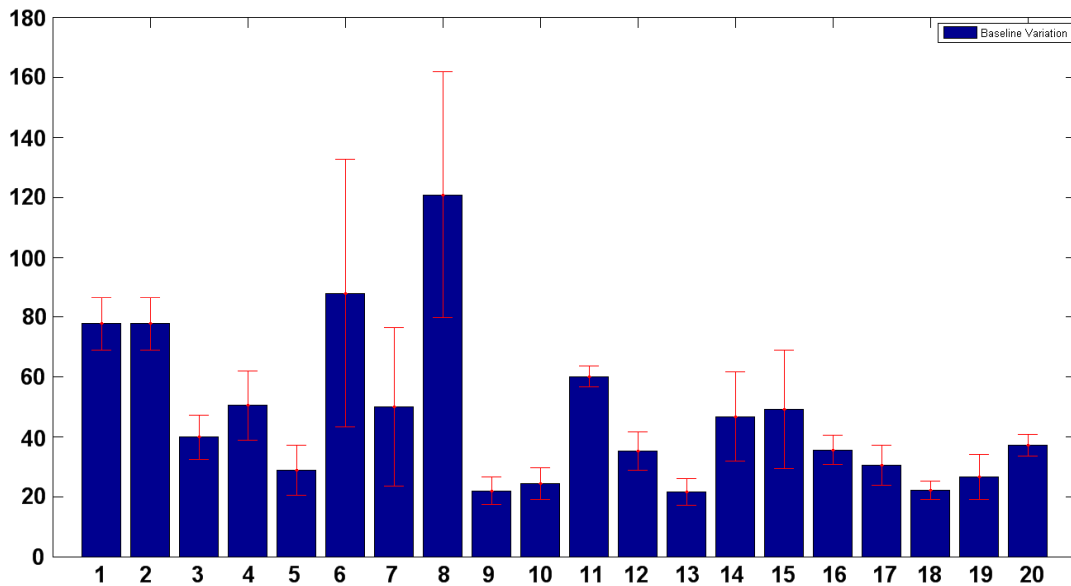


Figure 44. Feature 1: baseline variation.

The other three features are closed related, as they track the type of variation in 90 points of downsampled data in a segment. The pseudo-code below shows how it works.

```

If (Data(i+1) > Data(i))
{
    Upstairs ++;
}
Else if (Data(i+1) < Data(i))
{
    Downstairs ++;
}
Else
{
    Level ++;
}

```

Figure 45, Figure 46, and Figure 47 depict the statistics of these three features for the 20 subjects. Feature 2 (upstairs count) is of mean 28, Feature 3 (downstairs count) is of mean 60, and Feature 4 (level count) is less than 1. The fluctuations of these features are slight, with a standard deviation less than 4.

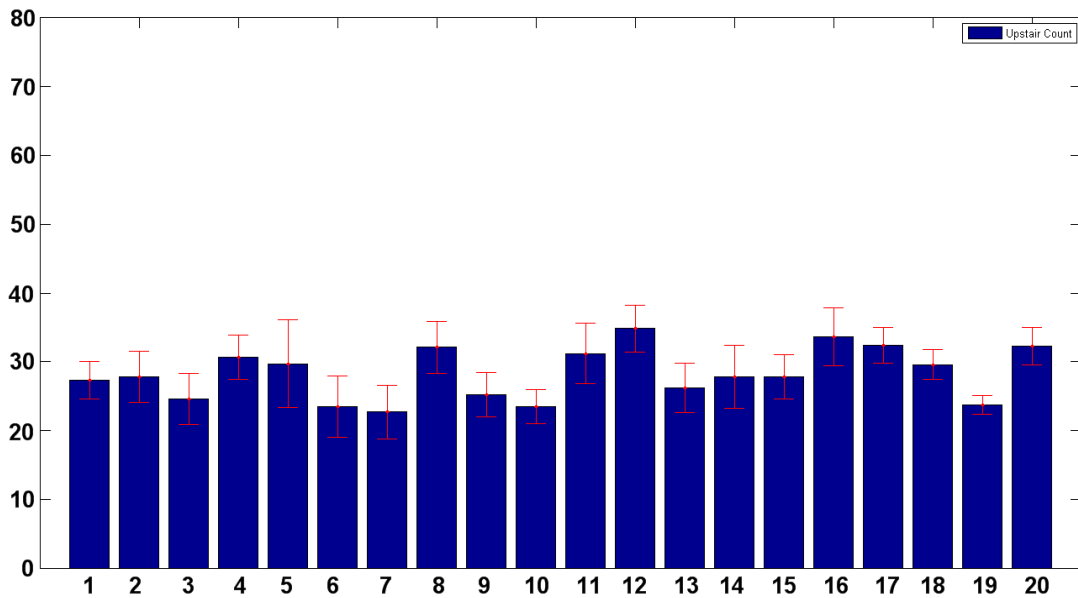


Figure 45. Feature 2: upstairs count.

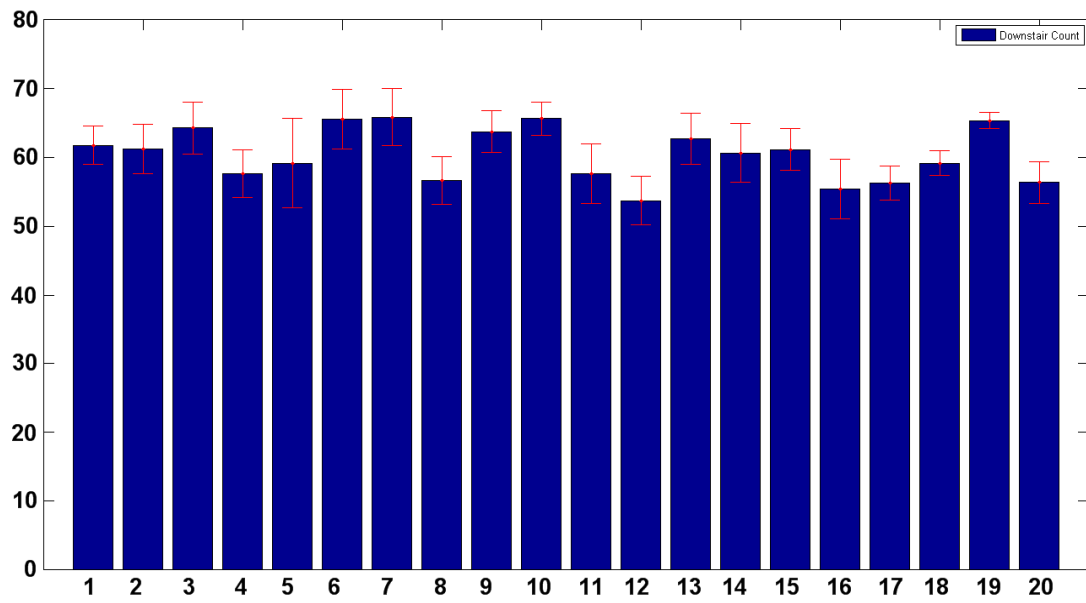


Figure 46. Feature 3: downstairs count.

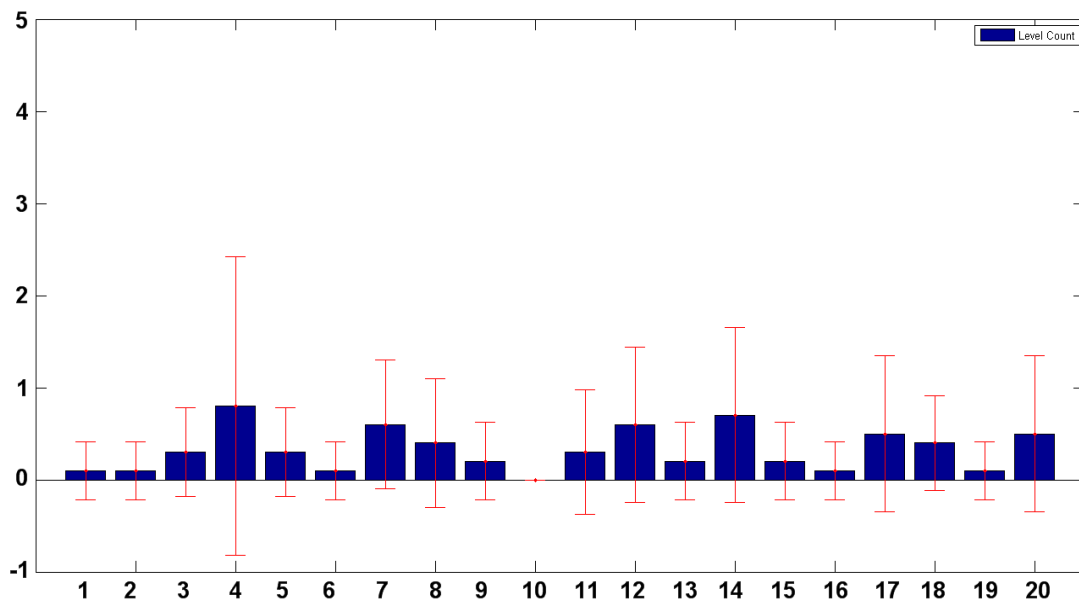


Figure 47. Feature 4: level count.

Feature 4 is obviously a good indicator of signal saturation, as the points in saturation are always at the boundary value: 0 or 4095. Analogous to the motion threshold situation, the saturation threshold can be specified subjectively: 8 is used to indicate signal saturation.

The ratio of Feature 3 and Feature 2 would be interesting to investigate, as demonstrated in Figure 48. The mean of 2.2 is a sensible description of the asymmetry of a single-cycle pulsatile waveform, which features a steep up-slope and a mild down-slope. The physiological reason for this is that the diastolic cycle is roughly two times longer than the systolic cycle.

This special ratio is seldom created by normal motion and ambient noise. For instance, when the pulse oximeter is taken off of the patient and laid on the desktop to pick up ambient light, the signal would be much like a sinusoid, and the ratio would be close to 1. If periodic motion is simulated, it also creates a sinusoid-like signal on the pulse oximeter.

The same problem then appears as before: how to define the motion types and their specifications, e.g., the time percentage of moving an arm up in an up-down cycle. This is difficult, so the same approach of manually and subjectively setting the threshold was found to be the most effective approach. 2 is selected as a threshold for a valid pulse, and 1.1 is selected as a threshold for no pulse.

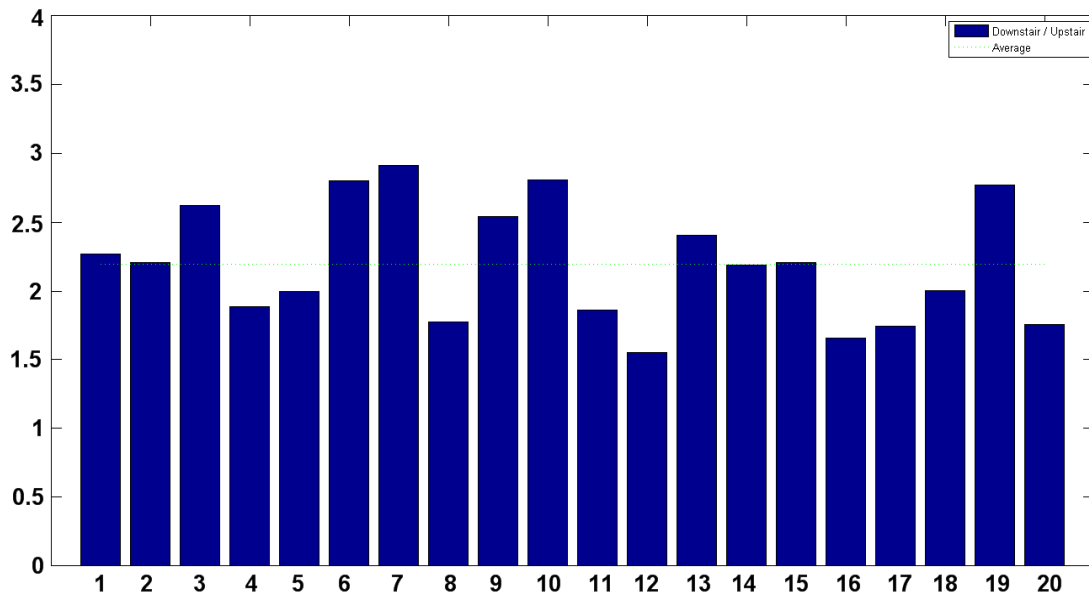


Figure 48. Ratio of downstairs count to upstairs count.

Initial Results and Discussion

Figure 49 shows an example of the downsampling process, and the downsampled signal still contains viable characteristics of the raw signal. Hence, it is an effective step to lessen the operational burden.

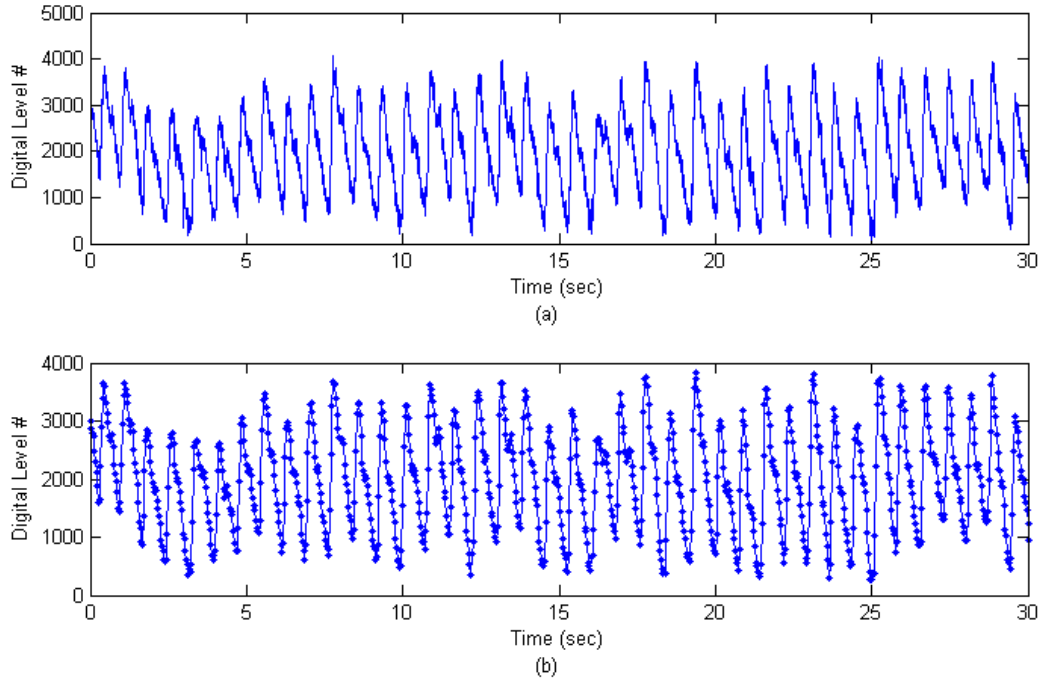


Figure 49. An example of a downsampled waveform (b) obtained from an original photoplethysmographic signal (a).

Figure 50 illustrates the first 9 minimum-representation segments from the downsampled signal in Figure 49. Each segment contains 3-4 cycles, where much fewer data points are needed to depict the waveform characteristics, i.e., foot, peak, and notch on the slope.

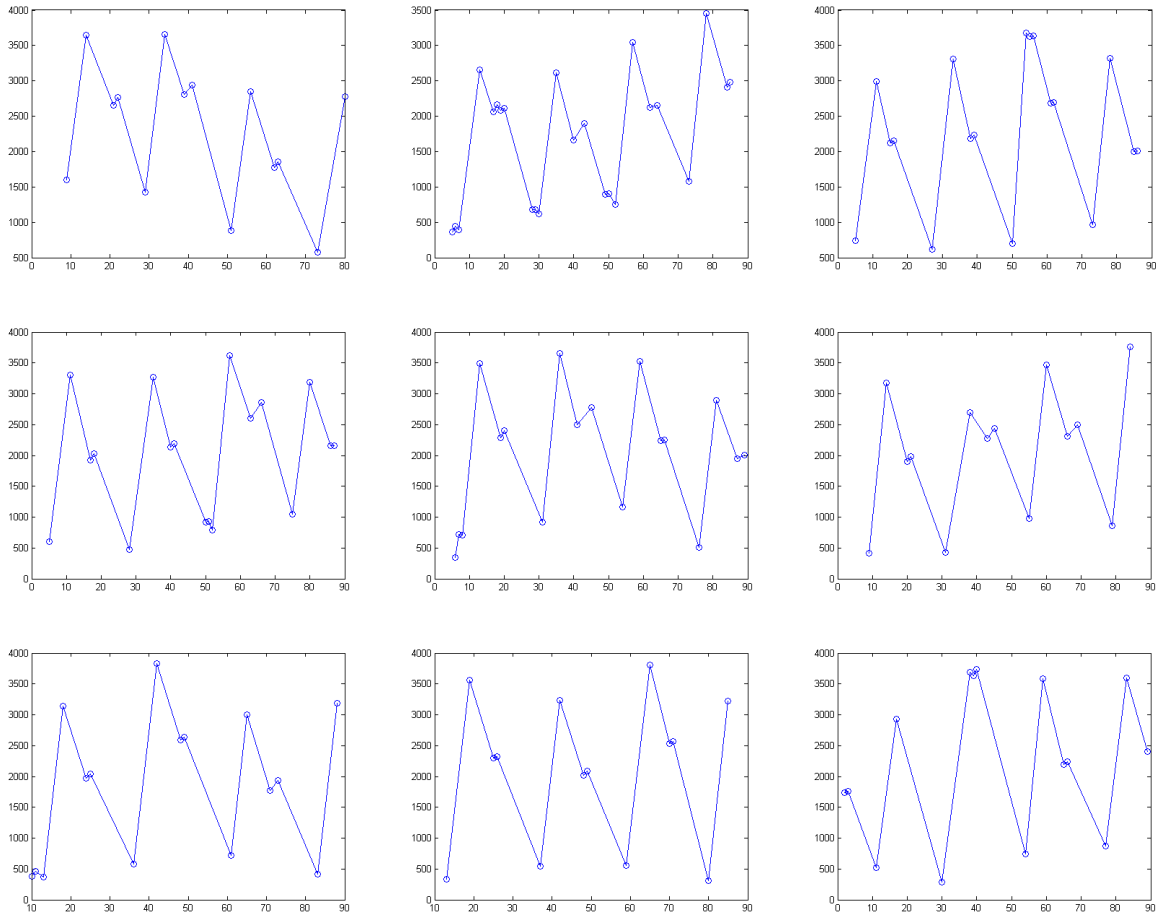


Figure 50. An example of 9 minimum representations from the first 27 seconds of data in the downsampled photoplethysmogram.

Figure 51, Figure 52, Figure 53, and Figure 54 demonstrate four different situations identified for the pulse oximeter with the feature detection algorithm. The segments are depicted using alternating red and blue colors, and their corresponding features are presented in two smaller plots in the lower left of each figure. The decision shown on the purple bar is only based on the subjectively-specified thresholds, but it works just fine and is capable of further adjustment. Additionally, the minimum-representation data are always transmitted and presented in the current debugging phase.

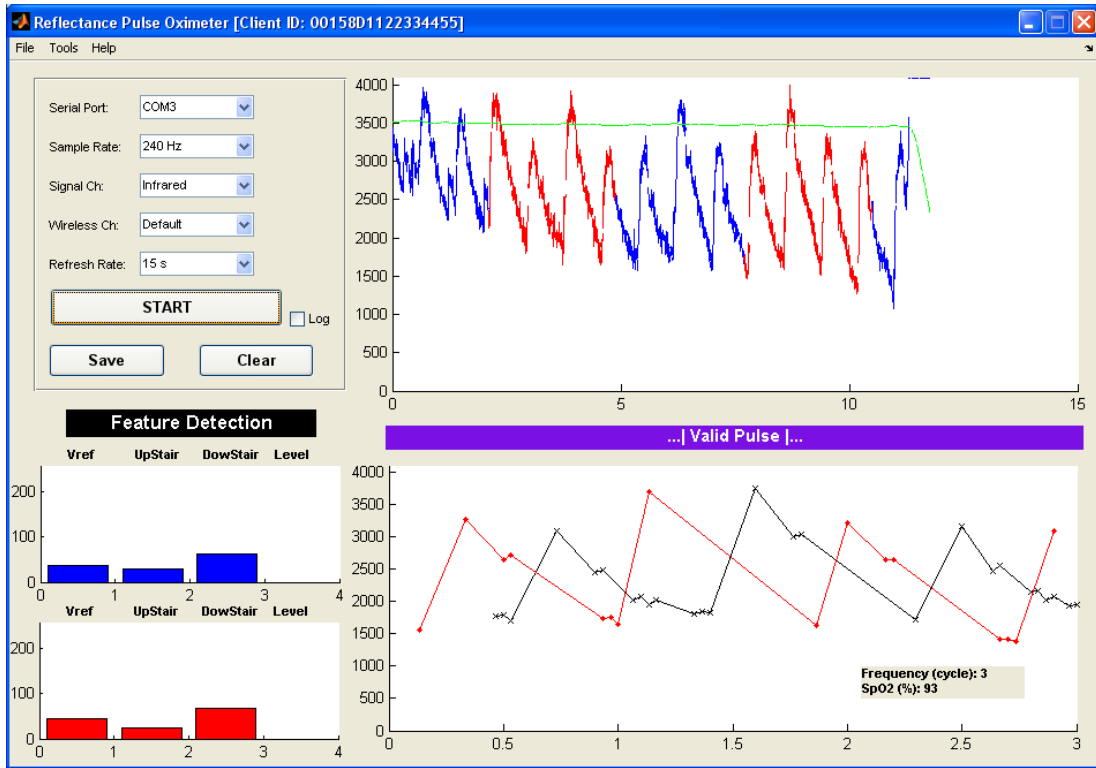


Figure 51. Valid pulse presented in feature detection.

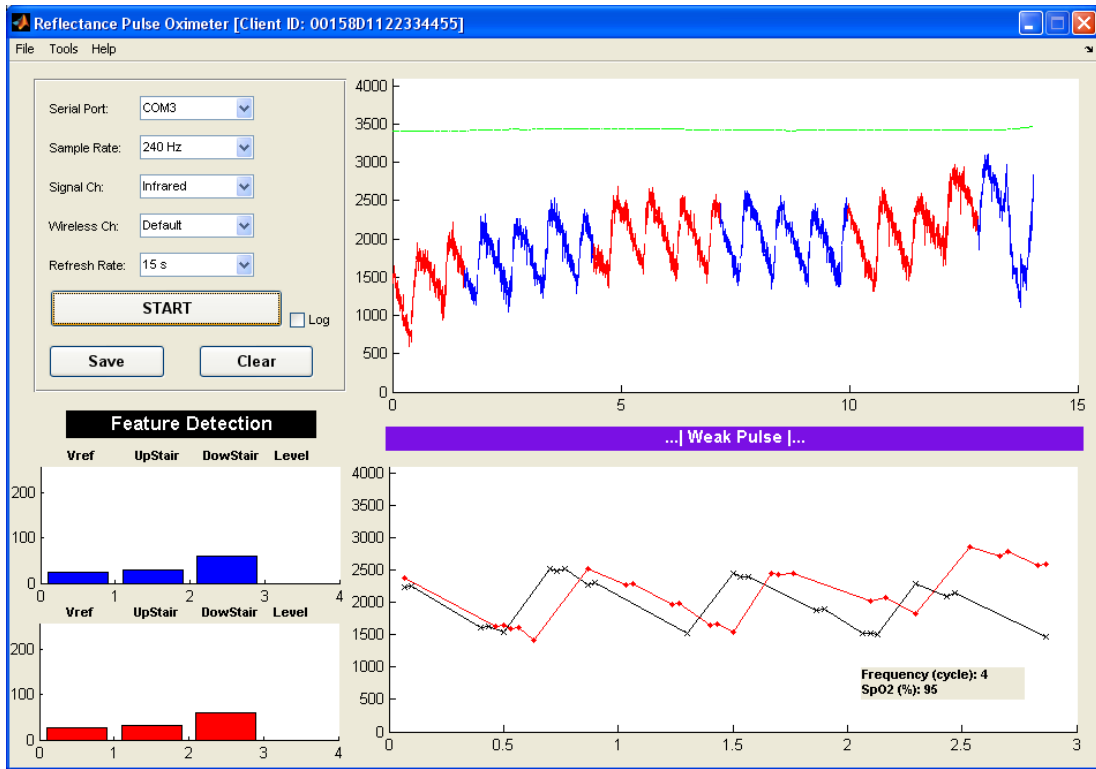


Figure 52. Weak pulse presented in feature detection.

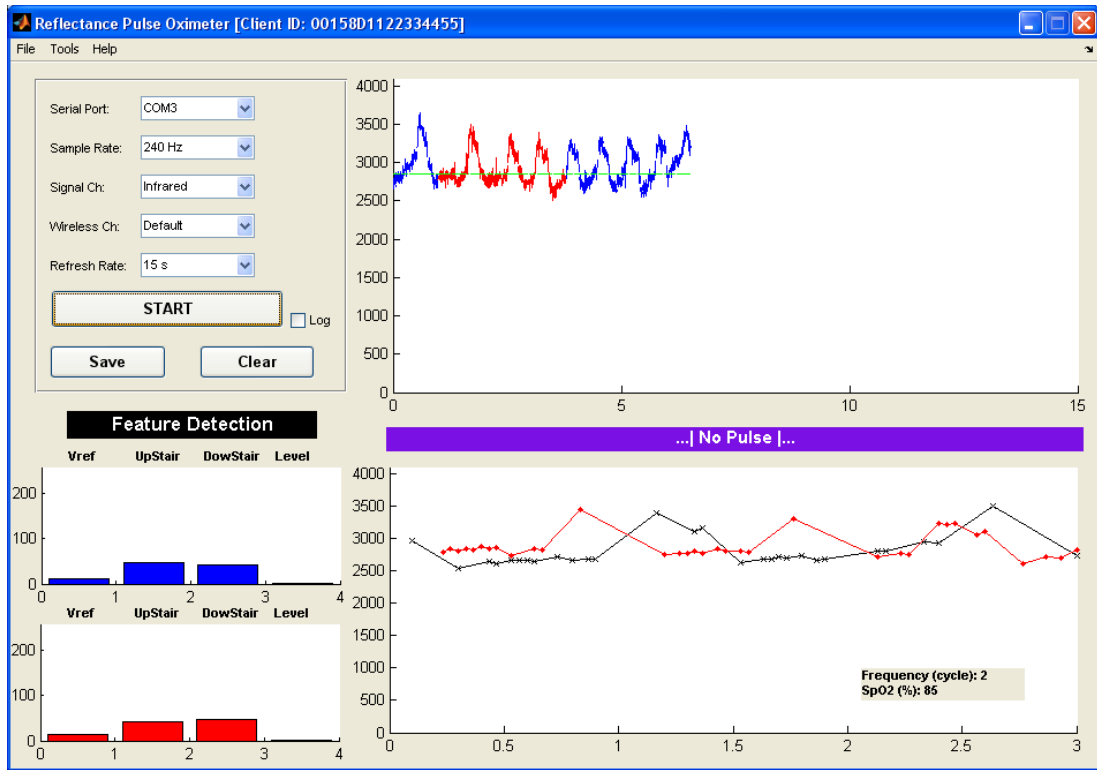


Figure 53. No pulse identified in feature detection.

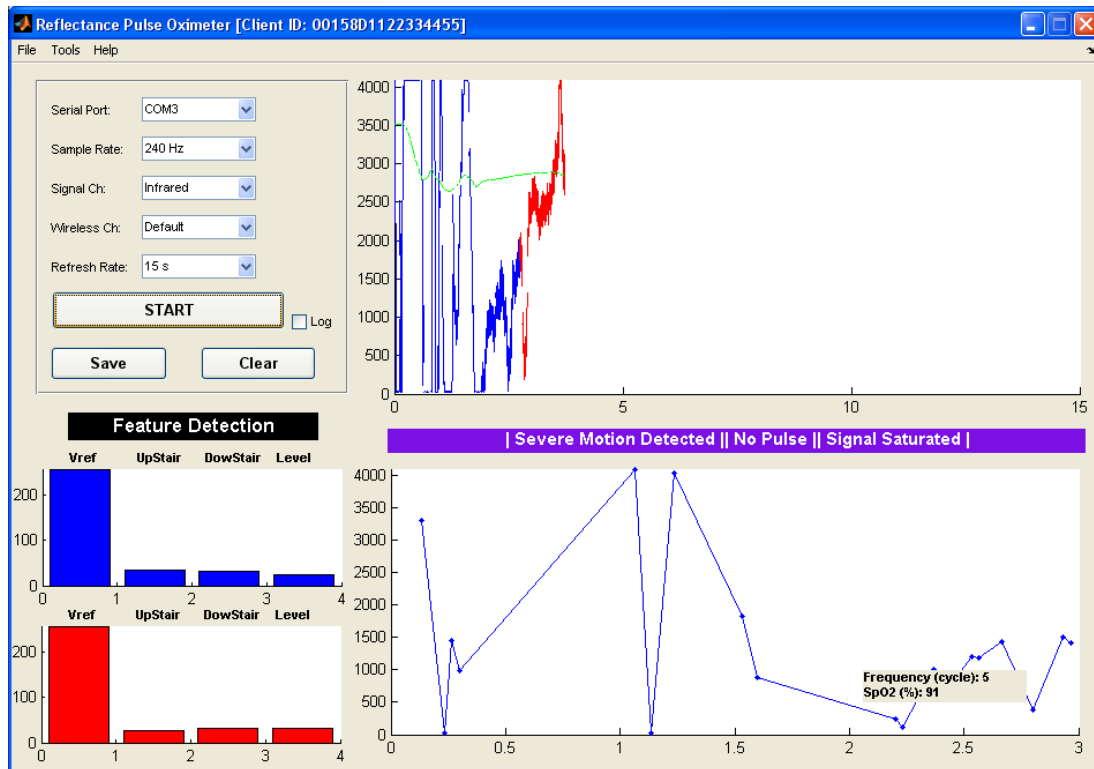


Figure 54. Severe motion and signal saturation identified in feature detection.

CHAPTER 8 - Conclusion

Two versions of a novel wireless reflectance pulse oximeter were successfully devised, from a unique control system design to the final manufactured prototypes. Version 1 suits the situation of a fixed vascular profile, where the LED intensity is manually optimized. Featuring new LED control circuitry, version 2 is capable of automatic LED intensity adjustment, which optimizes the intensity level according to the subject's vascular profile and the current ambient condition.

Utilizing the filter-free control system featuring two-stage feedback loops, an LED intensity regulator, and a signal saturation inhibitor, the process to generate high-fidelity photoplethysmographic signals becomes straightforward and effective. The pulse oximeter exhibited excellent performance with respect to photoplethysmogram measurement ease and quality, and the resultant signals proved the effectiveness of the distortion-free and corruption-resistant design. These signals are sampled at a high sampling rate and contain thousands of digitization levels. Although no onboard filtering technique was adopted, high-quality photoplethysmographic signals can be acquired from multiple body locations, and signal noise can be easily eliminated using a high-order linear-phase digital filter.

MATLAB GUIs were developed for different applications, where the primary tasks include data acquisition, visualization, restoration, and post-processing. Regarding educational applications, the new wireless pulse oximeter units and their accompanying MATLAB interfaces were initially applied within the context of the Fall 2009 *ECE 772 - Biomedical Instrumentation* laboratory course, and excellent results were achieved. A successful feature approach was also implemented to identify the presence of valid versus non-usable data, where the corresponding MATLAB interface depicted the raw waveform, the extracted features, the minimum signal representation, and the final decision determined by the pulse oximeter which ran the feature detection algorithm in embedded code.

With the availability of the novel high-fidelity reflectance wireless pulse oximeter, more applications and research goals are waiting to be explored. Each potential clinical parameter listed in Table 1 can be further pursued due to the reliable measurement results demonstrated here.

Future Work

Future work can be considered in two respects: device improvement and signal interpretation and processing. A case and a set of wearability add-ons (e.g., “wrist watch” packaging) for the pulse oximeter will make the unit more robust and make measurements easier and more conformant to current clinical needs. The performance of the device can be upgraded by employing a more powerful microprocessor if needed; a good candidate has appeared on the market with a model number JN5148. Although this device is designed to resist motion and inhibit saturation, work can be done to reinforce this area.

In the application of severe motion detection and reduction, the decision-making algorithm informs the system of severe motion emergence, and then the LED intensity regulator automatically lowers the current driving the LED to ensure that the signal is not saturated, improving the likelihood of signal restoration. Since the decision-making algorithm is primarily based on the feature detection process of the second-stage signal, it would be interesting to note the performance difference if motion information were read from an accelerometer directly. Hence, a 3-axis accelerometer with an I²C bus interface, the STMicroelectronics LIS3LV02DL, is intended to be integrated into the pulse oximeter prototype, allowing real-time motion artifact reduction to be realized, as in [25, 28].

In terms of photoplethysmographic signal interpretation and physiological information extraction, this area is disjoint from electrical engineering and presents a challenge in terms of device design and signal processing. Physiologists and medical researchers have been working in this area since the early 1960s, and plenty of literature exists to help understand the origin and makeup of the photoplethysmographic signal. Unique opportunities exist to extract clinically meaningful cardiovascular parameters using these highly functional, light-based devices.

References

- [1] J. Allen and A. Murray, "Modelling the Relationship Between Peripheral Blood Pressure and Blood Volume Pulses Using Linear and Neural Network System Identification Techniques," *Physiological Measurement*, vol. 20, pp. 287–301, 1999.
- [2] S. C. Millasseau, F. G. Guigui, R. P. Kelly, K. Prasad, J. R. Cockcroft, J. M. Ritter, and P. J. Chowienczyk, "Noninvasive Assessment of the Digital Volume Pulse : Comparison with the Peripheral Pressure Pulse," *Hypertension*, vol. 36, pp. 952-956, 2000.
- [3] J. Penaz, "Photoelectric Measurement of Blood Pressure, Volume and Flow in the Finger," in *Digest of the 10th International Conference on Medical and Biological Engineering*, Dresden, Germany, 1973, p. 104.
- [4] N. Westerhof, N. Stergiopoulos, and M. I. M. Noble, *Snapshots of Hemodynamics*, 1st ed. Boston: Springer, 2004.
- [5] W. Welkowitz, *Engineering Hemodynamics: Application to Cardiac Assist Devices*, 2nd ed. New York: New York University Press, 1987.
- [6] C. Roberts, *Blood Flow Measurement*. London: Sector Publishing Limited, 1972.
- [7] K. H. Shelley, W. B. Murray, and D. Chang, "Arterial-Pulse Oximetry Loops: A New Method of Monitoring Vascular Tone," *Journal of Clinical Monitoring*, vol. 13, pp. 223-228, 1997.
- [8] A. Reisner, P. A. Shaltis, D. McCombie, and H. H. Asada, "Utility of the Photoplethysmogram in Circulatory Monitoring," *Anesthesiology*, vol. 108, pp. 950-958, May 2008.
- [9] J. Li, L. Yang, S. Zhang, and Y. Yang, "Computation of Cardiac Output by Pulse Wave Contour," in *1st International Conference on Bioinformatics and Biomedical Engineering*, Wuhan, 2007, pp. 1088-1090.
- [10] K. Meigas, R. Kattai, and J. Lass, "Continuous Blood Pressure Monitoring Using Pulse Wave Delay," in *23rd Annual International Conference of the IEEE EMBS*, Oct. 25-28, 2001, pp. 3171-3174.
- [11] C. C. Y. Poon, Y.-T. Zhang, and Y. Liu, "Modeling of Pulse Transit Time under the Effects of Hydrostatic Pressure for Cuffless Blood Pressure Measurements," in *3rd IEEE-EMBS International Summer School and Symposium on Medical Devices and Biosensors*, MIT, Boston, Sep. 4-6, 2006.
- [12] S. R. Alty, N. Angarita-Jaimes, S. C. Millasseau, and P. J. Chowienczyk, "Predicting Arterial Stiffness From the Digital Volume Pulse Waveform," *IEEE Transactions on Biomedical Engineering*, vol. 54, pp. 2268-2275, Dec. 2007.

- [13] S. C. Millasseau, R. P. Kelly, J. M. Ritter, and P. J. Chowienczyk, "Determination of Age-Related Increases in Large Artery Stiffness by Digital Pulse Contour Analysis," *Clinical Science (London)*, vol. 103, pp. 371–377, Oct. 2002.
- [14] K. Li and S. Warren, "A High-Performance Wireless Reflectance Pulse Oximeter for Photo-Plethysmogram Acquisition and Analysis in the Classroom," in *2010 Annual Conference and Exposition of the ASEE*, Louisville, KY, June 20-23, 2010.
- [15] K. H. Shelley, "Photoplethysmography: Beyond the Calculation of Arterial Oxygen Saturation and Heart Rate," *Anesthesia & Analgesia*, vol. 105, pp. S31-S36, 2007.
- [16] P. A. Leonard, J. G. Douglas, N. R. Grubb, D. Clifton, P. S. Addison, and J. N. Watson, "A Fully Automated Algorithm for the Determination of Respiratory Rate from the Photoplethysmogram," *Journal of Clinical Monitoring and Computing*, vol. 20, pp. 33-36, 2006.
- [17] L. Nilsson, A. Johansson, and S. Kalman, "Respiration can be monitored by photoplethysmography with high sensitivity and specificity regardless of anaesthesia and ventilatory mode," *Acta Anaesthesiol Scand*, vol. 49, pp. 1157-62, 2005.
- [18] M. Nitzan, I. Faib, and H. Friedman, "Respiration-Induced Changes in Tissue Blood Volume Distal to Occluded Artery, Measured by Photoplethysmography," *Journal of Biomedical Optics*, vol. 11, p. 040506, 2006.
- [19] B. Khanokh, Y. Slovik, D. Landau, and M. Nitzan, "Sympathetically Induced Spontaneous Fluctuations of the Photoplethysmographic Signal," *Medical and Biological Engineering and Computing*, vol. 42, pp. 80-85, 2004.
- [20] K. A. Reddy, B. George, and V. J. Kumar, "Use of Fourier Series Analysis for Motion Artifact Reduction and Data Compression of Photoplethysmographic Signals," *IEEE Transactions on Instrumentation and Measurement*, vol. 58, pp. 1706-1711, May 2009.
- [21] B. S. Kim and S. K. Yoo, "Motion Artifact Reduction in Photoplethysmography Using Independent Component Analysis," *IEEE Transactions on Biomedical Engineering*, vol. 53, pp. 566-568, March 2006.
- [22] J. Y. A. Foo, "Comparison of Wavelet Transformation and Adaptive Filtering in Restoring Artefact-Induced Time-Related Measurement," *Biomedical Signal Processing and Control*, vol. 1, pp. 93-98, Jan. 2006.
- [23] C. M. Lee and Y. T. Zhang, "Reduction of Motion Artifacts from Photoplethysmographic Recordings Using a Wavelet Denoising Approach," in *2003 Asian-Pacific Conference of the IEEE EMBS*, 2003, pp. 194-195.
- [24] K. W. Chan and Y. T. Zhang, "Adaptive Reduction of Motion Artifact from Photoplethysmographic Recordings Using a Variable Step-Size LMS Filter," in *2002 IEEE Proceedings on Sensors*, 2002, pp. 1343-1346.

- [25] H. Han, M.-J. Kim, and J. Kim, "Development of Real-Time Motion Artifact Reduction Algorithm for a Wearable Photoplethysmography," in *29th Annual Conference of the IEEE EMBS*, 2007, pp. 1538-1541.
- [26] J. Yao and S. Warren, "A Short Study to Assess the Potential of Independent Component Analysis for Motion Artifact Separation in Wearable Pulse Oximeter Signals," in *27th Annual Conference of the IEEE EMBS*, 2005, pp. 3585-3588.
- [27] J. Yao and S. Warren, "A Novel Algorithm to Separate Motion Artifacts from Photoplethysmographic Signals Obtained with a Reflectance Pulse Oximeter," in *26th Annual International Conference of the IEEE EMBS*, San Francisco, CA, Sep. 1-5, 2004, pp. 2153-2156.
- [28] G. Comtois and Y. Mendelson, "A Comparative Evaluation of Adaptive Noise Cancellation Algorithms for Minimizing Motion Artifacts in a Forehead-Mounted Wearable Pulse Oximeter," in *29th Annual International Conference of the IEEE EMBS*, Lyon, France, Aug. 23-26, 2007, pp. 1528-1531.
- [29] K. Li and S. Warren, "High-Fidelity Wireless Reflectance Pulse Oximetry Based on Filter-Free and Surface-Integratable Design," unpublished.
- [30] H. Asada, P. Shaltis, A. Reisner, S. Rhee, and R. Hutchinson, "Mobile Monitoring with Wearable Photoplethysmographic Biosensors," in *IEEE Engineering in Medicine and Biology Magazine*, vol. 22, 2003, pp. 28-40.
- [31] Smiths Medical PM, Inc., "How can SpO₂ readings differ from manufacturer to manufacturer?," 2006, <http://www.smiths-medical.com>.
- [32] J. E. Scharf, S. Athan, and D. Cain, "Pulse Oximetry Through Spectral Analysis," in *12th Southern Biomedical Engineering Conference*, New Orleans, LA, 1993, pp. 227-229.
- [33] Y. Mendelson, P. W. Cheung, M. R. Neuman, D. G. Fleming, and S. D. Cahn, "Spectrophotometric Investigation of Pulsatile Blood Flow for Transcutaneous Reflectance Oximetry," *Advances in Experimental Medicine and Biology*, vol. 159, pp. 93-102, 1983.
- [34] B. Roberts, "Capturing Grid Power," *IEEE Power and Energy Magazine*, vol. 7, pp. 32-41, 2009.
- [35] S. Rhee, B. H. Yang, and H. Asada, "Artifact-Resistant, Power-Efficient Design of Finger-Ring Plethysmographic Sensors," *IEEE Transactions on Biomedical Engineering*, vol. 48, pp. 795-805, July 2001.
- [36] D. Thompson and S. Warren, "A Small, High-Fidelity Reflectance Pulse Oximeter," in *2007 Annual Conference and Exposition of the ASEE*, Honolulu, HI, June 24-27, 2007.

- [37] M. R. Yuce and C. K. Ho, "Implementation of Body Area Networks Based on MICS/WMTS Medical Bands for Healthcare Systems," in *30th Annual Conference of the IEEE EMBS*, Aug. 20-25, 2008, pp. 3417-3421.
- [38] J. W. Hui and D. E. Culler, "Extending IP to Low-Power, Wireless Personal Area Networks," in *IEEE Internet Computing*. vol. 12, July-Aug. 2008, pp. 37-45.
- [39] Jennic Ltd. , "Data Sheet: JN5139-001 and JN5139-Z01," 2008, <http://www.jennic.com>.
- [40] Jennic Ltd. , "Preliminary Data Sheet – JN5139-xxx-Myy," 2008, <http://www.jennic.com>.
- [41] Jennic Ltd. , "DR1080 Starter Kit Board Reference Manual " 2008, <http://www.jennic.com>.
- [42] Jennic Ltd. , "What Are the Minimum Connections Required for Programming Modules?," 2008, <http://www.jennic.com>.
- [43] Jennic Ltd. , "Jenie API Reference Manual (JN-RM-2035)," 2008, <http://www.jennic.com>.
- [44] Jennic Ltd. , "Jenie API User Guide (JN-UG-3042)," 2009, <http://www.jennic.com>.
- [45] Wikipedia, "RS-232," 2010, <http://en.wikipedia.org/wiki/RS232>.
- [46] J. T. Love, S. Warren, G. R. Laguna, and T. J. Miller, "Personal Status Monitor," Sandia National Laboratories SAND97-0418, Feb. 1997.
- [47] P. A. Kyriacou, S. Powell, R. M. Langford, and D. P. Jones, "Esophageal Pulse Oximetry Utilizing Reflectance Photoplethysmography," *IEEE Transactions on Biomedical Engineering*, vol. 49, pp. 1360-1368, 2002.
- [48] P. J. Chowienczyk, R. P. Kelly, H. MacCallum, S. C. Millasseau, T. L. G. Andersson, R. G. Gosling, J. M. Ritter, and E. E. Änggård, "Photoplethysmographic Assessment of Pulse Wave Reflection: Blunted Response to Endothelium-Dependent Beta2-Adrenergic Vasodilation in Type II Diabetes Mellitus," *Journal of the American College of Cardiology*, vol. 34, pp. 2007–2014, 1999.
- [49] E. Geun, H. Heo, K. C. Nam, and Y. Huh, "Measurement Site and Applied Pressure Consideration in Wrist Photoplethysmography," in *23rd ITC-CSCC*, 2008, pp. 1129-1132.
- [50] J. Yao and S. Warren, "Stimulating Student Learning with a Novel 'In House' Pulse Oximeter Design," in *2005 Annual Conference and Exposition of the ASEE*, Portland, OR, June 12-15, 2005, pp. 12-15.
- [51] M. Nitzan, A. Babchenko, and B. Khanokh, "Measurement of Oxygen Saturation in Venous Blood by Dynamic Near Infrared Spectroscopy," *Journal of Biomedical Optics* vol. 5, pp. 155-162, April 2000.

- [52] A. Keys, "The Oxygen Saturation of the Venous Blood in Normal Human Subjects," *American Journal of Physiology*, vol. 124, pp. 13-21, 1938.
- [53] H. V. Poor, *An Introduction to Signal Detection and Estimation*, 2nd ed. New York: Springer-Verlag, 1994.
- [54] R. Krishnan, B. Natarajan, and S. Warren, "Two-Stage Approach for Detection and Reduction of Motion Artifacts in Photoplethysmographic Data," *IEEE Transactions on Biomedical Engineering*, to be published.

Appendix A - Hardware Schematics

Pulse Oximeter Version 1

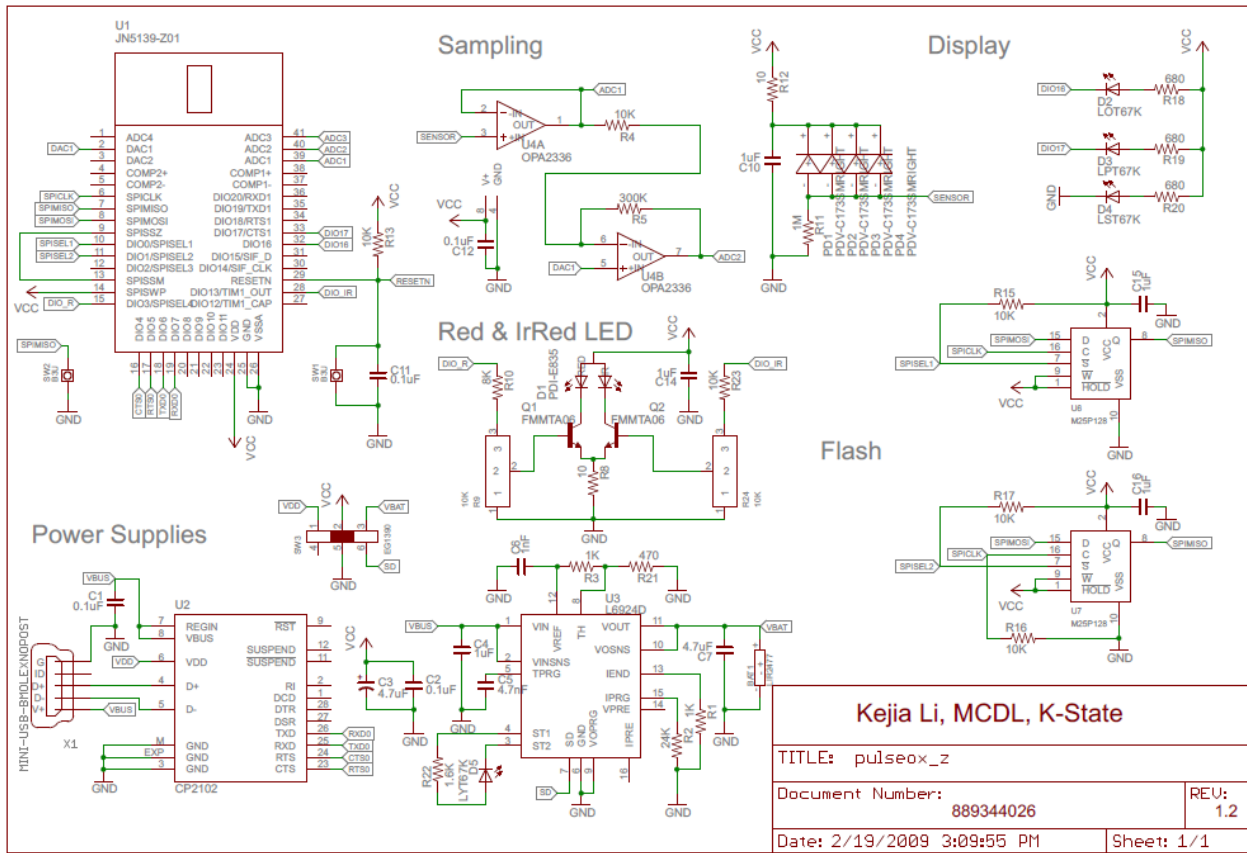


Figure 55. Pulse oximeter version 1 schematic.

Pulse Oximeter Version 2

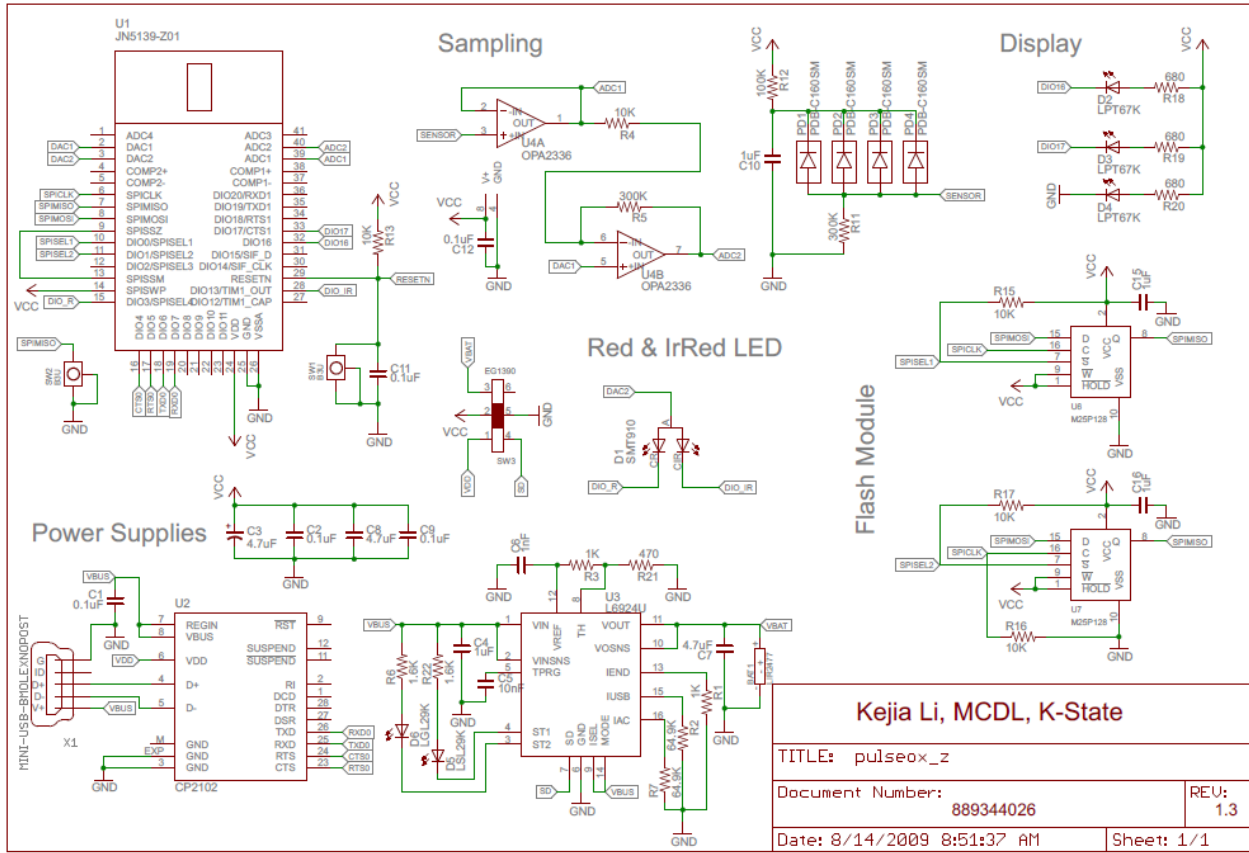


Figure 56. Pulse oximeter version 2 schematic.

Appendix B - Hardware PCB

Pulse Oximeter Version 1

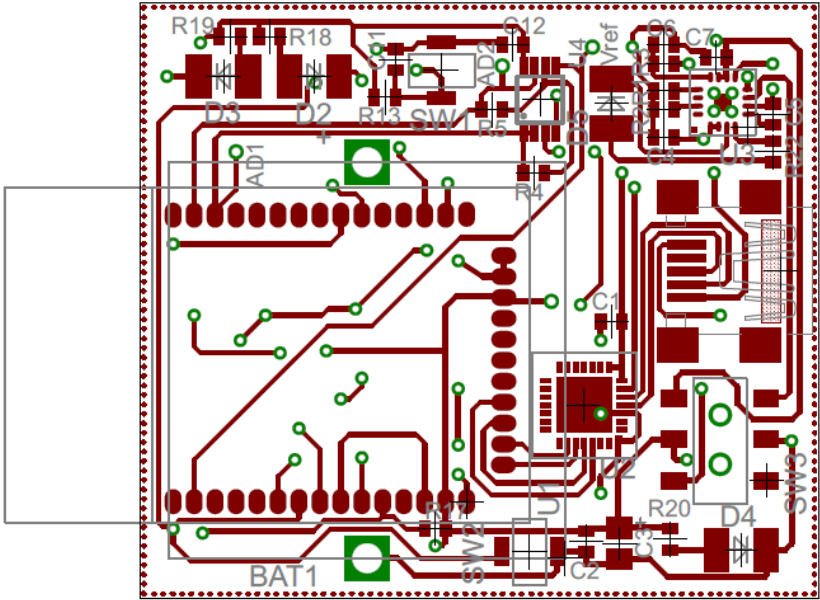


Figure 57. Pulse oximeter version 1 PCB (top view).

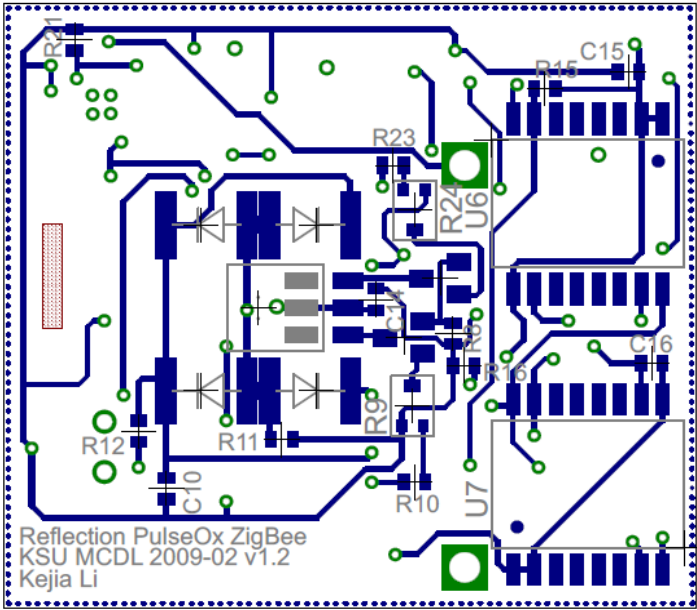


Figure 58. Pulse oximeter version 1 PCB (bottom view).

Pulse Oximeter Version 2

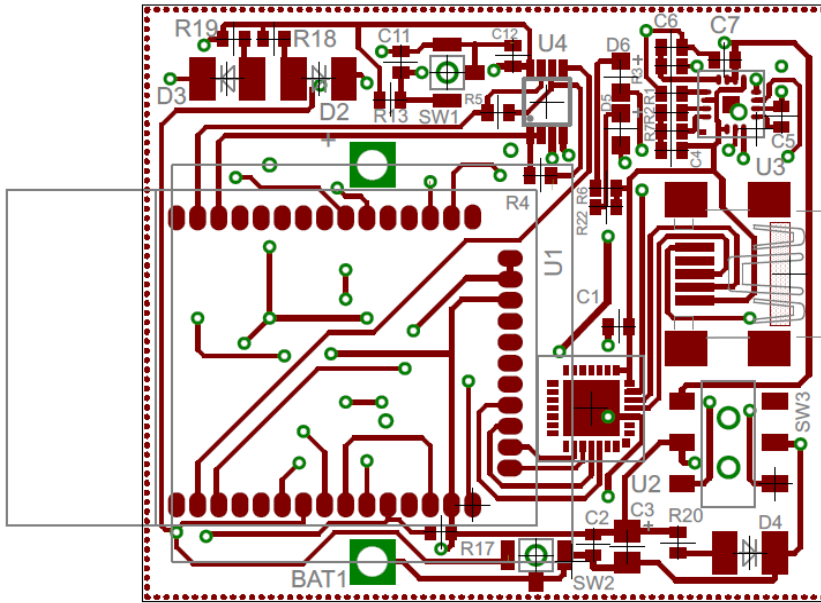


Figure 59. Pulse oximeter version 2 PCB (top view).

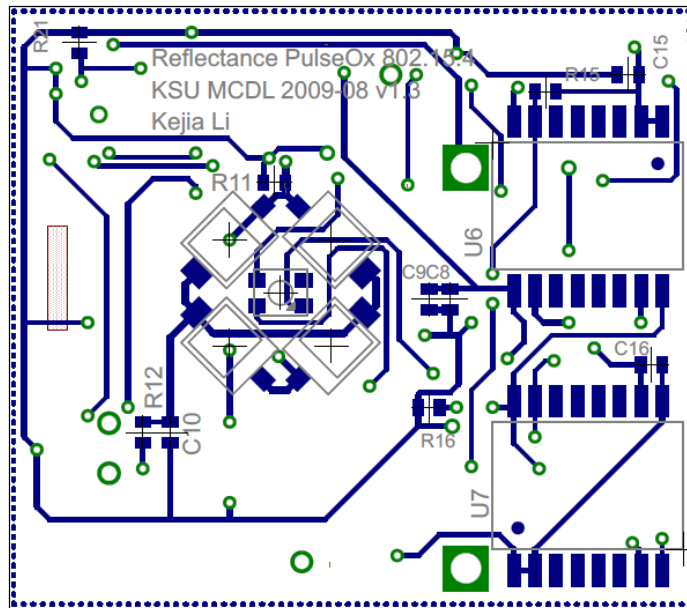


Figure 60. Pulse oximeter version 2 PCB (bottom view).

Appendix C - Hardware Parts Lists

Pulse Oximeter Version 1

Table 8. Pulse oximeter version 1 parts list.

Part	Value	Device	Package
BAT1	LIR2477	LIR2477	LIR2477
C1	0.1uF	C_NP	0402
C2	0.1uF	C_NP	0402
C3	4.7uF	C_P0805	0805P
C4	1uF	C_NP	0402
C5	10nF	C_NP	0402
C6	1nF	C_NP	0402
C7	4.7uF	C_NP	0402
C10	1uF	C_NP	0402
C11	0.1uF	C_NP	0402
C12	0.1uF	C_NP	0402
C14	1uF	C_NP	0402
C15	1uF	C_NP	0402
C16	1uF	C_NP	0402
D1	PDI-E835	PDI-E835	PDI-E835
D2	LOT67K	LOT67K	LEDPAD
D3	LPT67K	LPT67K	LEDPAD
D4	LST67K	LST67K	LEDPAD
D5	LYT67K	LYT67K	LEDPAD
PD1	PDV-C173SM	PDV-C173SM	PDV-C173SM-CORRECT
PD2	PDV-C173SM	PDV-C173SM	PDV-C173SM-CORRECT
PD3	PDV-C173SM	PDV-C173SM	PDV-C173SM-CORRECT
PD4	PDV-C173SM	PDV-C173SM	PDV-C173SM-CORRECT
Q1	FMMTA06	FMMTA06	SOT23-BEC
Q2	FMMTA06	FMMTA06	SOT23-BEC
R1	1K	R0402	0402
R2	64.9K	R0402	0402
R3	1K	R0402	0402
R4	10K	R0402	0402
R5	300K	R0402	0402
R8	10	R0402	0402
R9	10K	PVZ2A	PVZ2A
R10	8K	R0402	0402
R11	1M	R0402	0402
R12	10	R0402	0402
R13	10K	R0402	0402
R15	10K	R0402	0402
R16	10K	R0402	0402
R17	10K	R0402	0402
R18	680	R0402	0402
R19	680	R0402	0402

Part	Value	Device	Package
R20	680	R0402	0402
R21	470	R0402	0402
R22	1.6K	R0402	0402
R23	10K	R0402	0402
R24	10K	PVZ2A	PVZ2A
SW1	B3U	B3U	B3U
SW2	B3U	B3U	B3U
SW3	EG1390	EG1390	EG1390A
U1	JN5139-Z01	JN5139-Z01	JN5139-Z01
U2	CP2102	CP2102	MLP28
U3	L6924D	L6924D	VFQFPN16
U4	OPA2336	OPA2336	MSOP8
U6	M25P128	M25P128	SO16
U7	M25P128	M25P128	SO16
X1	MINI-USB-BMOLEXNOPOST	MINI-USB-BMOLEXNOPOST	USB-MINIB-MOLEX-54819-0572

Pulse Oximeter Version 2

Table 9. Pulse oximeter version 2 parts list.

Quantity	P/N	Designator	Description
1	616-1029-1	U1	MODULE ZIGBEE JN5139
1	336-1160	U2	IC USB-TO-UART
1	OPA2336EACT	U4	IC OPAMP
1	WM17116CT	X1	CONN MINIUSB 5POS
1	EG4632CT	SW3	SWITCH SLIDE
4	PDB-C160SM	PD1, PD2, PD3, PD4	PHOTODIODE BLUE
3	475-2752-1	D2, D3, D4	LED GREEN
1	475-2709-1	D6	LED GREEN 0603
1	475-1195-6	D5	LED RED 0603
1	497-8278-1	U3	IC BATT CHARGER
2	SW1021CT	SW1, SW2	SWITCH TACT
1	SMT660/910	D1	EPITEC INC
CAP			
1	478-3272-1	C3	CAP 4.7UF 0805
5	445-1266-6	C1, C2, C9, C11, C12	CAP .10UF 0402
2	PCC2475CT	C7, C8	CAP 4.7UF 0402
4	587-1231-1	C4, C10, C15, C16	CAP 1.0UF 0402
1	399-1279-1	C5	CAP .01UF 0402
1	399-1031-1	C6	CAP 1000PF 0402
RES			
2	RR05P1.0KDCT	R1, R3	RES 1.0K
2	RR05P64.9KDCT	R2, R7	RES 64.9K
5	RR05P10.0KDCT	R4, R13, R15, R16, R17	RES 10.0K
2	RHM300KLCT	R5, R11	RES 300K
2	RR05P1.6KDCT	R6, R22	RES 1.6K
3	RR05P680DCT	R18, R19, R20	RES 680
1	RR05P470DCT	R21	RES 470
1	RR05P100KDCT	R12	RES 100K

Appendix D - JN5139 Module Pin Descriptions

Pin Configurations

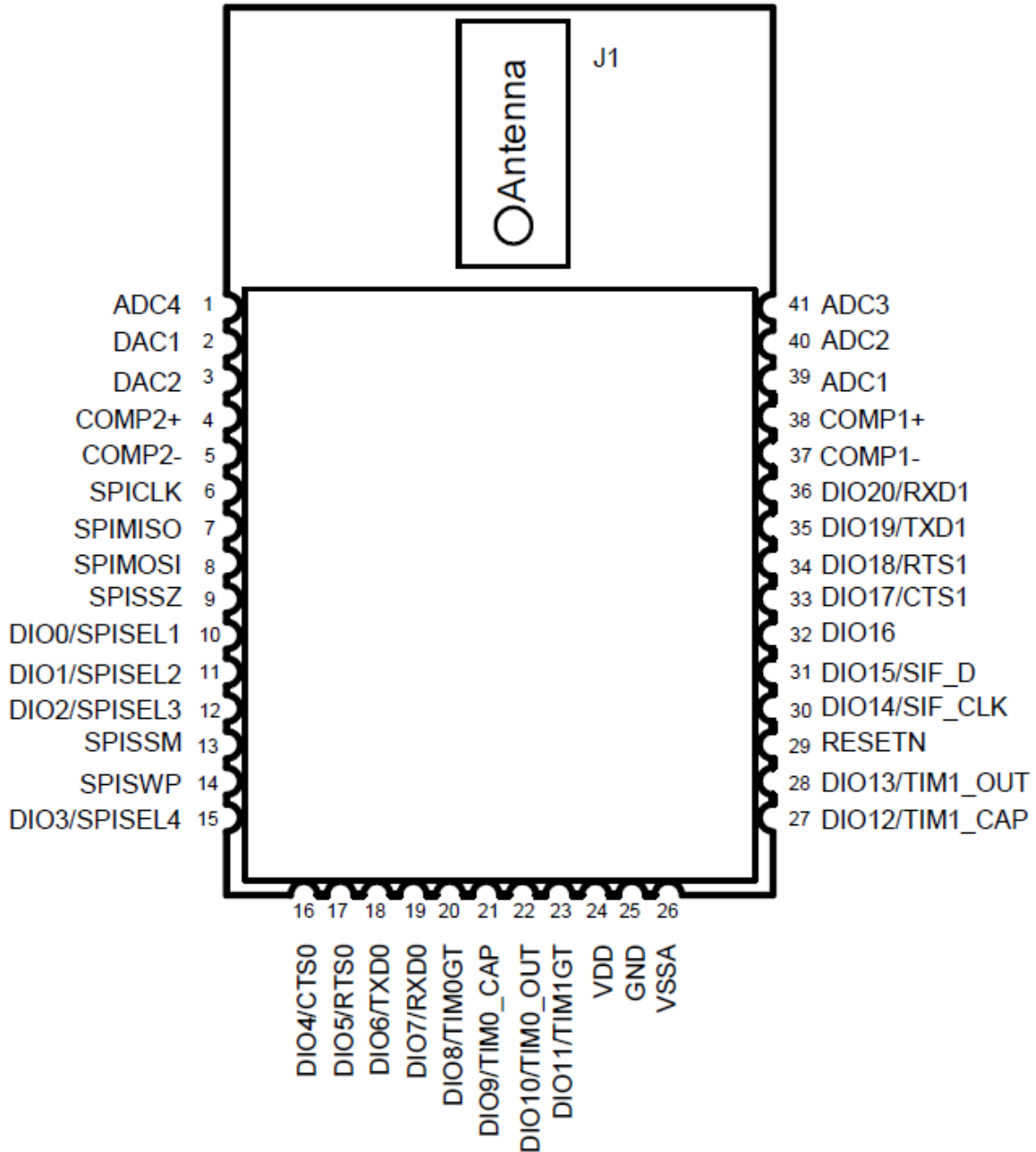


Figure 61. JN5139 module pin configurations (top view) [40].

Pin Assignments

Table 10. JN5139 module pin assignments (from [40]).

Pin	Signal	Function	Alternative Function
1	ADC4	Analogue to Digital input	
2	DAC1	Digital to Analogue output	
3	DAC2	Digital to Analogue output	
4	COMP2+	Comparator 2 inputs	
5	COMP2-		
6	SPICLK	SPI master clock out	
7	SPIMISO	SPI Master In/Slave Out	
8	SPIMOSI	SPI Master Out/Slave In	
9	SPISSZ	SPI select from module - SS0 (output)	
10	SPISEL1	SPI Slave Select1 (output)	General Purpose Digital I/O DIO0
11	SPISEL2	SPI Slave Select2 (output)	General Purpose Digital I/O DIO1
12	SPISEL3*	SPI Slave Select3 (output)	General Purpose Digital I/O DIO2 *
13	SPISSM	SPI select to FLASH (input)	
14	SPISWP	FLASH write protect (input)	
15	SPISEL4*	SPI Slave Select4 (output)	General Purpose Digital I/O DIO3*
16	CTS0	UART0 Clear To Send (input)	General Purpose Digital I/O DIO4
17	RTS0	UART0 Request To Send (output)	General Purpose Digital I/O DIO5
18	TXD0	UART0 Transmit Data (output)	General Purpose Digital I/O DIO6
19	RXD0	UART0 Receive Data (input)	General Purpose Digital I/O DIO7
20	TIM0GT	Timer0 clock/gate (input)	General Purpose Digital I/O DIO8
21	TIM0_CAP	Timer0 capture (input)	General Purpose Digital I/O DIO9
22	TIM0_OUT	Timer0 PWM (output)	General Purpose Digital I/O DIO10
23	TIM1GT	Timer1 clock/gate (input)	General Purpose Digital I/O DIO11
24	VDD	3V power	
25	GND	Digital ground	
26	VSSA	Analogue ground	
27	TIM1_CAP	Timer1 capture (input)	General Purpose Digital I/O DIO12
28	TIM1_OUT	Timer1 PWM (output)	General Purpose Digital I/O DIO13
29	RESETN	Active low reset	
30	SIF_CLK	Serial Interface clock / Intelligent peripheral clock	General Purpose Digital I/O DIO14

Pin	Signal	Function	Alternative Function
31	SIF_D	Serial Interface data / Intelligent peripheral data	General Purpose Digital I/O DIO15
32	DIO 16	Intelligent peripheral device select	General Purpose Digital I/O
33	CTS1	UART1 Clear To Send (input)	General Purpose Digital I/O DIO17
34	RTS1	UART1 Request To Send (output)	General Purpose Digital I/O DIO18
35	TXD1	UART1 Transmit Data (output)	General Purpose Digital I/O DIO19
36	RXD1	UART1 Receive Data (input)	General Purpose Digital I/O DIO20
37	COMP1-	Comparator 1 inputs	
38	COMP1+		
39	ADC1	Analogue to Digital input	
40	ADC2	Analogue to Digital input	
41	ADC3	Analogue to Digital input	